ILIADIS

Proton Resonance Spectroscopy in ^{36}Ar

William K. Brooks, Jr.

Triangle Universities Nuclear Laboratory
Department of Physics
Duke University

1988

PROTON RESONANCE SPECTROSCOPY IN ^{36}Ar

by

William K. Brooks, Jr.

Department of Physics
Duke University

Date: September 1, 1988

Approved:

Edward G Bilpuch
E. G. Bilpuch, Supervisor

Lawrence Weller

Richard L. Walter

Henry R. Weller

Frank DeLucia

Dissertation submitted in partial fulfillment of
the requirements for the degree of Doctor
of Philosophy in the Department of
Physics in the Graduate School
of Duke University

1988

ABSTRACT

(Physics-Nuclear)

PROTON RESONANCE SPECTROSCOPY IN ^{36}Ar

by

William K. Brooks, Jr.

Department of Physics
Duke University

Date: September 1, 1988

Approved:

Edward G. Bilpuch
E. G. Bilpuch, Supervisor

Laurence Weiss
Richard L. Walter
Norris R. Wallace
Frank DeTurci

An abstract of a dissertation submitted in partial fulfillment of the requirements for the degree of Doctor of Philosophy in the Department of Physics in the Graduate School of Duke University

1988

ABSTRACT

Excitation functions for proton elastic scattering and for proton-induced reactions on ^{35}Cl were measured with the KN Van de Graaff accelerator and associated high resolution system at TUNL. Differential cross sections for $^{35}Cl(p,p_0)$, (p,p_1), (p,p_2), (p,α_0), and (p,α_1) were measured in the range E_p = 0.6 to 4.0 MeV. The data were measured at five angles with an overall resolution of about 350 eV.

The measured excitation functions were analyzed with a multi-level, multi-channel R-matrix formalism. Resonance parameters were extracted for approximately 200 levels. The resonance parameters include resonance energy, total angular momentum, parity, partial elastic and reaction widths, channel spin or orbital angular momentum mixing ratios, and for some resonances the relative signs of width amplitudes. A number of resonances have strong level-level interference effects.

Comparison of these data with the Porter-Thomas distribution resulted in good agreement for almost all channels which had a statistically significant number of resonances. These comparisons indicated that nearly all the proton and alpha strength in ^{36}Ar for this energy range was observed in the present study. The s-wave proton strength function ratio for s = 1 and s = 2 resonances was consistent with previous measurements for 4N nuclei. This ratio can be used to set limits on the effective spin-spin interaction between projectile and target.

The present data are compared with the reduced width sum rule for proton and alpha decay. Large alpha strength was observed for the 1^-, 2^+, and 3^- states. The total alpha strength for the 2^+ and the 3^- states is on the order of the "single particle" estimate. Large proton strength was observed in the p-wave channels .

ACKNOWLEDGEMENTS

I would like to thank Dr. E. G. Bilpuch for his unfailing support and encouragement in every phase of this research project. I would like to thank Dr. G. E. Mitchell for his help in preparing this dissertation and for his suggestions and oversight during the course of this experiment.

The extensive instruction and help given me by C. R. Westerfeldt throughout this project and others is very deeply appreciated.

I would like to thank Dr. J. R. Vanhoy, Dr. B. J. Warthen, Dr. J. F. Shriner, Dr. D. Fang, Dr. P. Ramakrisnan and J. S. Bull for a number of enlightening discussions during the course of the data acquisition and analysis, and for their assistance in taking data. Thanks go to J. Bull for help in making several of the diagrams, and especially to B. Smith for all his input for the statistical analysis presented here. Thanks also to B. Smith, L. James, K. Keeter, and C. Fowler for their help in taking this data. I would especially like to thank S. Frankle for her help and also C. Frankle, S. Wilburn, and C. Coburn for their assistance in preparing this manuscript, and to D. Albright for her help in its completion.

Thanks go to S. E. Edwards and P. Mulkey for their help in maintaining the electronics used in this experiment, to R. Rummel and P. Carter for their help in maintaining the accelerator systems, and to A. Lovette for his provision of machine shop support. I would also like to thank M. Bailey for preparing several of the figures for this dissertation.

I would like to thank my parents for their support and guidance throughout my life.

This work was supported in part by the Department of Energy.

TABLE OF CONTENTS

ABSTRACT iii
ACKNOWLEDGEMENTS iv
LIST OF FIGURES vii
LIST OF TABLES x
I. INTRODUCTION 2
A. General Background 2
B. Previous Results for Proton-Induced Reactions on ^{35}Cl 5
II R-MATRIX FORMALISM 8
A. Introduction 8
B. Channel Wave Functions 10
C. Solutions for the External Region 11
D. Solutions for the Internal Region 11
E. Connection Between Internal and External Region 14
F. Scattering Amplitudes and Cross Sections 16
G. Single-level Formulas 17
III. EXPERIMENTAL EQUIPMENT AND PROCEDURES 20
A. Laboratory Equipment 20
1. Accelerator and Ion Source 20
2. High Resolution System 23
3. Scattering Chamber and Collimators 23
4. Targets 26
B. Signal Processing and Data Flow 27
1. Digitization of Charged Particle Signals 27
2. Sorting and Storage of Spectra 30
C. Data Acquisition Procedures and Automation 31
1. Determining and Incrementing Energy 31
2. Automating Data Acquisition 32
D. Obtaining Cross Sections from Spectra 32
1. Description of XSYS 32
2. Procedure for Generating Yield Curves 33

IV. ANALYSIS OF RESONANCE DATA 37
A. Description of MULTI6 37
B. Fitting Procedures 38
1. Basic Fitting Approach 38
2. Multilevel Interference 60
V. DATA, FIT, AND RESONANCE PARAMETERS 80
A. Data and Fit 80
B. Resonance Parameters 101
VI. ANALYSIS AND RESULTS 121
A. Statistical Tests 121
B. Resonance Strengths 133
1. Proton Strength 166
2. Alpha Strength 166
C. Sum Rules 171
D. Astrophysical Reaction Rates 171
E. Special States 185
1. Isobaric Analog States 185
2. T = 2 State 188
F. Strength Functions 188
VII. SUMMARY 190
APPENDIX 192
BIBLIOGRAPHY 213
BIOGRAPHY 216

LIST OF FIGURES

1.1	Level Diagram of ^{36}Ar	4
3.1	Schematic Diagram of the High Resolution Laboratory	22
3.2	Schematic Diagram of the Charged Particle Scattering Chamber	25
3.3	Block Diagram of the Data Acquisition Electronics	29
3.4	Charged Particle Spectrum	35
4.1	Coulomb Penetrabilities for the $^{35}Cl(p,p_0)$ Reaction	41
4.2	Variation in Resonance Shape as a Function of Angle and ℓ Value	47
4.3	Variation in s-wave Resonance Shape with J value	49
4.4	Variation in p-wave Resonance Shape with J value	51
4.5	Variation in d-wave Resonance Shape with J value	53
4.6	Variation in f-wave Resonance Shape with J value	55
4.7	Variation in 1^-, p-wave Resonance Shape with Channel Spin Mixing	57
4.8	Variation in 2^+, d-wave Resonance Shape with Channel Spin Mixing	59
4.9	Variation in 2^+, (s = 2) Resonance Shape with Orbital Angular Momentum Mixing	62
4.10	Variation in 2^-, (s = 2) Resonance Shape with Orbital Angular Momentum Mixing	64
4.11	Two Level Interference for Levels with the Same J^π and $\Gamma_1 >> \Gamma_2$ at $\theta = 165^\circ$	67
4.12	Two Level Interference for Levels with the Same J^π and $\Gamma_1 >> \Gamma_2$ at $\theta = 90^\circ$	69
4.13	Two Level Interference for Levels with Different J^π and $\Gamma_1 >> \Gamma_2$ at $\theta = 165^\circ$	71
4.14	Two Level Interference for Levels with Different J^π and $\Gamma_1 >> \Gamma_2$ at $\theta = 90^\circ$	73
4.15	Two Level Interference Effects on the (p,α_0) Reaction Cross Sections with One Alpha Partial Width Included	76
4.16	Two Level Interference Effects on the (p,α_0) Reaction Cross Sections with Two Alpha Partial Widths Included	78

5.1 Elastic and (p,α_0) Data and Fit for θ = 165°, E_p = 1.2 to 2.2 MeV 82

5.2 Elastic and (p,α_0) Data and Fit for θ = 165°, E_p = 2.2 to 3.2 MeV 84

5.3 Elastic Scattering Data and Fit for Five Angles, E_p = 2.4 to 2.6 MeV 86

5.4 Elastic Scattering for θ = 165° and (p,α_0) Data and Fit at Five Angles, E_p = 1.2 to 2.2 MeV 88

5.5 Elastic and (p,α_0) Data and Fit for θ = 165°, E_p = 1.2 to 1.6 MeV 90

5.6 Elastic and (p,α_0) Data and Fit for θ = 165°, E_p = 1.6 to 2.0 MeV 92

5.7 Elastic and (p,α_0) Data and Fit for θ = 165°, E_p = 2.0 to 2.4 MeV 94

5.8 Elastic and (p,α_0) Data and Fit for θ = 165°, E_p = 2.4 to 2.8 MeV 96

5.9 Elastic and (p,α_0) Data and Fit for θ = 165°, E_p = 2.8 to 3.2 MeV 98

5.10 Elastic and (p,α_0) Data Only, for θ = 165°, E_p = 3.2 to 4.0 MeV 100

6.1 Porter-Thomas Distribution for 1^- p-wave Protons with s = 1 124

6.2 Porter-Thomas Distribution for 1^- f-wave Protons with s = 2 126

6.3 Porter-Thomas Distribution for 1^- p-wave Protons with s = 2 128

6.4 Porter-Thomas Distribution for 2^- p-wave Protons with s = 2 130

6.5 Porter-Thomas Distribution for 3^- p-wave Protons with s = 2 132

6.6 Porter-Thomas Distribution for 2^+ Alphas 135

6.7 Porter-Thomas Distribution for 1^- Alphas 137

6.8 Proton Reduced Widths for 0^- Resonances in ^{36}Ar 139

6.9 Proton Reduced Widths for 0^+ Resonances in ^{36}Ar 141

6.10 Proton Reduced Widths for 1^- p-wave Resonances in ^{36}Ar 143

6.11 Proton Reduced Widths for 1^- f-wave Resonances in ^{36}Ar 145
6.12 Proton Reduced Widths for 1^+ s-wave Resonances in ^{36}Ar 147
6.13 Proton Reduced Widths for 1^+ d-wave Resonances in ^{36}Ar 149
6.14 Proton Reduced Widths for 2^- p-wave Resonances in ^{36}Ar 151
6.15 Proton Reduced Widths for 2^- f-wave Resonances in ^{36}Ar 153
6.16 Proton Reduced Widths for 2^+ s-wave Resonances in ^{36}Ar 155
6.17 Proton Reduced Widths for 2^+ d-wave Resonances in ^{36}Ar 157
6.18 Proton Reduced Widths for 3^- p-wave Resonances in ^{36}Ar 159
6.19 Proton Reduced Widths for 3^- f-wave Resonances in ^{36}Ar 161
6.20 Proton Reduced Widths for 3^+ d-wave Resonances in ^{36}Ar 163
6.21 Proton Reduced Widths for 4^+ d-wave Resonances in ^{36}Ar 165
6.22 Alpha Reduced Widths for 0^+ Resonances in ^{36}Ar 168
6.23 Alpha Reduced Widths for 1^- Resonances in ^{36}Ar 170
6.24 Alpha Reduced Widths for 2^+ Resonances in ^{36}Ar 173
6.25 Alpha Reduced Widths for 3^- Resonances in ^{36}Ar 175
6.26 Total $^{35}Cl(p,\alpha)^{32}S$ Cross Section..... 182
6.27 Effective Energies for Nuclear Astrophysical Reactions..... 184
6.28 $\langle\sigma v\rangle$ Versus Temperature..... 187
A.1 Apparatus for Heating Backings 206
A.2 Time Yield for Decaying and Stable Targets..... 210

LIST OF TABLES

4.1 Allowed Channels for Elastic Scattering.....42
4.2 Allowed Channels for the $^{35}Cl(p,p_1)$ Reaction.....43
4.3 Allowed Channels for the $^{35}Cl(p,p_2)$ Reaction.....44
5.1 Resonance Parameters for $^{35}Cl(p,x)$ in the Range E_p = 1.0 to 3.18 MeV.....103
5.2 Resonance Parameter Assignments for $^{35}Cl(p,x)$ in the Range E_p = 3.18 to 4.0 MeV.....113
6.1 Proton Strength in ^{36}Ar.....176
6.2 Alpha Strength in ^{36}Ar.....177

PROTON RESONANCE SPECTROSCOPY IN ^{36}AR

CHAPTER I

INTRODUCTION

A. General Background

Resonance processes in nuclear physics were first observed in 1935 with the measurements of Moon and Tillman (1936), Amaldi and Fermi (1935), and Szilard (1935). They found that low energy neutron capture depended strongly upon the specific nucleus and on the velocity of the neutrons. These observations led Bohr (1936) to postulate the formation of a compound nucleus. The key idea of this model is that the incident particle's energy is rapidly shared among the nucleons. This implies that its decay is a statistical process and will occur with a lifetime up to 10^6 times longer than the previously assumed reaction times of 10^{-21} seconds. Several compound nucleus formalisms (using somewhat different approaches) were developed during the following decade (Kapur and Peierls 1938; Wigner 1946a; Wigner 1946b, Wigner and Eisenbud 1947).

Although resonances in nuclear cross sections have been observed since the early part of this century, the accelerators used in producing particle beams often had relatively poor energy regulation; therefore differential cross sections were measured with correspondingly poor energy resolution. The early theoretical formalisms for multiple channel and level resonance reactions were general, but the complexity of the calculations prohibited analysis of complicated cross section data. It was only in the 1960's that the calculations became feasible. By this time accelerator energy resolutions had also improved significantly. At Duke University an energy corrective feedback system which achieved experimental energy resolution of a hundredth of a percent or less was developed. The initial studies employed gas targets. A long series of nuclei were then investigated with thin solid targets. Recently a series of experiments has been initiated to study the systematic properties of proton resonance reactions on odd mass nuclei in the nuclear "s - d" shell.

Figure 1.1 Level diagram of ^{36}Ar. Excitation functions are shown on an expanded scale for the $^{35}Cl(p,p_0)^{35}Cl$ and the $^{35}Cl(p,\alpha_0)^{32}S$ reactions measured in this experiment.

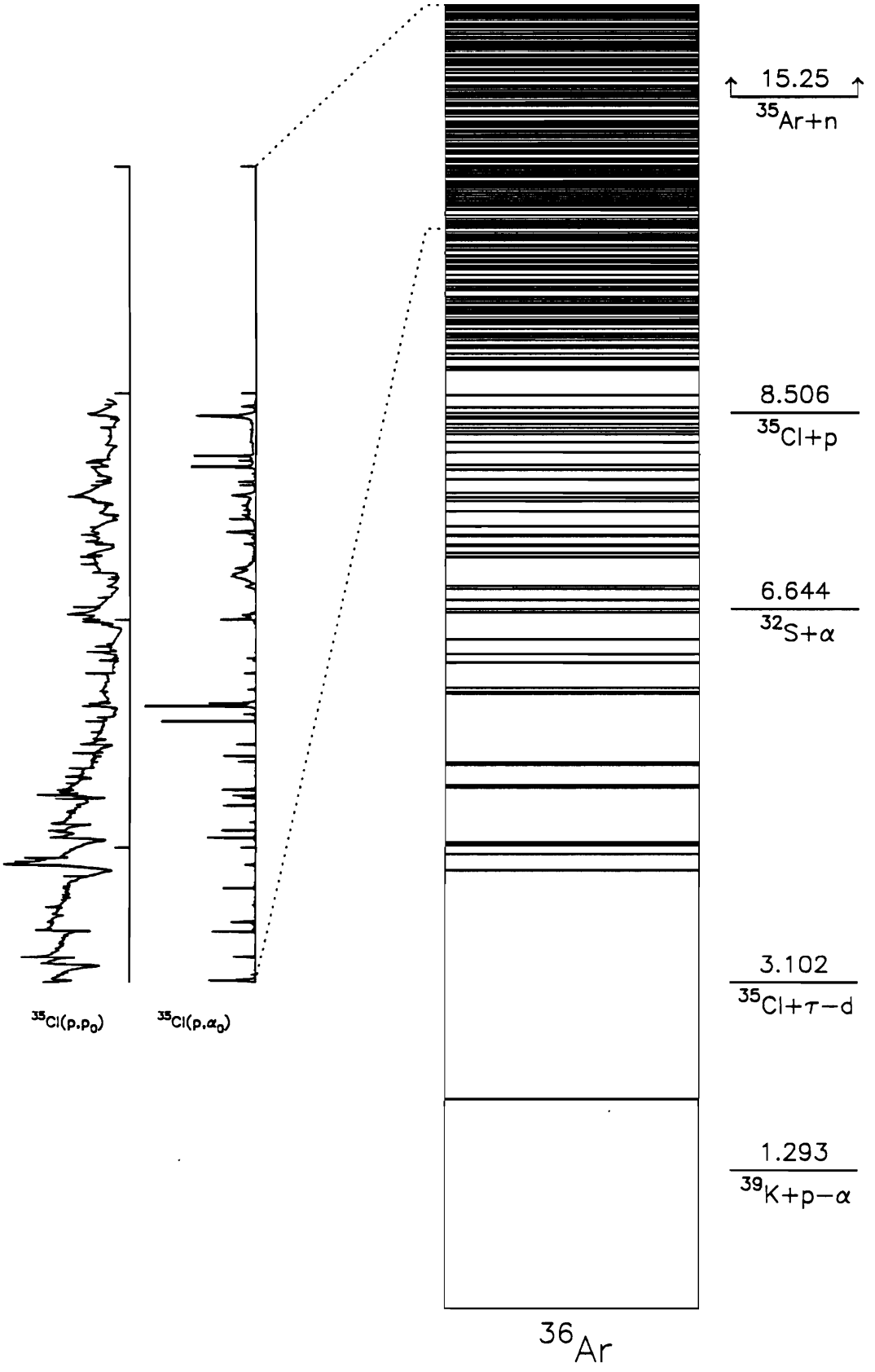
15.25
35Ar+n
8.506
35Cl+p
6.644
32S+α
3.102
35Cl+τ−d
1.293
39K+p−α
35Cl(p,p0)
35Cl(p,α0)
36Ar

The TUNL High Resolution Laboratory is now beginning a third decade of measurements using a high resolution proton beam to initiate nuclear reactions. In the middle sixties and early seventies the emphasis was on detailed measurements on even-even target nuclei in the mass range $40 \leq A \leq 64$. These studies were directed primarily toward understanding the fine structure of analog states, reviewed in Bilpuch (1976). After these studies came a series of experiments extending from the middle seventies to the early 1980's which systematically examined correlations between exit channel widths and amplitudes by measurements of inelastic scattering. In these experiments one studies the differential cross section for all open channels, and follows with measurements of detailed angular distributions of the reaction products. In recent years a new experimental focus has been on the analysis of resonance data from non-zero spin targets. The present study is one of these measurements. It is anticipated that future detailed measurements using the (p,α_0) channel angular distributions will yield more information on width and amplitude correlations, similar to that obtained in the previous inelastic scattering studies. Here we focus on the results which are obtained from the initial (survey) experiment.

B. Previous Results for Proton-Induced Reactions on ^{35}Cl

There have been a number of experiments on proton-induced resonance reactions on ^{35}Cl, but no studies of the elastic scattering reaction. Erne and Endt (1965) measured $\sigma(E_p;E_\gamma)$ for the $^{35}Cl(p,\gamma)$ channel from E_p = 0.4 to 3.1 MeV and found 65 resonances. (All energies quoted in this section will be proton laboratory energies.) They obtained resonance strengths for each resonance, total widths and inelastic decay widths for a few levels, and branching ratios for a number of the lower energy resonances More recently Johnson, Meyer, and Reitmann (1974) also measured $\sigma(E_p;E_\gamma)$, obtaining energies and strengths for the (p,γ) and (p,p_2) channels in the range 0.4 to 3.0 MeV, and energies and strengths of the (p,p_1) resonances in the range 1.5 to 3.0 MeV. They deduced γ-branching ratios, mean lifetimes, spins, and parities. Isospin values were assigned for a number of levels. The proton energy resolution was about one keV in the experiment by Johnson, and two

to six keV in the earlier study by Erne.

The (p,γ) reaction was studied at higher proton energies by Kernbach (1970), who measured the ^{35}Cl(p,γ_0) and (p,γ_1) yields from 6.0 to 12.2 MeV to study gross structure in the GDR region.

The ^{35}Cl(p,α_0)^{32}S reaction has been carefully studied with moderate energy resolution. Clarke, Almqvist, and Paul (1960) investigated the (p,α_0) reaction for a variety of target nuclei including ^{35}Cl in the region 1 to 3 MeV. They measured the differential cross section at 90°, and obtained reduced widths and strength functions for protons and alpha particles; Q values for the reaction were also measured.

Karadzhev, Man'ko, and Chukreev (1966) performed a measurement of the ^{35}Cl(p,α_0)^{32}S reaction from 1.3 to 3.0 MeV on ^{35}Cl and ^{37}Cl, using the ^{natural}Cl(p,p_0) cross section to eliminate ambiguities in the spin assignments. The spins were assigned by a detailed analysis of the angular distribution of the alpha particles. They determined the spins, parities, and reduced widths of 25 levels in ^{36}Ar, and discussed possible deviations from the Porter-Thomas distribution.

Bosnjakovic, Bouwmeester, Van Best and Pruys (1968) also have performed detailed studies on the ^{35}Cl(p,α_0) reaction in the range 0.83 to 2.93 MeV. They observed 76 resonances, and reported resonance energies, strengths, and widths. Angular distributions were measured at 58 resonances and definite spin and parity assignments were made for 24 resonances. Possible isobaric analog states were identified.

There are large gaps in several of these proton-induced reactions on ^{35}Cl: the ^{35}Cl(p,γ) cross section from 3.1 MeV to 6 MeV; (p,p_1) resonance strengths above 3.0 MeV; (p,p_2) resonance strengths above 3.0 MeV; ^{35}Cl(p,α_0) resonance parameters below 0.83 MeV and above 3.0 MeV. Good resolution proton elastic scattering data is not available for ^{35}Cl. A detailed study of the elastic scattering would be most useful to obtain detailed information on the resonance parameters.

The measurements performed in this experiment were of the differential cross section at five scattering angles for the following channels:

1) Elastic scattering from E_p = 0.60 to 4.01 MeV
2) (p,p_1) from the threshold value of 1.22 MeV to 4.01 MeV
3) (p,p_2) from the threshold at 1.76 MeV to 4.01 MeV
4) (p,α_0) from 0.60 to 4.01 MeV
5) (p,α_1) from 0.60 to 4.01 MeV

While the (p,α_2) channel and several other inelastic channels are open, they are kinematically suppressed and in practice were not observed.

The analysis of these data provided much new spectroscopic information for this nucleus. Resonance energy, partial widths, total angular momentum, parity and orbital angular momenta were obtained for about two hundred resonances; of these about 140 are considered to have reliable assignments while about 60 are somewhat tentative. It was often possible to clearly determine the channel spin mixing for resonances and to measure the relative signs between partial widths.

In the next chapter the R-matrix theory is outlined. Chapter III contains a description of the experimental apparatus and the techniques used to obtain the data. The following chapter describes the data fitting methods and strategies. Chapter V is a presentation of the data and the fit; the resonance parameters are also listed. The next chapter treats analysis and interpretation of the resonance parameters. Chapter VII provides a summary. Detailed procedures and information about nuclear target preparation are given in the appendix.

CHAPTER II

R-MATRIX FORMALISM

In order to obtain meaningful information from complicated resonance scattering data it is necessary to adopt some appropriate quantum mechanical formalism. Over time nuclear reaction theories have proliferated; while the basic ideas are the same, one formalism may be much more appropriate for a given application. Matrix formalisms are the most general and elegant presentation of reaction theory. Examples of these (see Marmier and Sheldon 1969) are the M-matrix polarization theory (Wolfenstein 1952), R-matrix ("reaction matrix") (Wigner and Eisenbud 1947), S-matrix ("scattering matrix") (Heisenberg 1943), T-matrix ("transition matrix"), and U-matrix ("collision matrix"). Common elements of these include consideration of asymptotic wave functions for the system of interest and emphasis on matrix elements as fundamental quantities in expressing interaction probabilities.

A. Introduction

The theoretical framework used to obtain the resonance parameters in this work is the R-matrix theory of Wigner and Eisenbud (1947). This is a non-relativistic quantum mechanical formulation of the reaction-scattering problem. The definitive review article is the Lane and Thomas paper of 1958, although scores of accounts of this and similar other reaction theories have been given, both earlier and more recently (see McCarthy 1968). The summary given here will strongly reflect the influence of that paper; for the historical evolution of the theory see Lane and Thomas (1958) or Vogt (1952).

The essence of the R-matrix theory is as follows. The scattering problem is posed in a 6A dimensional space (3 configuration space dimensions and 2 spin dimensions for each nucleon). A surface is postulated in this space such that the strong interaction does not occur

outside of the volume enclosed. There are a number of distinct regions outside the surface which correspond to two separated particles α_1 and α_2; these are the reaction "channel" subspaces. In the exterior region the potential and the wave function in any given channel are known; the asymptotic wave functions may be used to generate an expression for the cross section. Quantities similar to logarithmic derivatives of the interior and exterior wave functions are matched at the interaction radius; the interior functions have in turn been specified by an eigenfunction expansion of basis vectors. These vectors are eigenfunctions of the real nuclear Hamiltonian and each is associated with a particular set of quantum numbers. Thus the cross section may be expressed in terms of quantum numbers and partial widths (matrix elements) characterizing the internal nuclear wave function. The formalism is made complicated only by the number of reaction channels and number of levels involved in the problem.

If the energy eigenfunction representation is chosen the wave function for the total system is defined in all of space by

$$\mathbf{H}\,\Psi = E\,\Psi \tag{2.1}$$

where E is the total energy and

$$\mathbf{H} = \sum_{i=1}^{A} \frac{-\hbar^2}{2m_i}\nabla_i^2 + \mathbf{V}. \tag{2.2}$$

In a particular channel this Hamiltonian may be rearranged into a sum of four parts corresponding to

(1) energy of the center of mass
(2) energy of the separated pair in the center-of-mass frame, ε
(3),(4) internal energies of each particle of the separated pair α_1 and α_2, $E_{\alpha 1}$, $E_{\alpha 2}$.

Thus a product wave function will satisfy the differential equation:

$$\psi = \Phi^{(1)}\,\chi^{(2)}\,\psi_{\alpha 1}^{(3)}\,\psi_{\alpha 2}^{(4)} \tag{2.3}$$

Since the center of mass motion is irrelevant, Φ will not be further considered and the kinetic energy associated with Φ will be taken as being

equal to zero. Thus the scattering is being viewed in the center-of-mass frame and the total energy (non-relativistic) in a given channel is then

$$E^{total} = \varepsilon + E_{\alpha 1} + E_{\alpha 2} \ . \tag{2.4}$$

B. Channel Wave Functions

The intrinsic wave functions $\psi_{\alpha 1}$ and $\psi_{\alpha 2}$ may be coupled together into what will be termed the "channel spin wave functions" $\psi_{\alpha sv}$:

$$\psi_{\alpha sv} = \sum_{i_1+i_2=v} (l_1 l_2 i_1 i_2 | sv)\, \psi_{\alpha_1 l_1 i_1}\, \psi_{\alpha_2 l_2 i_2} \tag{2.5}$$

The channel spin wave functions are orthonormal in the following sense:

$$\int_s \psi^*_{\alpha sv}\, \psi_{\alpha' s' v'}\, ds = 4\pi\, a_\alpha^2\, \delta_{\alpha sv, \alpha' s' v'} \ . \tag{2.6}$$

where $ds = \sum_c ds_c = \sum_c a_\alpha^2\, d\Omega_\alpha dq_\alpha$, q_α representing internal variables.

For a spherically symmetric potential the wave functions of relative motion are

$$\chi_c \sim r^{-1} u_{\alpha s \ell}(r) i^\ell Y_m^\ell (\Omega_\alpha) \tag{2.7}$$

where the $Y_m^{(\ell)}$ are the spherical harmonics and the $u_{\alpha s \ell}(r_\alpha)$ satisfy the radial equation

$$\left[\frac{d^2}{dr_\alpha^2} - \frac{\ell(\ell+1)}{r_\alpha^2} - \frac{2M_\alpha}{h^2}(V_{\alpha s \ell} - E_\alpha)\right] u_{\alpha s \ell}(r_\alpha) = 0 \ . \tag{2.8}$$

For clarity later the "channel functions" are defined as

$$\varphi_{\alpha s \ell v m} = \frac{1}{r_\alpha} \psi_{\alpha sv}\, i^\ell\, Y_m^{(\ell)} \ . \tag{2.9}$$

These represent the non-radial part of the wave function; they may be regarded as unit vectors identifying each channel in the channel space. They are orthonormal on the sum of the channel surfaces **s**:

$$\int \varphi^*_{\alpha s \ell v m} \varphi_{\alpha' s' \ell' v' m'} ds = \delta_{\alpha s \ell v m, \alpha' s' \ell' v' m'} \quad . \tag{2.10}$$

C. Solutions for the External Region

In the external region the potential is due only to the Coulomb force, and the above equation (2.8) may be solved exactly. Reducing the equation to dimensionless form with the substitutions $k_\alpha r_\alpha = \rho_\alpha$ and $\eta_\alpha = Z_{\alpha 1} Z_{\alpha 2} e^2 / h v_\alpha$, two linearly independent solutions may be found and characterized as "incoming" and "outgoing" waves (based on the sign of the overall phase) having the asymptotic forms

$$I_c \sim \exp\left[-i \left(\rho_\alpha - \eta_\alpha \ln 2\rho_\alpha - \frac{\ell\pi}{2} + \sigma_{\alpha 0}\right)\right], \quad O_c = I_c^* \ . \tag{2.11}$$

Thus in the external region the complete incoming and outgoing wave functions in a given channel are

$$\mathcal{I}_{\alpha s \ell v m} = \frac{1}{\sqrt{v_\alpha}} I_{\alpha \ell} \varphi_{\alpha s \ell v m}$$

$$\mathcal{O}_{\alpha s \ell v m} = \frac{1}{\sqrt{v_\alpha}} O_{\alpha \ell} \varphi_{\alpha s \ell v m} \tag{2.12}$$

where the normalization is to unit incident flux.

D. Solutions for the Internal Region

Since a detailed potential for the many-body nuclear problem is not known, an approach which leaves out explicit reference to the potential is desirable; the problem is parameterized in terms of physically meaningful resonance parameters such as quantum numbers or partial widths. In matching the logarithmic derivative quantities at the reaction surface it is necessary to have an expression for the wave function and its derivative; an approach which both bypasses specification of the interior potential and

which relates the wave functions to derivatives is as follows.

In the interior region the real nuclear wave function Ψ satisfies the Schrödinger equation:

$$\mathbf{H}\,\Psi = E\,\Psi \tag{2.13}$$

Another set of orthonormal eigenfunctions of **H** also may be generated which satisfy special conditions:

$$\begin{aligned} &\mathbf{H}\,X_\lambda = E_\lambda\,X_\lambda \\ &r_c\frac{dX_\lambda}{dr_c} = b_c\,X_\lambda \end{aligned} \tag{2.14}$$

Here r_c is the channel radius and b_c is a constant. The real nuclear wave function may be expressed as an expansion in the X_λ:

$$\Psi = \sum_\lambda A_\lambda X_\lambda\ , \qquad A_\lambda = \int_\tau \Psi X_\lambda^*\,d\tau\ . \tag{2.15}$$

The functions X_λ are here taken to be states of definite J and M.

The derivative of the wave function may be related to the A_λ through the two Schrödinger equations above using Green's first identity in 3A dimensions. Multiplying the first by X_λ^* and the complex conjugate of the second by Ψ, taking the difference of the two resulting equations (which removes V explicitly) and integrating over the nuclear volume τ gives

$$(E - E_\lambda)\int_\tau \Psi^* X_\lambda\,d\tau = \int_S \frac{\hbar^2}{2M_c}\left(\Psi^*\frac{d}{dr_c} - X_c\frac{d}{dr_c}\Psi^*\right)ds \tag{2.16}$$

where Green's identity has been used to reduce the volume integral on the RHS; the derivative normal to S is just $\Sigma_c d/dr_c$. Using the boundary condition on X_λ given before and identifying the integral on the LHS gives

$$A_\lambda = \frac{1}{E - E_\lambda}\int_S \frac{\hbar^2}{2m_c r_c}\left(\Psi X_\lambda^* b_c - X_\lambda^* r_c\frac{d}{dr_c}\Psi\right)ds \tag{2.17}$$

This expression can be reduced by making eigenfunction expressions for Ψ and $r\Psi$ in the channel functions φ_c on the channel surfaces (where the φ_c form a complete set) in the following way.

The "value" and "derivative" quantities

$$V_c = \sqrt{\frac{\hbar^2}{2M_c a_c}} \int_s \varphi_c^* \Psi \; ds$$
$$D_c = \sqrt{\frac{\hbar^2}{2M_c a_c}} \int_s \varphi_c^* \frac{d}{dr_c}(r_c \Psi) \; ds \qquad (2.18)$$

are numbers proportional to the radial part of the actual wave function and its derivative evaluated on the channel surface. They are essentially the coefficients in the channel function expansions

$$\Psi = \sum_c \sqrt{\frac{2M_c a_c}{\hbar^2}} V_c \varphi_c,$$
$$\frac{d}{dr_c}(r_{c'} \Psi) = \sum_c \sqrt{\frac{2M_c a_c}{\hbar^2}} D_c \varphi_{c'} \qquad (2.19)$$

Inserting these into the expression for A_λ and simplifying gives

$$A_\lambda = \frac{1}{E - E_\lambda} \sum_c (V_c b_c - D_c) \gamma_{\lambda c} \; , \qquad (2.20)$$

where $\gamma_{\lambda c} = \sqrt{\frac{\hbar^2}{2M_c a_c}} \int_s \varphi_c^* X_\lambda \; ds$ are the reduced width amplitudes.

Then the total interior wave function is

$$\Psi = \sum_c \left[\sum_\lambda \frac{X_\lambda \gamma_{\lambda c}}{E_\lambda - E} \right] (D_c - V_c b_c) \; . \qquad (2.21)$$

The quantity in the square bracket is the Green's function relating the value of Ψ to its derivatives on the channel surfaces. By multiplying the above equation by $\varphi_{c'}^*$ and integrating over **s**, the fundamental R-matrix relation is derived:

$$V_{c'} = \sum_c R_{c'c} (D_c - V_c b_c) \; , \qquad (2.22)$$

$$\text{where} \quad R_{c'c} = \sum_{\lambda} \frac{\gamma_{\lambda c'} \gamma_{\lambda c}}{E_\lambda - E} \quad . \tag{2.23}$$

Thus the essential function of the R-matrix is to relate the value of the interior radial wave function on a given channel surface to the value of the derivatives of the radial wave functions on all the channel surfaces. In the simplest case of one channel R is proportional to the ratio of the radial wave function to its derivative. The R-matrix itself is specified by quantities related directly to the nuclear Hamiltonian: the quantum numbers associated with the basis states, and the partial width amplitudes, which are proportional to the projection of the basis functions X_λ onto the channel functions φ_c, averaged over the channel surfaces.

Equation (2.21) may be rewritten

$$\Psi = \sum_c \sum_\lambda \left[\frac{\gamma_{\lambda c} (D_c - V_c b_c)}{E_\lambda - E} \right] X_\lambda \tag{2.24}$$

which displays more explicitly the energy-resonant relationship between the basis vectors and the actual nuclear wave function.

E. Connection Between Internal and External Regions

The elements of the R-matrix may be related to the measurable cross section using the collision matrix U. This matrix is defined using the asymptotic scattering wave functions. In the general case the total wave function is given by incoming and outgoing waves in many channels with various amplitudes:

$$\Psi = \sum_c (x_c O_c + y_c I_c) \quad . \tag{2.25}$$

In practice y_c is known, since the incident wave is prepared in the laboratory, while the x_c characterize the system under study. The transformation from the y_c to the x_c is given by the collision matrix:

$$x_{c'} = - \sum_{c} U_{c'c}\, y_c \,. \qquad (2.26)$$

The collision matrix has the properties of unitarity and symmetry corresponding to the conservation of probability and to invariance of the system under time reversal.

Using the expression (2.25) for the total *external* wave function the value and derivative quantities are (by direct computation)

$$\begin{aligned} V_c &= \sqrt{\frac{\hbar}{2}}\left(\rho_c^{-\frac{1}{2}} O_c x_c + \rho_c^{-\frac{1}{2}} I_c y_c\right) \\ D_c &= \sqrt{\frac{\hbar}{2}}\left(\rho_c^{\frac{1}{2}} O'_c x_c + \rho_c^{\frac{1}{2}} I'_c y_c\right) \end{aligned} \qquad (2.27)$$

At this point matrix notation will be adopted, where channel quantities with a single subscript are taken as a diagonal matrix with the subscripted quantities on the diagonal. Then

$$\begin{aligned} \mathbf{V} &= \sqrt{\frac{\hbar}{2}}\left(\rho^{-\frac{1}{2}} \mathbf{O}\mathbf{x} + \rho^{-\frac{1}{2}} \mathbf{I}\mathbf{y}\right) \\ \mathbf{D} &= \sqrt{\frac{\hbar}{2}}\left(\rho^{\frac{1}{2}} \mathbf{O}'\mathbf{x} + \rho^{\frac{1}{2}} \mathbf{I}'\mathbf{y}\right) \end{aligned} \qquad (2.28)$$

and inserting these in the fundamental R-matrix relation $\mathbf{V}=\mathbf{R}(\mathbf{D}-\mathbf{b}\mathbf{V})$,

$$\rho^{-\frac{1}{2}}\mathbf{O}\mathbf{x}+\rho^{-\frac{1}{2}}\mathbf{I}\mathbf{y}=\mathbf{R}\left[(\rho^{\frac{1}{2}}\mathbf{O}'\mathbf{x}+\rho^{\frac{1}{2}}\mathbf{I}'\mathbf{y})-\mathbf{b}(\rho^{-\frac{1}{2}}\mathbf{O}\mathbf{x}+\rho^{-\frac{1}{2}}\mathbf{I}\mathbf{y})\right] \,. \qquad (2.29)$$

Implicit in this action is the matching of the internal and external wave functions and derivatives. Rearranging expression (2.29) to resemble the definition of the U matrix,

$$\mathbf{x}=-\rho^{\frac{1}{2}}\mathbf{O}^{-1}[\mathbf{1}-\mathbf{r}(\rho\mathbf{O}'\mathbf{O}^{-1}-\mathbf{b})]^{-1}[\mathbf{1}-\mathbf{R}(\rho\mathbf{I}'\mathbf{I}^{-1}-\mathbf{b})]\mathbf{I}\rho^{-\frac{1}{2}}\mathbf{y} \,. \qquad (2.30)$$

Then defining the logarithmic derivative matrix $\mathbf{L} = [\,\rho\ \mathbf{O}'\ \mathbf{O}^{-1}\,]$, (2.31)

$$\mathbf{U} = \rho^{\frac{1}{2}}\mathbf{O}^{-1}[\mathbf{1}-\mathbf{R}(\mathbf{L}-\mathbf{b})]^{-1}[\mathbf{1}-\mathbf{R}(\mathbf{L}^{*}-\mathbf{b})]\mathbf{I}\rho^{\frac{1}{2}} \,. \qquad (2.32)$$

F. Scattering Amplitudes and Cross Sections

The connection between the collision matrix and differential cross sections is well-known and will only be outlined here (see e.g. Schiff 1969). The differential cross section for the reaction from channel (α,s,ν) to channel (α',s',ν') is given by definition as

$$d\sigma_{\alpha s\nu,\alpha' s'\nu'} = | A_{\alpha' s'\nu',\alpha s\nu} (\Omega_{\alpha'}) |^2 \, d\Omega_{\alpha'} \tag{2.33}$$

where $A_{\alpha' s'\nu',\alpha s\nu}$ is the amplitude of the asymptotic outgoing wave. This amplitude is obtained from the general expression for the wave function by specifying the incident wave to be a plane wave moving along the z-axis prepared in state (α,s,ν), distorted only by the Coulomb interaction. The amplitude thus obtained is

$$A_{\alpha' s'\nu',\alpha s\nu} (\Omega_{\alpha'}) = -\frac{\sqrt{\pi}}{k_\alpha} C_{\alpha'} (\theta_{\alpha'}) \, \delta_{\alpha' s'\nu',\alpha s\nu} \tag{2.34}$$

$$+ \; i \frac{\sqrt{\pi}}{k_\alpha} \sum_{\ell' m' \ell} \sqrt{2\ell+1} \left\{ e^{2i\omega_{\alpha'\ell}} \delta_{\alpha' s'\ell'\nu' m',\alpha s\ell\nu 0} - U_{\alpha' s'\ell'\nu' m',\alpha s\ell\nu 0} \right\} Y_m^{(\ell)} (\Omega_{\alpha'}) ,$$

where

$$C_\alpha (\theta_\alpha) = \frac{1}{\sqrt{4\pi}} \eta_\alpha \, \mathrm{cosec}^2\left(\frac{\theta_\alpha}{2}\right) \exp\left\{ - 2i\eta_\alpha \ln \sin\left(\frac{\theta_\alpha}{2}\right) \right\} \tag{2.35}$$

is the Coulomb amplitude. When this amplitude is squared the resulting cross section gives a sum of three terms: one due to pure Coulomb scattering, one due to nuclear scattering, and an interference term.

The final result for the cross section is obtained for unpolarized incident beam and target by summing over the ν' and averaging over the ν. After extensive simplification the final result is:

$$\frac{d\sigma_{\alpha s,\alpha' s'}}{d\Omega_{\alpha'}} = \pi k_\alpha^{-2} |C_{\alpha'}(\theta_{\alpha'})|^2 \delta_{\alpha' s',\alpha s}$$
$$+ [k_\alpha^2(2s+1)]^{-1} \sum_L B_L(\alpha' s',\alpha s) P_L(\cos\theta_{\alpha'})$$
$$+ \pi^{1/2}[k_\alpha^2(2s+1)]^{-1} \sum_{J\ell} (2J+1)\delta_{\alpha' s'\ell',\alpha s\ell}$$
$$\mathrm{Re}[iT^J_{\alpha' s'\ell',\alpha s\ell} C_{\alpha'}(\theta_{\alpha'}) P_\ell(\cos\theta_{\alpha'})] \quad . \tag{2.36}$$

where

$$B_L(\alpha' s',\alpha s) = \frac{1}{4}(-)^{s-s'} \sum_{J_1 J_2 \ell_1 \ell_2 \ell'_1 \ell'_2} \bar{Z}(\ell_1 J_1 \ell_2 J_2, sL)\, \bar{Z}(\ell'_1 J_1 \ell'_2 J_2, s'L)$$
$$\times (T^{J_1}_{\alpha' s'\ell'_1,\alpha s\ell_1})(T^{J_2}_{\alpha' s'\ell'_2,\alpha s\ell_2})^* \ , \tag{2.37}$$

where the T-matrix elements in the J representation are defined using the collision matrix in that representation as

$$T^J_{\alpha' s'\ell',\alpha s\ell} = e^{2i\omega_{\alpha'\ell'}} \delta_{\alpha' s'\ell',\alpha s\ell} - U^J_{\alpha' s'\ell',\alpha s\ell} \tag{2.38}$$

and U^J is related to U by

$$U^J_{\alpha' s'\ell',\alpha s\ell} = \sum_{\nu m \nu' m'} (s\ell\nu m|JM)\,(s'\ell'\nu' m'|JM)\, U_{\alpha' s'\nu'\ell' m',\alpha s\nu\ell m} \ ; \tag{2.39}$$

the $\bar{Z}$ coefficients are those of Blatt and Biedenharn (1952) as corrected by Huby (1954).

G. Single-level Formulas

While in general the cross sections given by the above formula are complicated for many channels and levels, it is possible to make approximations which yield simplified formulas. These are useful for developing intuition to guide the fitting of more complicated cross sections. The simplest of these is the Breit-Wigner one-level formula (2.42). It results

from considering only one of the basis levels λ .

In equation (2.31) the **L** matrix was introduced. The real and imaginary components of its elements have simple interpretations which are demonstrated in the one-level approximation. For a given channel,

$$L_c \equiv [\, \rho_c \, O_c' \, O_c^{-1} \,]_{r=c} = S_c + i\, P_c \,. \tag{2.40}$$

These are referred to as the shift function and the penetrability, and can be used in defining the level width and level shift for an isolated resonance in the following way:

$$\begin{aligned} \Gamma_{\lambda c} &= 2\, P_c\, \gamma_{\lambda c}^2 \\ \Delta_{\lambda c} &= -\,(S_c - b_c)\, \gamma_{\lambda c}^2 \quad . \end{aligned} \tag{2.41}$$

These definitions only apply in the assumption that no other levels exist at any energy, but similar quantities may be defined for less drastic assumptions. In this approximation the total cross section for a reaction proceeding from channel α to channel α' through isolated level λ with definite J and parity is

$$\sigma_{\alpha\alpha'} = \frac{\pi}{k_\alpha^2} \frac{2J+1}{(2I_1+1)(2I_2+1)} \frac{(\sum_{l+s=J} \Gamma_{\lambda c})(\sum_{l'+s'=J} \Gamma_{\lambda c'})}{(E_\lambda + \Delta_\lambda - E)^2 + \frac{1}{4}\Gamma_\lambda^2} \tag{2.42}$$

where I_1 and I_2 are spins of particles 1 and 2 and the sums are over channels which conserve parity.

For scattering from channel α into channel α (elastic scattering) the total cross section has a potential scattering term, an interference term, and a resonance term:

$$\sigma_{\alpha\alpha} = \frac{\pi}{k_\alpha^2}\left\{ 4\sum_{\ell}(2\ell+1)\sin^2\phi_{\alpha\ell} \right.$$

$$-\frac{(2J+1)}{(2I_1+1)(2I_2+1)}\Big(\sum_{\ell+s=J}\Gamma_{\lambda c}\Big)\left[\frac{(2(E_\lambda+\Delta_\lambda-E)\sin 2\phi_c+\Gamma_\lambda(1-\cos 2\phi_c)}{(E_\lambda+\Delta_\lambda-E)^2+\frac{1}{4}\Gamma_\lambda^2}\right]$$

$$\left. +\frac{(2J+1)}{(2I_1+1)(2I_2+1)}\frac{(\sum'\Gamma_{\lambda c})(\sum'\Gamma_{\lambda c'})}{(E_\lambda+\Delta_\lambda-E)^2+\frac{1}{4}\Gamma_\lambda^2}\right\} \quad (2.43)$$

Here the infinite Coulomb cross section is omitted, $\Gamma_\lambda = 2\Sigma P_c\gamma_{\lambda c}^2$ is the total width, and ϕ_c is the hard sphere phase shift given by $\phi_c = \tan^{-1}(F_c/G_c)$. The primed sums are over channels which conserve parity and which couple ℓ, s, ℓ', and s' to J.

The two-level formula for the total cross section (see e.g. Lane and Thomas 1958 or Nelson 1985) exhibits quite complicated interference between levels even in its simplest form .

CHAPTER III

EXPERIMENTAL EQUIPMENT AND PROCEDURES

In this chapter a brief overview will be presented of the equipment and methods used to perform the experiment. First the particle acceleration system will be described; the scattering chamber and detector arrangement is shown, and target preparation procedures will be outlined. Following that is a description of the charged particle signal processing. The procedures for data acquisition, and the automated acquisition system are explained in the next section, and finally the data reduction procedure is given.

A. Laboratory Equipment

Equipment in the TUNL High Resolution Laboratory includes a Van de Graaff accelerator, an electrostatic analyzer with associated fast feedback electronics, a scattering chamber, detectors and modular electronics for signal processing, and a VAX 11/750 minicomputer with the necessary interfacing and software. The description given here will be brief; many more details are given in the High Resolution Laboratory operating manual or in (Westerfeldt 1988). A schematic diagram of the laboratory is found in fig. 3.1.

1. Accelerator and Ion Source

The accelerator itself is an upgraded HVEC KN model Van de Graaff. It is a single-ended horizontal machine with a radio-frequency ionization ion source. Such an ion source can produce both atomic (H^+) and molecular (H_2^+) ionized hydrogen simultaneously. This property is crucial to the method of operation: the H^+ beam is used in the scattering experiment while the H_2^+ beam is used to measure online the energy fluctuations of both beams. During the course of this experiment the accelerator was

Figure 3.1 Schematic diagram of the High Resolution Laboratory and block diagram of the energy regulation systems.

High Resolution Laboratory and Control Systems

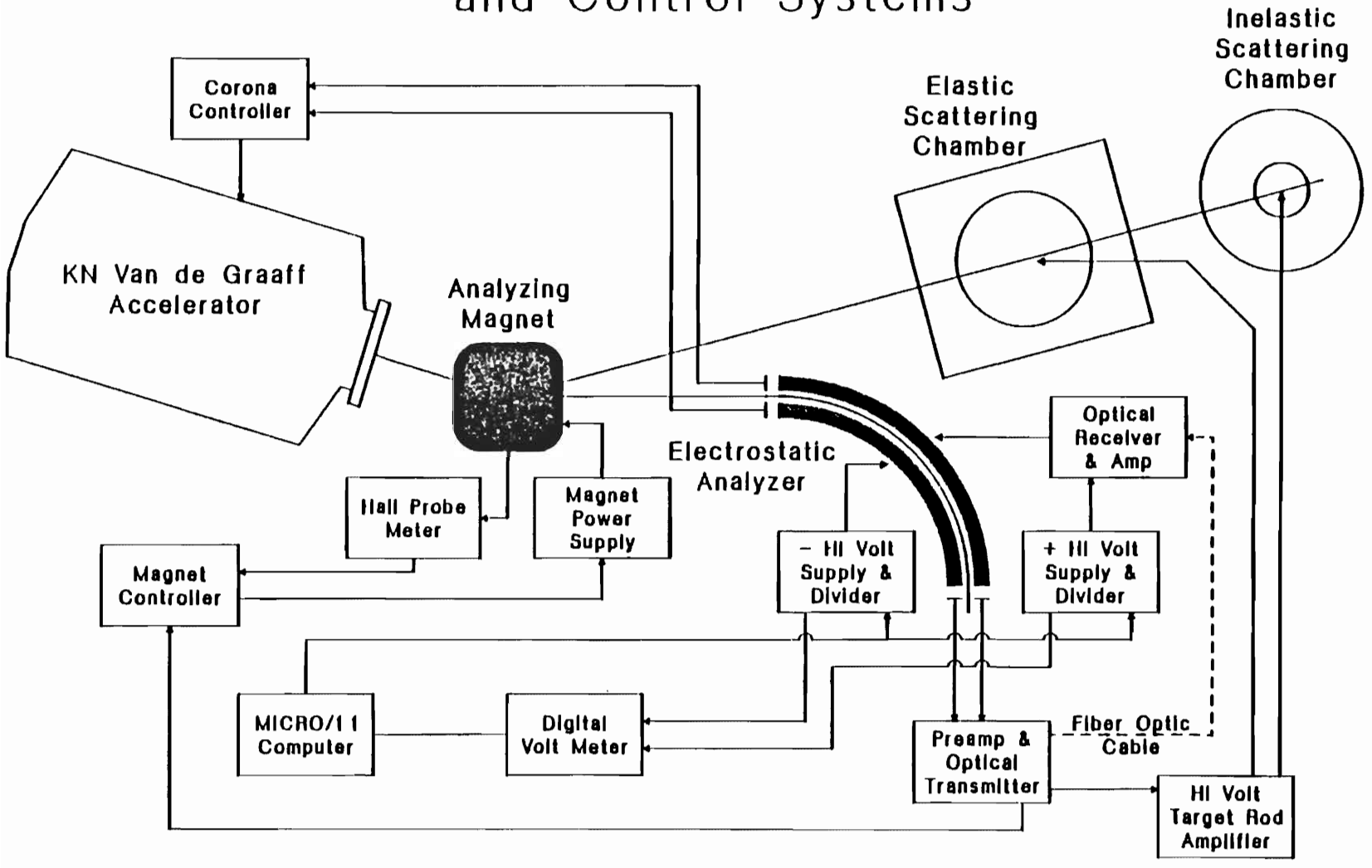

operated in the range 0.6 to 4.0 MV.

2. High Resolution System

The energy measurement is accomplished using a 90° section of a cylindrical electrostatic analyzer 1 m in radius. The composite beam emitted from the accelerator is split into the H^+ and H_2^+ beams by a bending magnet. The H_2^+ beam is focused and steered into the analyzer using only the accelerator focus electrode and the electrostatic steerers at the baseplate of the machine. The proton beam leg has sufficient beam optical elements to provide a proton beam on target focused to a ~1 mm spot. The H_2^+ beam passes between two horizontal corona control slits before entering the analyzer; these control slits serve as the object slits for the analyzer. With the inner and outer plates appropriately biased a focused image of those slits appears at the analyzer exit slits. The corona control feedback system regulates the accelerating potential in the large, slow fluctuations sufficiently well to keep the beam on the narrow entrance slits. If the H_2^+ beam is focused to a point at the corona control slits, then a difference signal from the exit slits provides a sensitive measurement of the faster energy fluctuations in the beam. This signal is primarily used in two ways: the H_2^+ beam is brought back to the center of the analyzer in a closed feedback loop, and the target is bias is changed to compensate for the energy fluctuations in the proton beam by an open feedback loop. There is also a low-pass-filtered loop feeding back to the bending magnet which compensates for any drift in the magnetic field.

3. Scattering Chamber and Collimators

A modified Ortec 17" scattering chamber (see figure 3.2) was used in this experiment. Five detectors were used at scattering angles normally between 90° and 165°. The detectors were solid-state surface barrier detectors with depletion regions ranging from one to five hundred microns in depth. Targets were mounted on a stainless steel rod in the center of the cylindrical chamber; this target rod was electrically isolated by a Teflon

Figure 3.2 Schematic diagram of the charged particle scattering chamber, showing the beam collimator assembly and detector arrangement.

Charged Particle Scattering Chamber

(Top View)

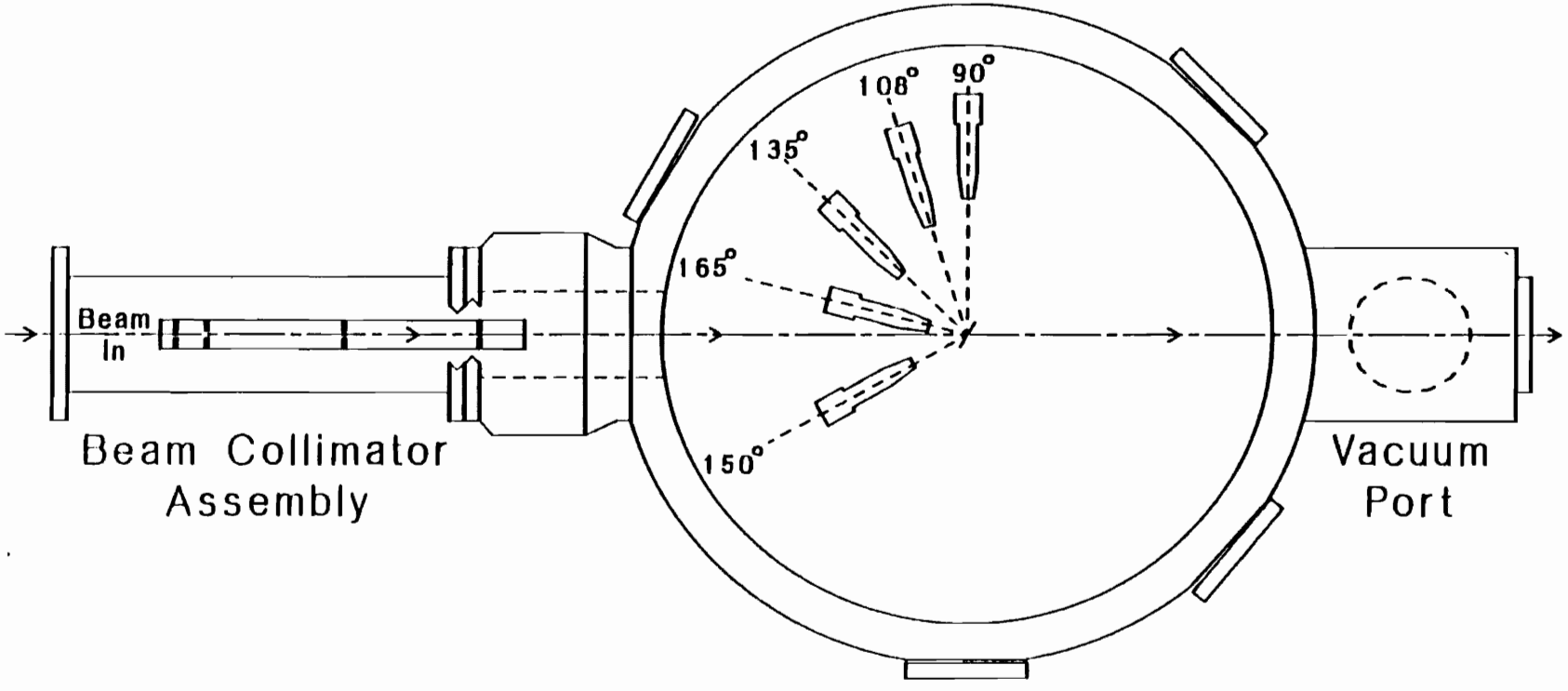

mount so that the target rod could be biased to compensate for the incident beam energy fluctuations.

A set of collimators was mounted in front of the scattering chamber to define a small beam spot on the target. Collimator sets were also mounted in front of each detector; the detector acceptance angle included the entire beam spot, but excluded the target mounting ring. The former was to prevent any fluctuations in beam trajectory from affecting the measured yield and the latter was to minimize noise in the spectrum due to protons which did not scatter directly from the target. A typical maximum background for the 165^{o} detector was less than one hundred counts of noise per hundred μC of charge, with the number of counts of interest of chlorine ranging from five to ten thousand.

4. Targets

The targets used for high resolution experiments in this laboratory are very specialized. They must be highly uniform in thickness, physically and chemically stable, and thin enough so that the average energy lost by the proton beam in passing through the target is much less than the experimental resolution of 300-400 eV. Since this thickness is on the order of 10 Å, a target backing must be used. This backing must be thin enough and made of a suitable material not to cause practical experimental difficulties such as extraneous counts which increase the system dead time, or cause radiation damage in the charged particle detectors. A typical compromise is to use physical vapor deposition of the target material onto a carbon backing a few $\mu g/cm^2$ thick. This method has worked with varying degrees of success. In this experiment it was found advantageous to deposit a layer of nickel on the carbon backing and then to heat the composite layer under vacuum before depositing the material of interest: without the nickel the target underwent severe chemical decomposition during the experiment. The details of the evolution of this preparation method are given in the appendix. One disadvantage of this method is that the charged particle spectrum has a peak due to elastic scattering from nickel. This peak increases the system dead time and at lower energies and

smaller scattering angles the elastic nickel peak may overlap the chlorine peak. As a result the background subtraction is more complicated and less reliable. Fortunately the bulk of the observed resonances are not in the energy region where this overlap poses a problem.

B. Signal Processing and Data Flow

1. Digitization of Charged Particle Signals

The outgoing particles were detected in silicon surface barrier detectors one to five hundred microns in thickness. This thickness is sufficient to stop the detected particles within the depletion zone. The output of the detectors is a current pulse which passes through a short cable of low capacitance, through a high voltage vacuum feedthrough and through another short coaxial cable, and through a precision 10 MΩ resistor to ground. The resulting voltage pulse is processed by a unity gain fast preamplifier. The output of this preamplifier is a spiked pulse which is sent through a long coaxial cable to the spectroscopy amplifier. These amplifiers boost the signal from less than a tenth of a volt to several volts, and shape the signal into pulses suitable for digitizing. This is performed with the minimum time constant available from the amplifier to decrease system dead time; the pulses are about one μs in duration. The output is in the form of a unipolar signal which is digitized to provide energy information and a bipolar signal which is utilized in several ways which are described below.

Since data were measured at five angles and only one analog-to-digital converter (ADC) was available, the five signals were multiplexed, with the outputs of the multiplexer being a single pulse on the line into the ADC and a three-bit binary number specifying the angle. The binary number is decoded into five parameter signals input to a CAMAC buffer module which then gates the ADC to accept the unipolar pulse. The ADC then digitizes the pulse within 8 to 10 μs and that binary word is combined in the hardwired interface with bits representing angle (and optionally other information) and this sixteen-bit number then is stored in

Figure 3.3 Block diagram of the data acquisition electronics.

Data Acquisition Electronics Setup

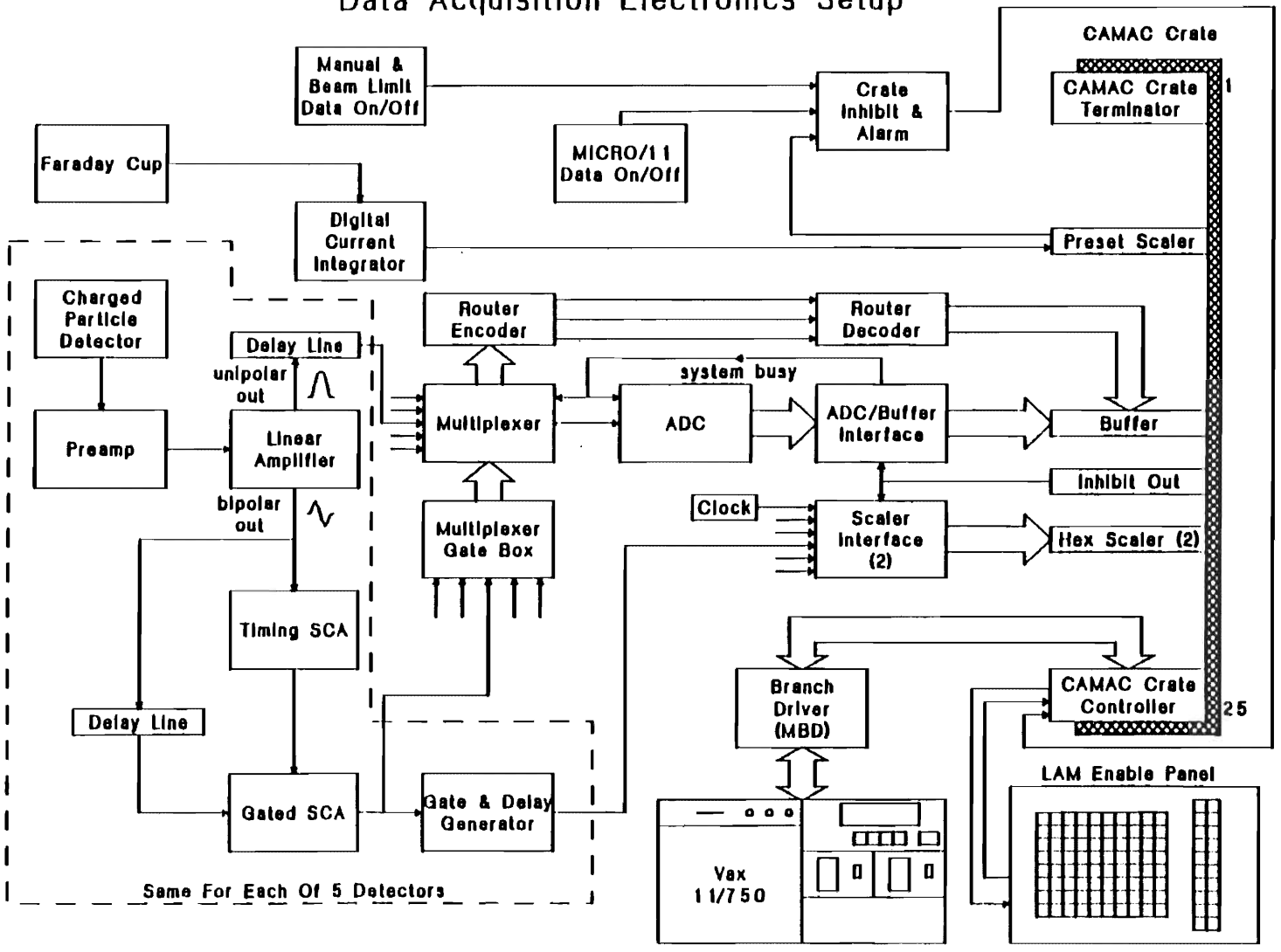

one of the two 256 word memory areas in the CAMAC ADC buffer. When this buffer is full its contents are dumped to a memory buffer in the VAX 11/750 via the Microprogrammable Branch Driver (MBD). Incoming data are then written to the other memory area, eliminating dead time due to the computer interrupt cycle time. A block diagram of the electronics is shown in figure 3.3.

Considerable system dead time is encountered using only the system just described. This is primarily due to digitizing the proton elastic scattering pulses from the carbon backings used to support the target material. These pulses are "gated out" before reaching the ADC. This is accomplished by delaying the unipolar signal out of the shaping amplifier two μs (an option built into the amplifier) and sending the bipolar signal into two cables. One line is passed through a single channel analyzer with a narrow window set on the peak corresponding to carbon, generating an output logic gate for each carbon pulse; the other is delayed 900 ns and then passes through a NIM module which optionally may be gated to reject pulses. When a carbon signal is identified by the first SCA a gate is sent to the second module which then rejects the bipolar signal. Signals which are not rejected enable the multiplexer to accept the unipolar signal; if not enabled the signal is ignored by the multiplexer.

The signals which are accepted by the multiplexer correspond to "good" pulses which are to be digitized. One other use made of the gate signal in this experiment was for approximate dead time correction. Each logic pulse not corresponding to carbon was stored in a scaler memory and read out when the preset value was reached. These correspond approximately to the actual pulses reaching the detector. The number from the scaler is compared with the total number of counts stored in each spectrum. The corresponding dead time correction factor is then used to correct the yield curves.

2. Sorting and Storage of Spectra

Once in the VAX buffers, the data are sorted using a low-level language (called "EVAL" for "Event Analysis Language"; for detailed information see

XSYS manual). It accesses a source file (file type ".EVL") designed by the experimenter which specifies the VAX memory area each datum is to be stored based on the angle information contained in the sixteen-bit data word. Once stored in the data areas the spectrum can be displayed on a graphics terminal and windows of interest may be set for calibration and yield acquisition purposes.

C. Data Acquisition Procedures and Automation

1. Determining and Incrementing Energy

The primary components of the beam energy regulation system include an electrostatic analyzer, two high voltage programmable power supplies of opposite polarity, a programmable digital multimeter, and a minicomputer. The minicomputer is interfaced to the high voltage power supplies, the multimeter, and the VAX 750 data acquisition computer. Additionally there is an analog feedback system consisting of a slit preamplifier, a magnetic field regulation circuit to regulate the main bending magnet field, a higfh voltage amplifier which biases the target, and the "homogenizer circuit" which provides an interface between the slit preamplifier and the magnet and target-biasing circuits.

The incident beam energy is determined when the H_2^+ beam is successfully transported through the electrostatic analyzer with the inner and outer plates properly biased. The entrance and exit slits and the plates themselves are set to such small separation distances (relative to the cylindrical radius of one meter) that only a very narrow range of particle energies is possible. The difference in the analyzer plate voltages is measured by a digital voltmeter; this is interfaced to a micro PDP/11 microcomputer which compares this number to a reference number and outputs a programming voltage to the two high voltage power supplies maintaining the analyzer biases. The system is designed to maintain zero potential in the central beam trajectory to avoid accelerating the beam in the

analyzer.

Thus when the average beam energy is that for which the inner and outer plates voltages are selected, the maximum beam is transported through the analyzer exit slits. Fluctuations about this average energy result in fluctuations in the current difference measured from the exit slits. This difference measurement is fed back to the outer plate (through an optical fiber link) to bring the beam back to the center of the analyzer. The difference signal is fed back to a high voltage target rod driver which changes the bias on the target rod to compensate for energy fluctuations in the proton beam.

2. Automating Data Acquisition

Warthen (1987) implemented an automated data acquisition system which allowed the measurement of yield curves without operator intervention required for long periods of time. In this system the microprocessor is continually running a control program which checks a terminal output from the VAX to determine the selected energy and then measures the difference between the analyzer plates. If there is a discrepancy of more than 20 eV between the two values the microprocessor inhibits the CAMAC crate, which stops the data flow. When the preset value of accumulated charge is reached, the data acquisition is inhibited and the experimental energy is incremented by the current energy step.

The microprocessor, upon referencing the new energy specified by the VAX, inhibits the CAMAC crate and steps up the voltage difference between the analyzer plates by incrementing the microprocessor output signal to the programmable high voltage power supplies. In this way the incident beam energy is increased; the bending magnet field increases appropriately through the slow feedback signal from the analyzer exit slits to the magnet power supply.

D. Obtaining Cross Sections from Spectra

1. Description of XSYS

The software used by the VAX 11/750 in processing the data in this experiment is called XSYS. Overviews of this system are available in several conference proceedings (Roberson 1981). XSYS consists of stand-alone FORTRAN modules which communicate with each other via permanently resident global sections of memory. The global sections contain all the data arrays, buffers, and control information.

The programs used in this experiment drew from both the general TUNL XSYS assortment of programs and from routines specialized to the High Resolution Laboratory. Some of the latter are modifications of standard XSYS programs and others are specific to this laboratory.

The set of programs used to select windows of interest, perform spectrum calibration, etc., were written mainly by Warthen (1987). Several peaks can be selected from each spectrum to be used for calibration purposes. After entering mass and Q-value information for the reactions of interest, the programs automatically set the windows of interest in each spectrum. The location and widths of the windows may be modified by the operator, and the method of background subtraction is selectable, with linear and polynomial background fitting available. A typical spectrum is shown in figure 3.4.

For the lower energies an alternative method was used. In the lowest energy range the elastic scattering peaks in the spectrum were too close together to allow reliable background subtraction. If a higher gain setting were used the (p,α_0) peak would not have been within the bounds of the spectrum. Therefore the method chosen was to fit the elastic peaks in the spectra using two gaussian peaks superimposed on a polynomial background. Although the CPU time required for the searches was much greater than in the previous method, for the most part this yielded excellent results.

2. Procedure for Generating Yield Curves

Spectra at five angles are measured until the preset scaler reaches its preset value. At this point the CAMAC crate is inhibited by the preset scaler

Figure 3.4 Charged particle spectrum at E_p = 3.4498 MeV and $\theta = 165^o$. The tallest peak is a doublet due to barium and a tantalum contaminant. The first peak to the left of this is due to nickel and the next peak to the left is due to chlorine. The first and second inelastic peaks are shown magnified by a factor of 50 and the peak due to the (p,α_o) reaction is shown magnified by a factor of 10.

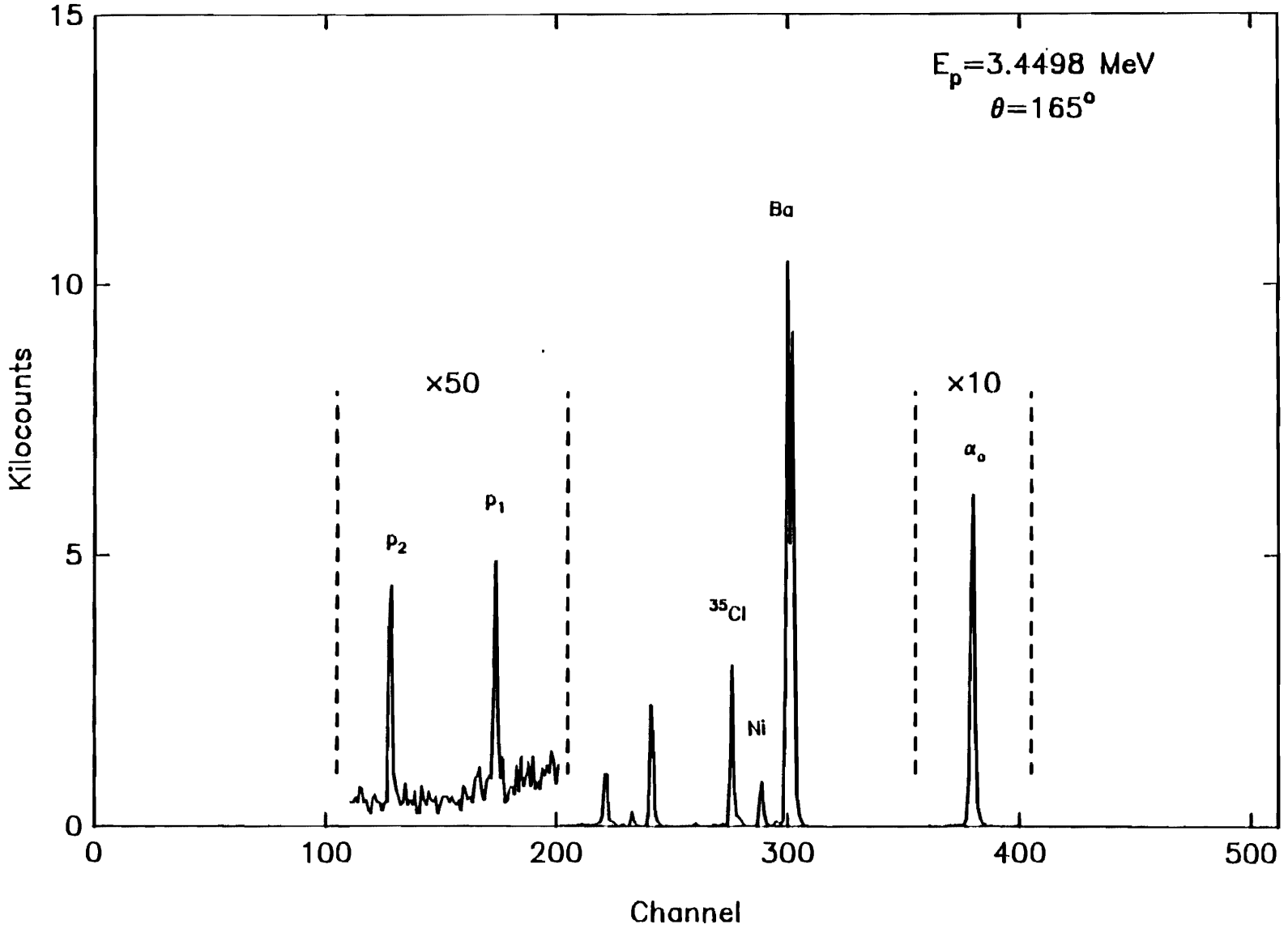
E_p=3.4498 MeV
θ=165°
Ba
×50
×10
α_o
p_1
p_2
^{35}Cl
Ni
Kilocounts
Channel
0
5
10
15
0
100
200
300
400
500

module and a command file (specified in the scaler ".DAP" file) is executed. In the earlier part of the experiment this was a master command file which in turn ran a series of other separate XSYS programs. These programs would do the following: dump spectra and scalers to tape; perform dead time calculations based on the scaler and spectra sums, and make a dead time correction to the spectra; shift the windows of interest (if necessary) to compensate for peaks which have been displaced from the previous positions because the incident energy has been changed; sum under the peaks of interest and store the sums in the yield curve data areas; increment the experimental energy value stored in memory; zero the spectra data areas to prepare for the next point; and remove the XSYS CAMAC crate inhibit. If the crate was not then inhibited by another input (such as the microPDP/11 or the data taker) the data flow would begin again at the new energy.

During the later stages of this experiment it became clear that an appreciable fraction of the time required to obtain the data was due to the time required to run each individual program from a command file. In stages of the experiment where each point required about a minute to obtain this processing time occupied 15 to 20% of the total active experimental time, or about one day of a week's run! Consequently efforts were made to reduce this processing time. The first significant reduction was the incorporation of the separate FORTRAN programs into a single master FORTRAN program. This reduced the processing time by 10 to 20%. An attempt was made to streamline the sorting program in the EVAL language. Although this had been an important effect in a previous coincidence experiment, this change made no significant improvements here.

The method finally adopted in the latter half of the experiment was designed and implemented primarily by Bull (1988). In this approach the master program is installed as a subprocess which is "hibernating" during the data acquisition. It is "awakened" by the scaler subprocess. This procedure takes only a few seconds to complete; significant improvement beyond this point probably is not possible with the present system.

CHAPTER IV

ANALYSIS OF RESONANCE DATA

In this chapter the data fitting program and the procedures for fitting data will be described. A number of examples of resonance curves are presented which show the resonance shapes as a function of the resonance parameters. At the end of the chapter several examples are presented of two-level interference effects which were observed in this analysis.

A. Description of MULTI6

The program used to generate the theoretical cross sections for data fitting in this experiment is called MULTI6. It is a FORTRAN code originally written by Sellin (1969) and modified by others over the years. It accepts parameters for the entrance and exit channels such as the projectile and target masses, the reaction Q-values, the allowed channel spins and orbital angular momentum values. The variable parameters are the resonance energies, total angular momenta, channel spins, orbital angular momenta, partial widths, and the sign of the reduced width amplitude associated with each partial width. The cross section calculation includes Coulomb, "hard sphere," and resonance scattering, and is based on the differential cross section formulae given in Lane and Thomas (1958).

Currently the program considers up to 300 levels, 12 J^{π} values, 5 groups of decay channels, ℓ values up to 5, and up to 10 channels for a given J^{π}. The theoretical cross sections calculated by the program are convoluted with a resolution function to simulate the finite resolution of the system plus straggling effects in the target. Empirically a Gaussian function with a Lorentzian leading edge fitted (p,α) resonance shapes well, and was therefore used as the resolution function. This function was specified by a Gaussan FWHM and the ratio of the Lorentzian FWHM to the Gaussian

width. These quantities were determined by fitting a narrow resonance; for a given target and tuning they were constant, and the numbers were nearly the same from one target and tuning to the next.

The fitting procedure was simply to input the adjustable resonance parameters, calculate the convoluted theoretical cross section, normalize the data to the theoretical cross section and visually evaluate the fit. The resonance parameters are then adjusted and the cross section is calculated again and compared to the normalized data. The strategy involved in choosing parameters which converge to a fit will be described in the next section.

B. Fitting procedures

1. Basic Fitting Approach

The formula for the differential cross section given in equation (2.36) includes many levels and channels and takes into account several types of complicated phenomena. Underlying the intuitive approach taken in analyzing the data is the idea that the single-level resonance formulae provide a guide to fitting more complicated resonance shapes. The Breit-Wigner formula in equation (2.42) for $\sigma_{p\alpha}$ is reproduced here in simplified form specialized to a (p,α_0) reaction for one entrance width in which only the p_0 and α_0 decay channels are open:

$$\sigma_{p\alpha}(E) = \frac{\pi}{k_p^2}(2J+1)\frac{\Gamma_p\Gamma_\alpha}{(E_0+\Delta-E)^2+\frac{1}{4}(\Gamma_p+\Gamma_\alpha)^2} \quad . \tag{4.1}$$

This corresponds to a Lorentzian lineshape with a FWHM of $\Gamma=\Gamma_\alpha+\Gamma_p$. The maximum value occurs at $E = E_0+\Delta$ and is proportional to

$$(2J+1)\frac{\Gamma_p\Gamma_\alpha}{\Gamma_p+\Gamma_\alpha} \quad . \tag{4.2}$$

Thus in fitting a resonance with this formula the height of the peak may be increased by increasing J; increasing Γ_p or Γ_α up to the value of $\Gamma_p = \Gamma_\alpha$ has the same effect, but also broadens the total width. In practice the elastic

channel is used to estimate Γ_p and J. The level shift Δ may be set equal to zero by allowing the boundary condition parameter b_c to be equal to the shift function (see equation (2.41)) which varies slowly with energy (see Fang 1987 for discussion). The entire cross section is weighted by $1/k^2 = 1/E$, which changes somewhat the effect of a given set of J, Γ_p, and Γ_α over the range of several MeV. For example, for constant width, from 1 to 4 MeV there is a factor of 4 difference in the observed height of the peak. In obtaining reduced width magnitudes from the partial widths there is the additional effect of the penetrability function (see equation (2.41)). The penetrability functions are plotted in fig. 4.1.

The effects of other open channels on the resonance shape is small. Other open exit channels increase the total width of the resonance and therefore decrease the maximum height. The complication of several entrance widths affects the angular distribution; the entrance channel mixing must be inferred from the angular distribution. Only one exit channel width is allowed for the (p,α_0) reaction in this experiment; in other channels such as (p,α_1) or (p,p_1) several partial decay widths are allowed. Angular distributions for the (p,α_0) reaction for isolated resonances are discussed at length in Vanhoy (1986).

The Breit-Wigner formula given in equation 4.1 describes the total cross section as a function of energy, and gives a general, qualitative guide to fitting the data measured in this experiment. The formula used to generate the theoretical fit has been presented in equation 2.36. This formula describes the multilevel, multichannel differential cross section.

Table 4.1 lists the open channels in this experiment for elastic scattering, considering ℓ values up to $\ell = 3$. There are twenty-four open channels. The open channels for inelastic scattering to the first and second excited states of ^{35}Cl are listed in tables 4.2 and 4.3, respectively. There are fourteen channels open for the p_1 channel and thirty channels open for the p_2 channel, considering ℓ values up to $\ell = 3$. In the $^{35}Cl(p,\alpha_0)^{32}S$ reaction there are only four channels open for $\ell < 4$, since the total angular momentum of ^{32}S is zero. This requires $J = \ell$ for the (p,α_0) channel, which helps to reduce the number of possible fitting parameters for

Figure 4.1 The Coulomb penetrability for elastic scattering as a function of energy and orbital angular momentum.

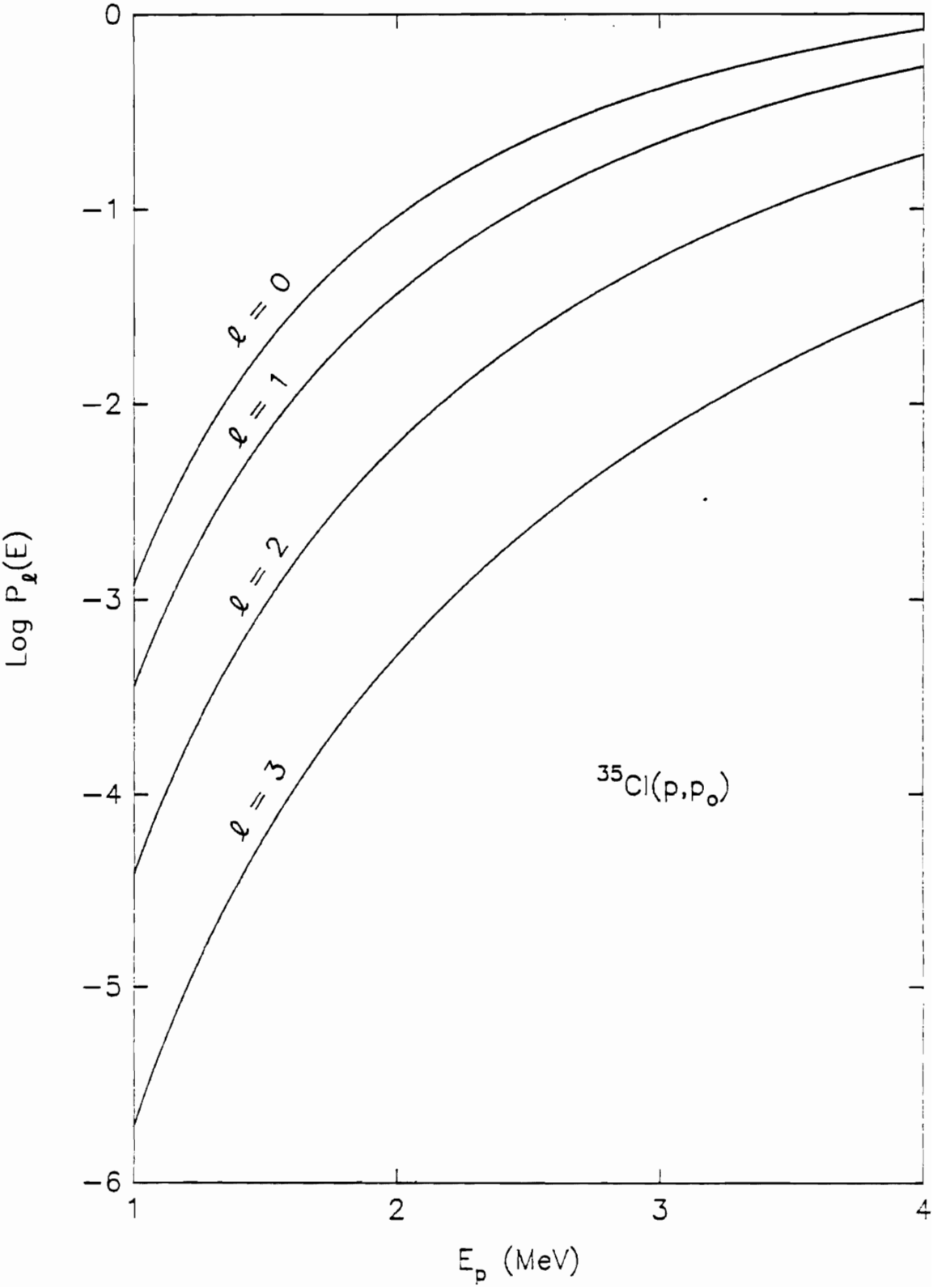
0
−1
−2
−3
−4
−5
−6
1
2
3
4
Log $P_\ell(E)$
E_p (MeV)
$\ell = 0$
$\ell = 1$
$\ell = 2$
$\ell = 3$
$^{35}Cl(p,p_o)$

Table 4.1

Allowed Channels for Elastic Scattering

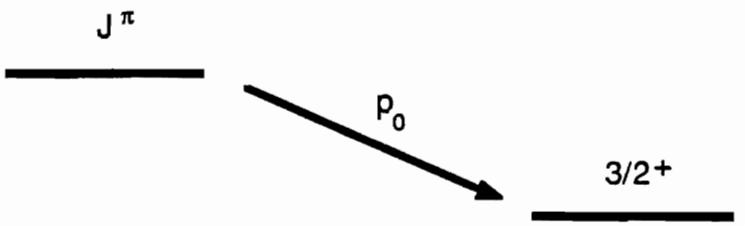

$^{35}Cl(p,p_0)$; I = 3/2					
J^π	Channels		J^π	Channels	
0^-	s=1	ℓ=1	2^+	s=1	ℓ=2
				s=2	ℓ=0
0^+	s=2	ℓ=2		s=2	ℓ=2
1^-	s=1	ℓ=1	3^-	s=1	ℓ=3
	s=2	ℓ=1		s=2	ℓ=1
	s=2	ℓ=3		s=2	ℓ=3
1^+	s=1	ℓ=0	3^+	s=1	ℓ=2
	s=1	ℓ=2		s=2	ℓ=2
	s=2	ℓ=2			
			4^-	s=1	ℓ=3
2^-	s=1	ℓ=1		s=2	ℓ=3
	s=1	ℓ=3			
	s=2	ℓ=1	4^+	s=2	ℓ=2
	s=2	ℓ=3			
			5^-	s=2	ℓ=3

Table 4.2

Allowed Channels for Inelastic Scattering

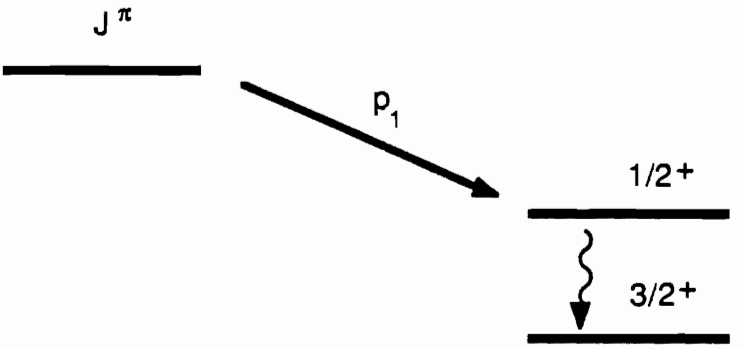

$^{35}Cl(p,p_1)$					
J^π	Channels		J^π	Channels	
0^-	s=1	ℓ=1	2^+	s=0	ℓ=2
				s=1	ℓ=2
0^+	s=0	ℓ=0			
			3^-	s=0	ℓ=3
1^-	s=0	ℓ=1		s=1	ℓ=3
	s=1	ℓ=1			
			3^+	s=1	ℓ=2
1^+	s=1	ℓ=0			
	s=1	ℓ=2	4^-	s=1	ℓ=3
2^-	s=1	ℓ=3			
	s=1	ℓ=1			

Table 4.3

Allowed Channels for Inelastic Scattering

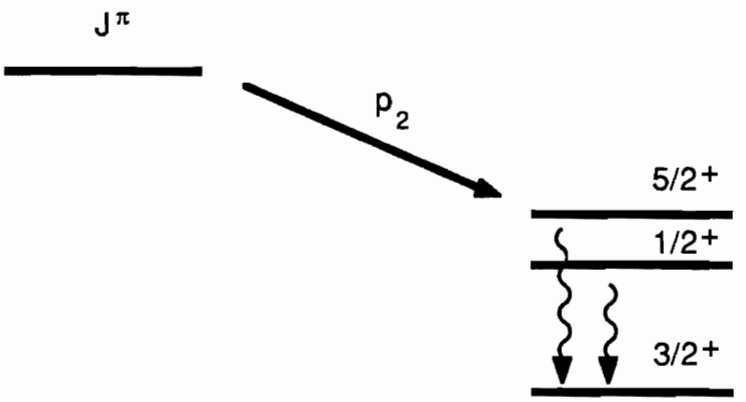

$^{35}Cl(p,p_2)$					
J^π	Channels	J^π	Channels	J^π	Channels
0^-	s=3 ℓ=3	2^+	s=2 ℓ=0	4^-	s=3 ℓ=1
			s=2 ℓ=2		s=2 ℓ=3
0^+	s=2 ℓ=2		s=3 ℓ=2		s=3 ℓ=3
1^-	s=2 ℓ=1	3^-	s=2 ℓ=1	4^+	s=2 ℓ=2
	s=2 ℓ=3		s=3 ℓ=1		s=3 ℓ=2
	s=3 ℓ=3		s=2 ℓ=3		
			s=3 ℓ=3	5^-	s=2 ℓ=3
1^+	s=2 ℓ=2				s=3 ℓ=3
	s=3 ℓ=2	3^+	s=3 ℓ=0		
			s=2 ℓ=2	5+	s=3 ℓ=2
2^-	s=2 ℓ=1		s=3 ℓ=2		
	s=3 ℓ=1			6-	s=3 ℓ=3
	s=2 ℓ=3				
	s=3 ℓ=3				

resonances decaying into this channel. In total there are sixty-eight open decay channels for $\ell < 4$ which contributed appreciably in this experiment. At the higher energies the (p,α_1) and (p,p_3) channels were also open but were not observed appreciably, and the (p,α_2), (p,p_4), (p,p_5), and (p,p_6) channels were open but were completely suppressed by the Coulomb penetrability effects.

The fitting parameters for each resonance do not all have the same kind of effect on the resonance shape; modifying a given parameter will affect the resonance shape in a distinct way, which often provides unambiguous parameter assignments. The method for assigning each parameter value in the analysis will be described below.

In the resonance analysis for this experiment the orbital angular momentum (and therefore the parity $(-1)^{\ell}$)of any isolated resonance is usually apparent from the resonance shape at different angles, as can be seen in figure 4.2. For resonances with widths greater than the experimental resolution there is little ambiguity in this assignment; as is seen in figure 4.2, the shapes are quite distinctive for pure ℓ values.

For a given ℓ value the spin of the resonance is usually well determined by the vertical excursion of the shape at a back angle. In all elastic cross section plots which follow there is only the elastic scattering channel open, i.e. $\Gamma_p = \Gamma_{total}$. In figure 4.3 the shapes for s-wave resonances at $\theta = 165^o$ are plotted. The higher spin value has the greater vertical excursion at this angle. The shapes for various spin values are plotted in figures 4.3 through 4.6 for ℓ values of 0, 1, 2, and 3.

Since the target spin is 3/2 in this experiment, both ℓ mixing and s mixing are allowed. An example of channel spin mixing is shown at $\theta = 165^o$ and $\theta = 90^o$ in figure 4.7 for 1^- p-wave resonances. In this plot, three values of the channel spin mixing ratio are shown. The channel spin mixing ratio is defined by

$$\xi_n = \frac{\sum_{\ell} \Gamma_{n,s,\ell}}{\Gamma_n} \qquad (4.3)$$

Figure 4.2 Variation in resonance shape as a function of angle and ℓ value.

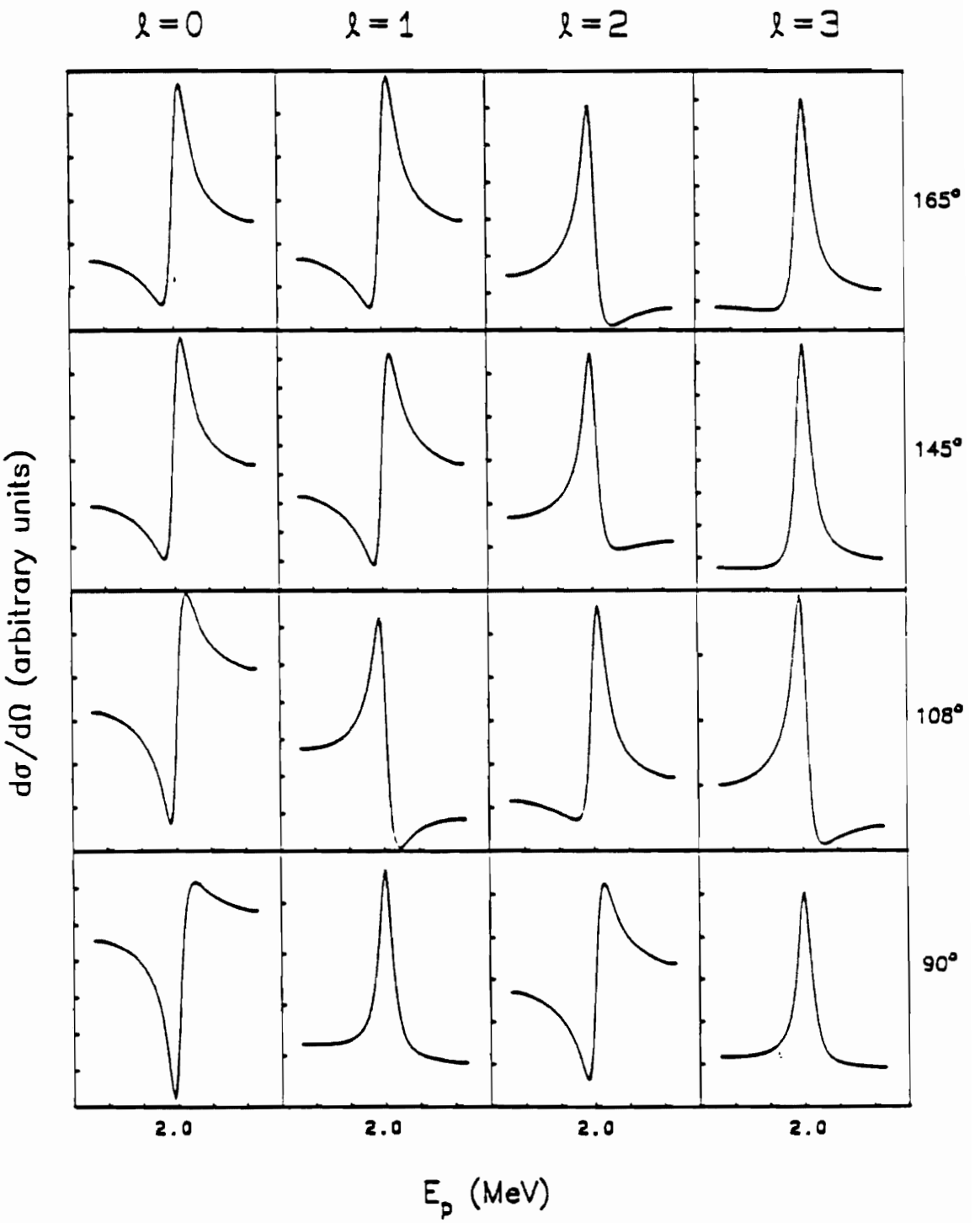
ℓ = 0
ℓ = 1
ℓ = 2
ℓ = 3
165°
145°
108°
90°
dσ/dΩ (arbitrary units)
2.0
2.0
2.0
2.0
E_p (MeV)

Figure 4.3 Variation in s-wave resonance shape with J value at $\theta = 165^{o}$.

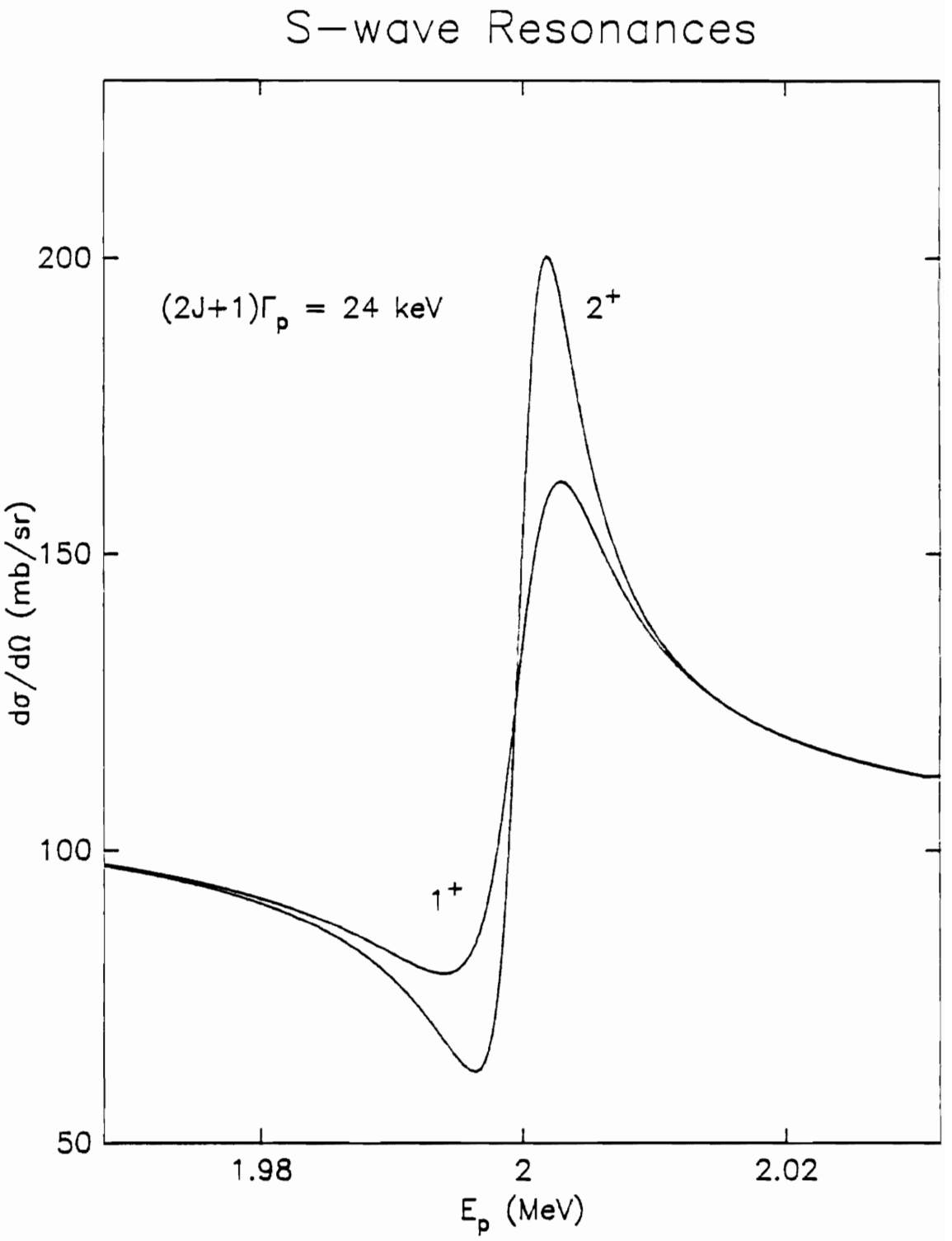
S—wave Resonances
200
150
100
50
$(2J+1)\Gamma_p$ = 24 keV
2^+
1^+
$d\sigma/d\Omega$ (mb/sr)
1.98
2
2.02
E_p (MeV)

Figure 4.4 Variation in p-wave resonance shapes with J value for s = 2 at 165^{o}.

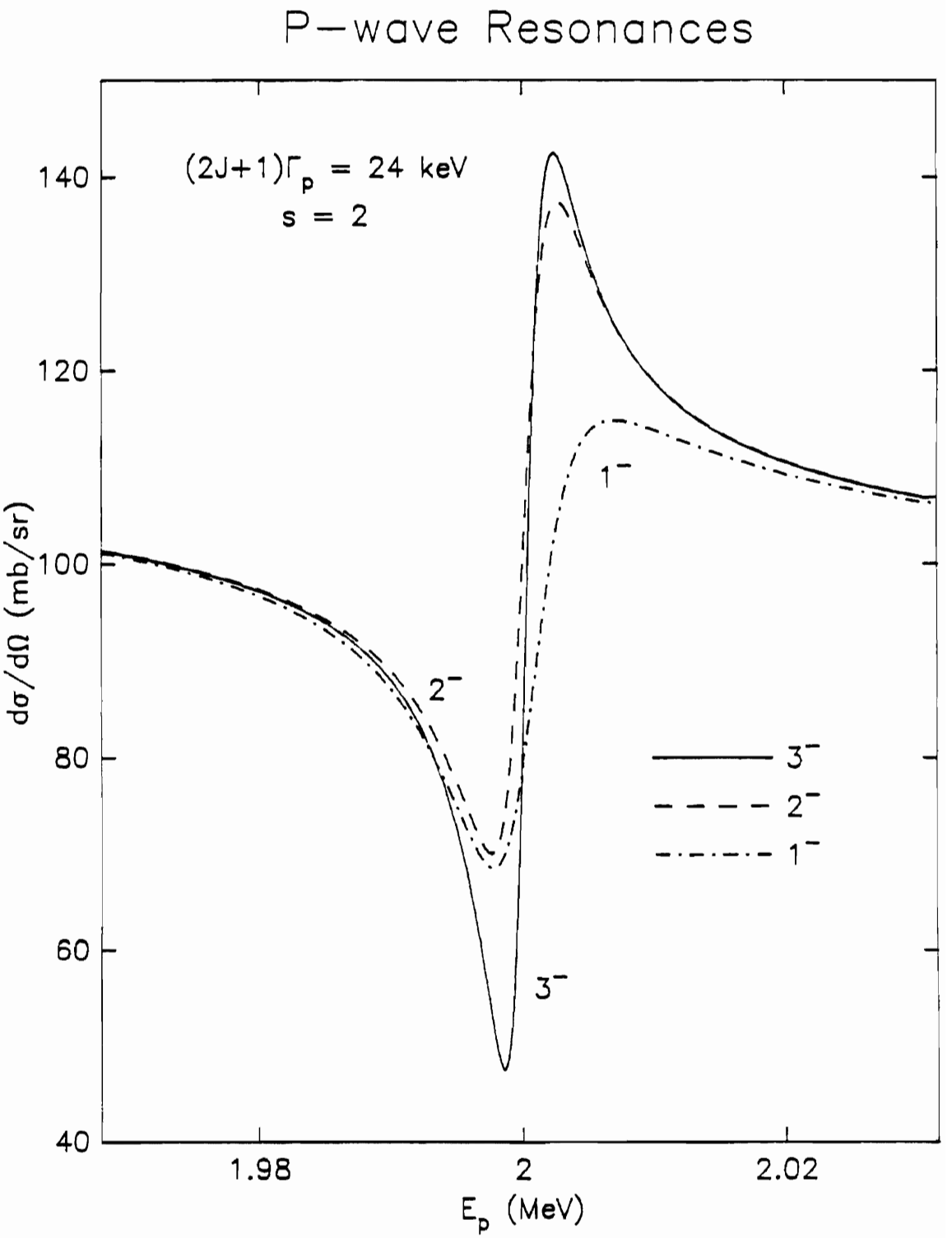
P—wave Resonances
(2J+1)Γp = 24 keV
s = 2
140
120
100
80
60
40
dσ/dΩ (mb/sr)
1.98
2
2.02
Ep (MeV)
2⁻
1⁻
3⁻
3⁻
2⁻
1⁻

Figure 4.5 Variation in d-wave resonance shape with J value for s = 2 at 165^{o}.

D—wave Resonances

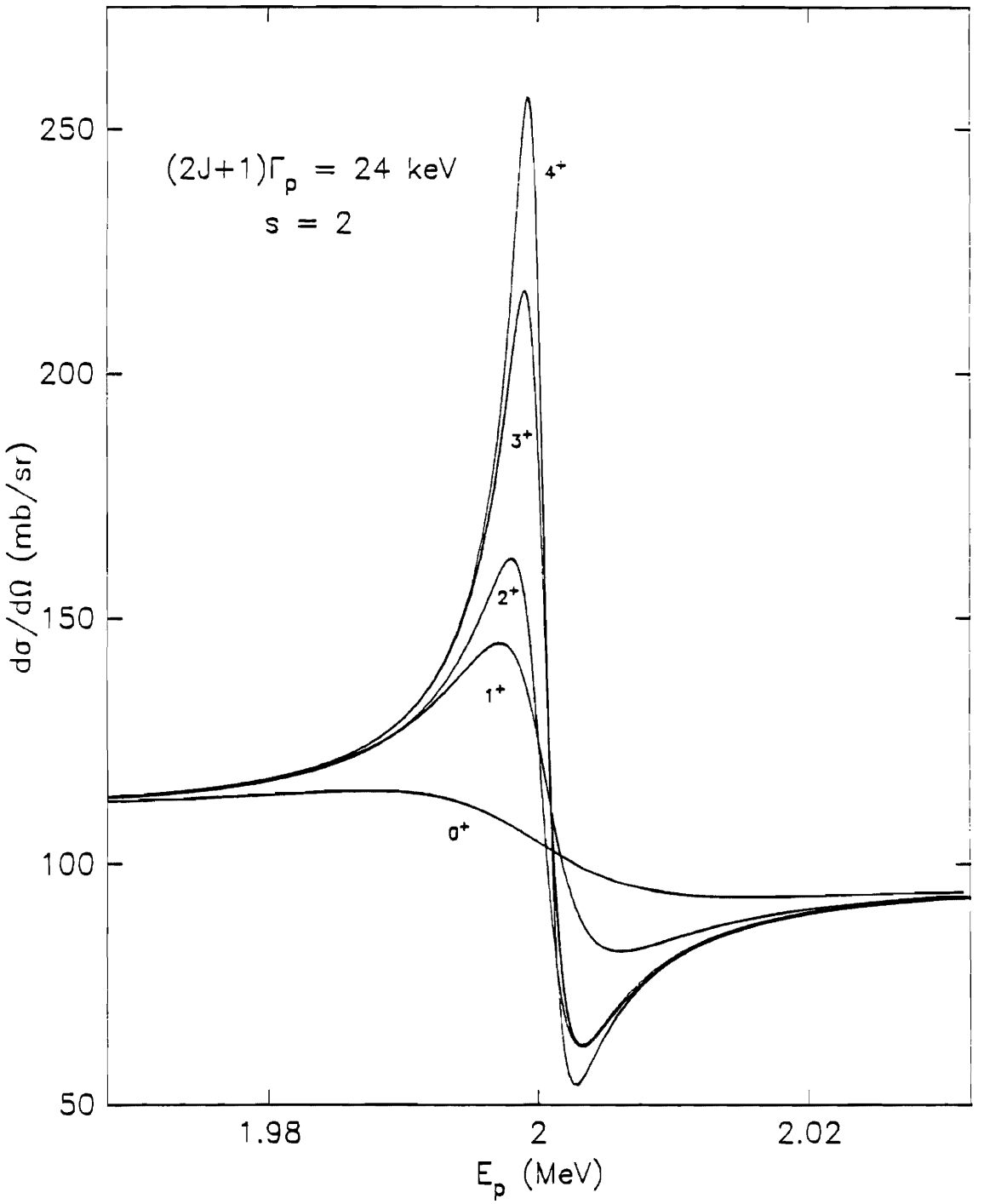

Figure 4.6 Variation in f-wave resonance shape with J value for s = 2 at 165^{o}.

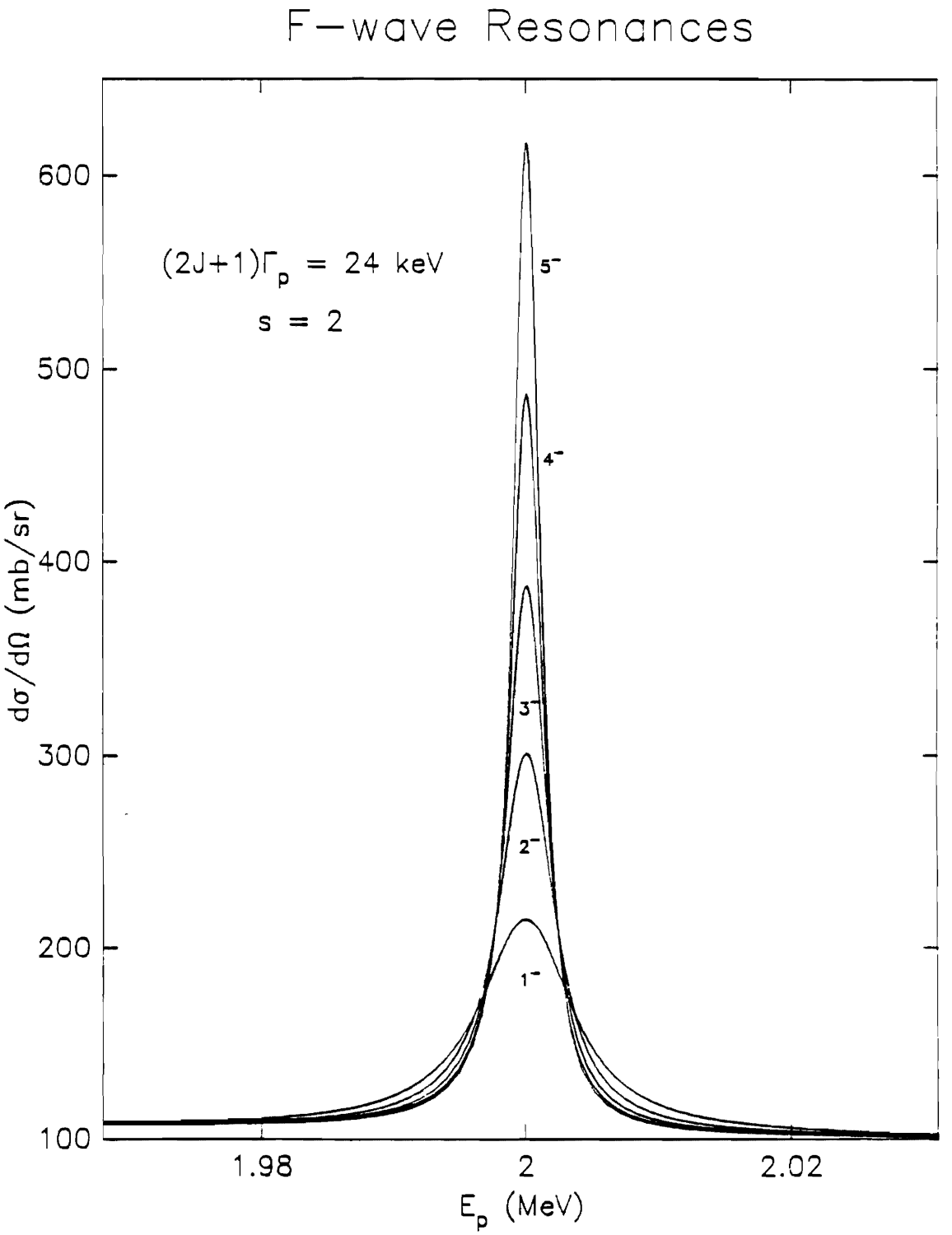
F—wave Resonances
(2J+1)Γp = 24 keV
s = 2
5⁻
4⁻
3⁻
2⁻
1⁻
600
500
400
300
200
100
dσ/dΩ (mb/sr)
1.98
2
2.02
Ep (MeV)

Figure 4.7 Variation in shape for 1^-, ℓ =1 resonances with channel spin mixing at 90^o and 165^o. The intermediate value plotted is for $\xi = 0.5$. The differential cross section is more sensitive to the channel spin mixing ratio for values of ξ close to 0 than it is for values close to 1.

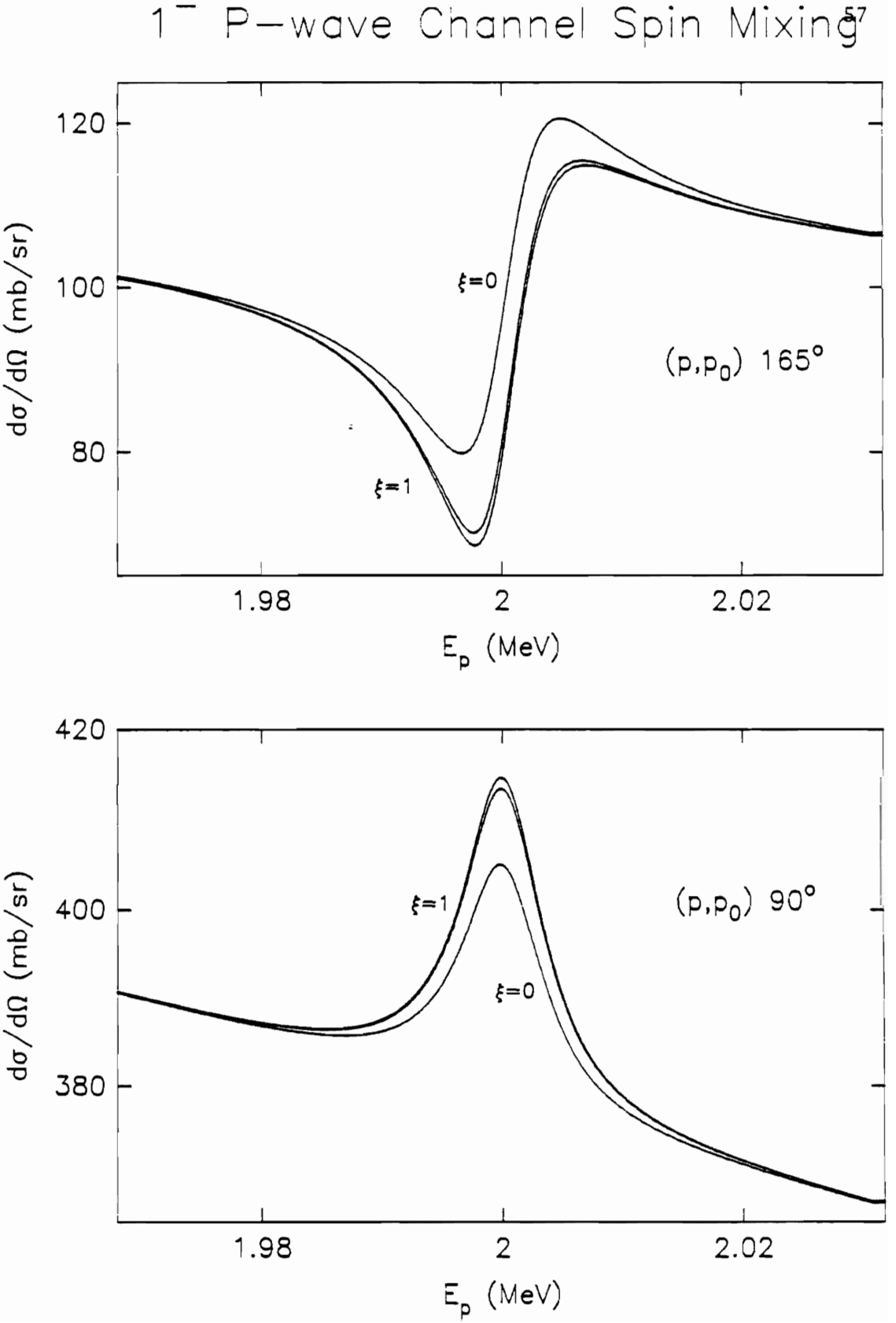
1⁻ P−wave Channel Spin Mixing
120
100
80
dσ/dΩ (mb/sr)
ξ=0
ξ=1
(p,p0) 165°
1.98
2
2.02
Ep (MeV)
420
400
380
dσ/dΩ (mb/sr)
ξ=1
ξ=0
(p,p0) 90°
1.98
2
2.02
Ep (MeV)

Figure 4.8 Variation in shape for 2^+, ℓ =2 resonances with channel spin mixing at 90^o and 165^o . The intermediate values shown are 25% increments in laboratory widths. Note that in this case the curve for ξ = 1 is not the most different from that for ξ = 0, but rather an intermediate value for ξ is most different.

2^+ D—wave Channel Spin Mixing[59]

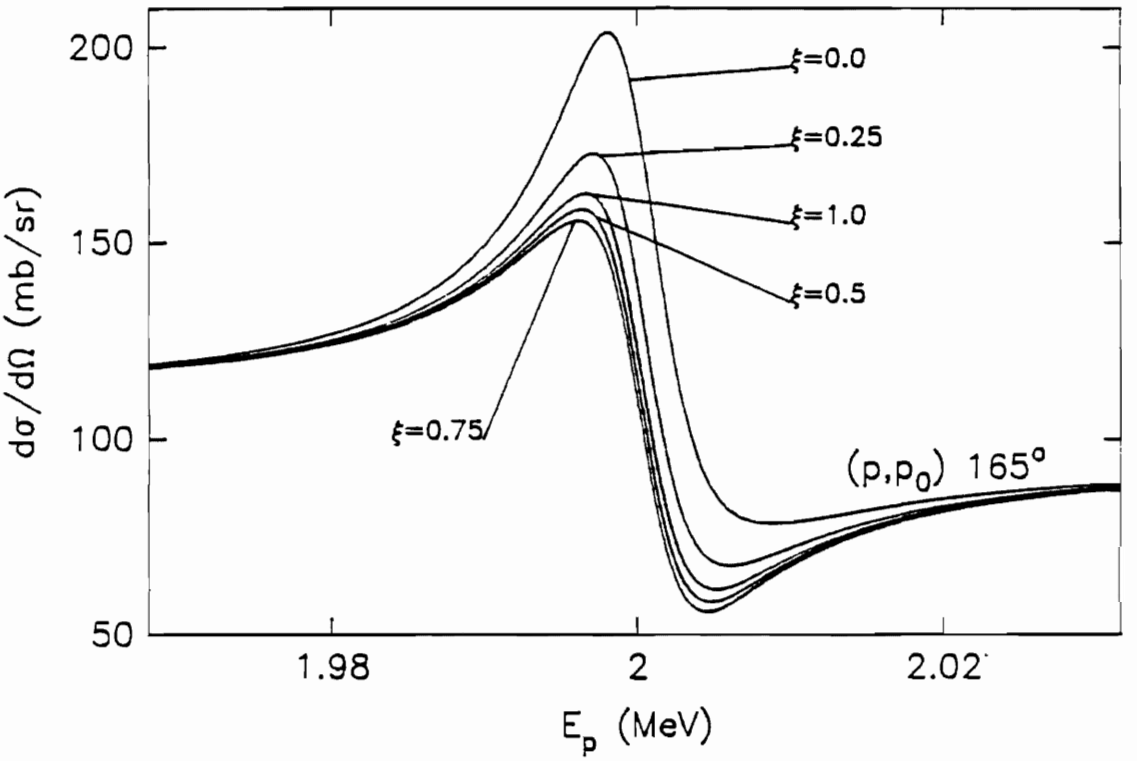

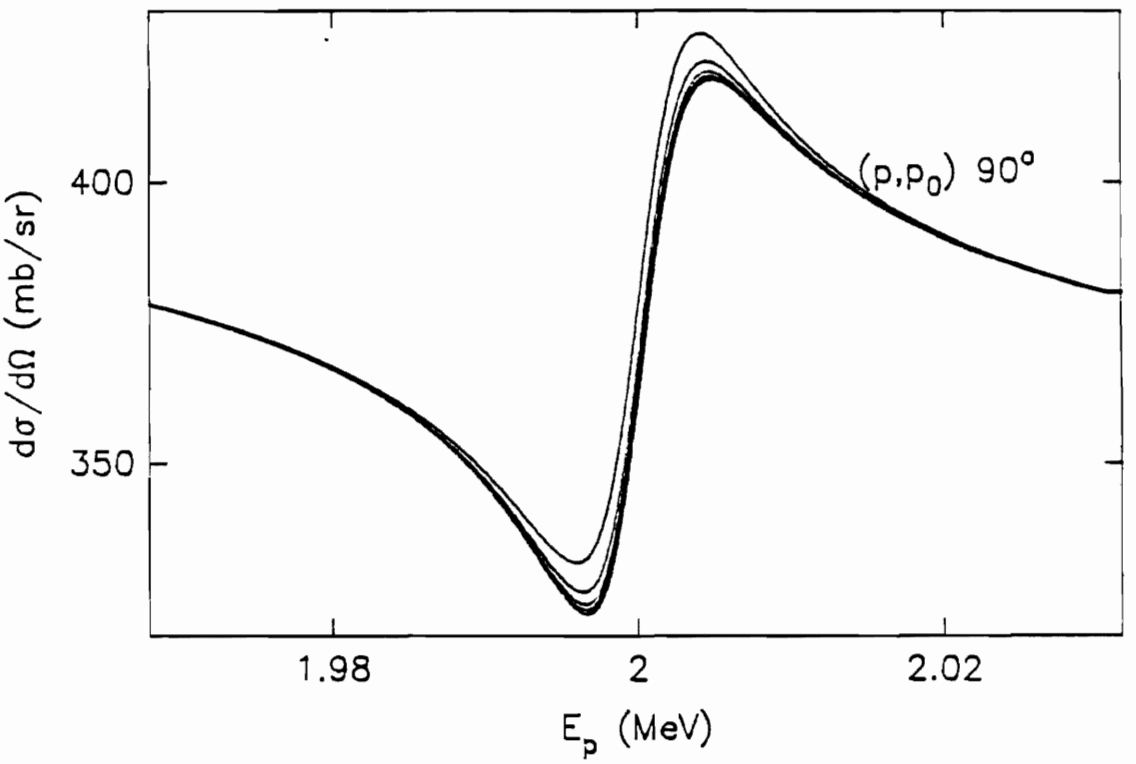

and thus is equal to zero for pure s = 1 and is equal to one for s = 2. In figure 4.8 is shown channel spin mixing for 2^+ d-wave resonances. In this plot it can be seen that an unambiguous assignment for channel spin mixing may be impossible to make based on the 165° elastic scattering shape, since the shape is not single-valued as a function of channel spin. It is often possible to make assignments based on elastic data at other angles or on the angular distributions of reaction products, if these are seen for a given resonance. To make a reliable assignment often requires measurements with much higher counting statistics (in the reaction channel) than were performed in this experiment to make a reliable assignment.

Orbital angular momentum mixing, by contrast, has a more distinct signature in the elastic scattering. In figures 4.9 and 4.10 are shown resonance shapes for 2^+ s- and d-wave mixing and for 2^- p- and f- wave mixing for several values of the orbital angular momentum mixing angle. This angle is defined by (Nelson 1985)

$$\psi_{ns} = \tan^{-1}\left(\pm \sqrt{\frac{\Gamma_{n,s,\ell+2}}{\Gamma_{n,s,\ell}}} \right) \qquad (4.4)$$

2. Multilevel Interference

While description of the basic fitting approach in the previous section provides a guide to fitting the data measured in this experiment, it does not account for level-level interference. For a $J^\pi = 3/2^+$ target both ℓ and s mixing can occur simultaneously. In regions where strong level-level interference occurs this makes data fitting much more complicated, although if a very good fit is obtained this also is an argument for near-uniqueness of the fitting parameters. In this section these effects will be discussed.

Multilevel interference is the distortion of the shape of an isolated resonance due to the presence of another nearby resonance. Two-level effects are discussed in Nelson (1985) and Fang (1987). Multilevel interference can show a number of effects which are difficult to categorize systematically. One typical effect occurs when a variety of small and

Figure 4.9 Variation in shape for 2^+ resonances with ℓ mixing at 90^o and 165^o . The intermediate values shown are 25% increments in laboratory widths.

2^+ S–wave and D–wave Mixing

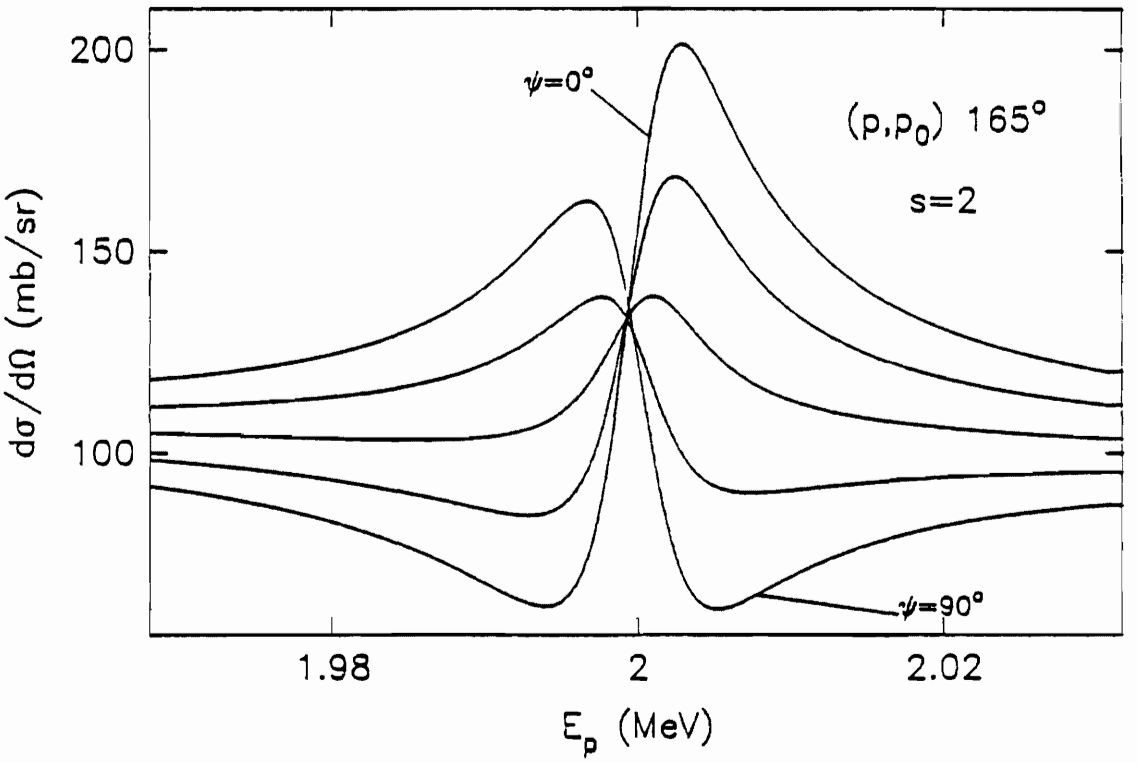

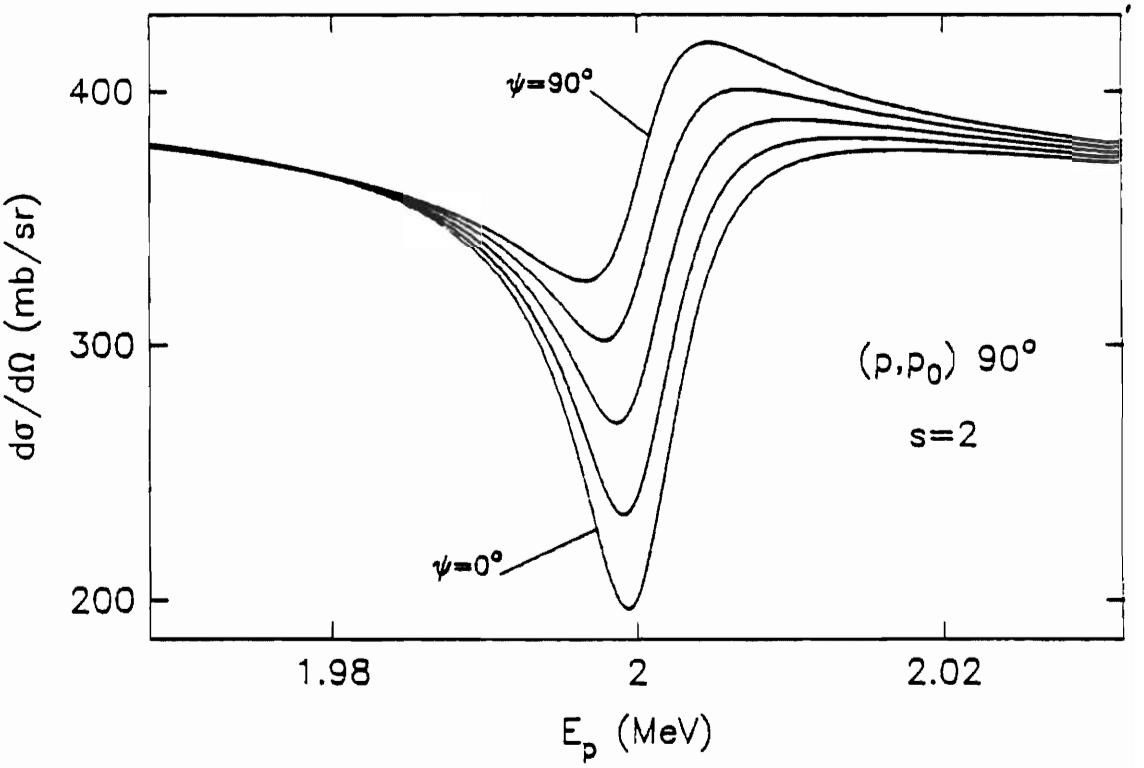

Figure 4.10 Variation in shape for 2^- resonances with ℓ mixing at 90^o and 165^o. The intermediate values shown are 25% increments in laboratory widths.

2^- P–wave and F–wave Mixing[64]

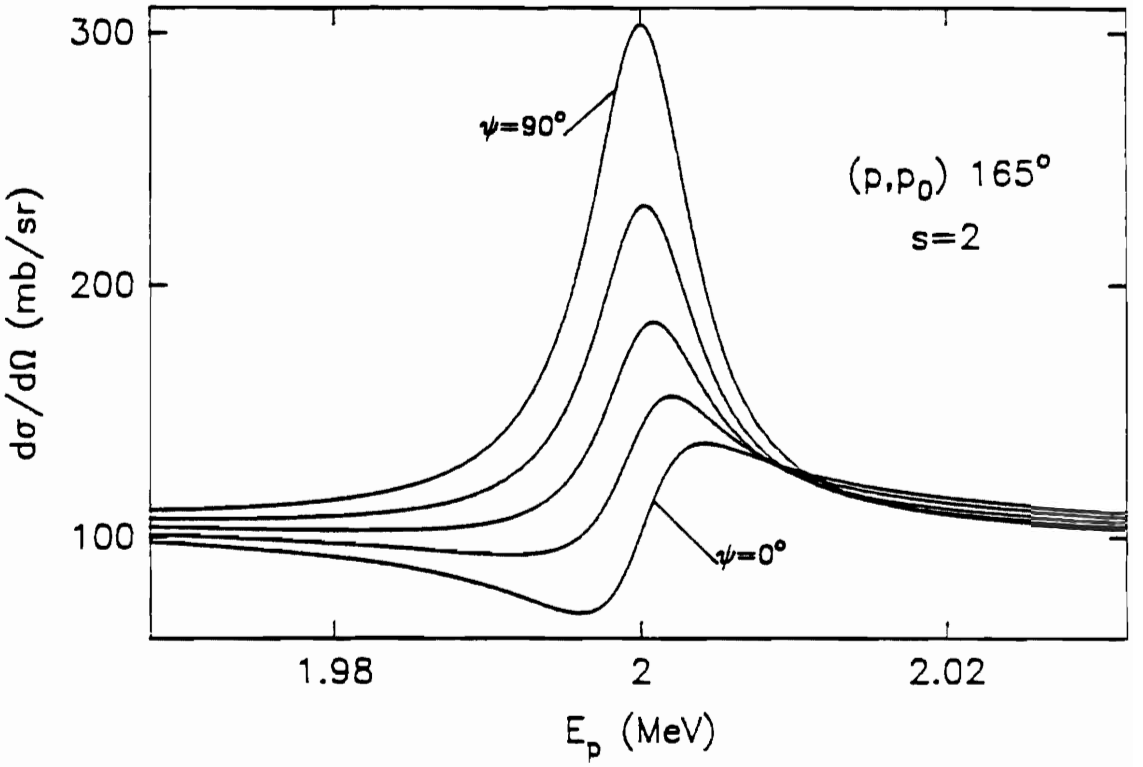

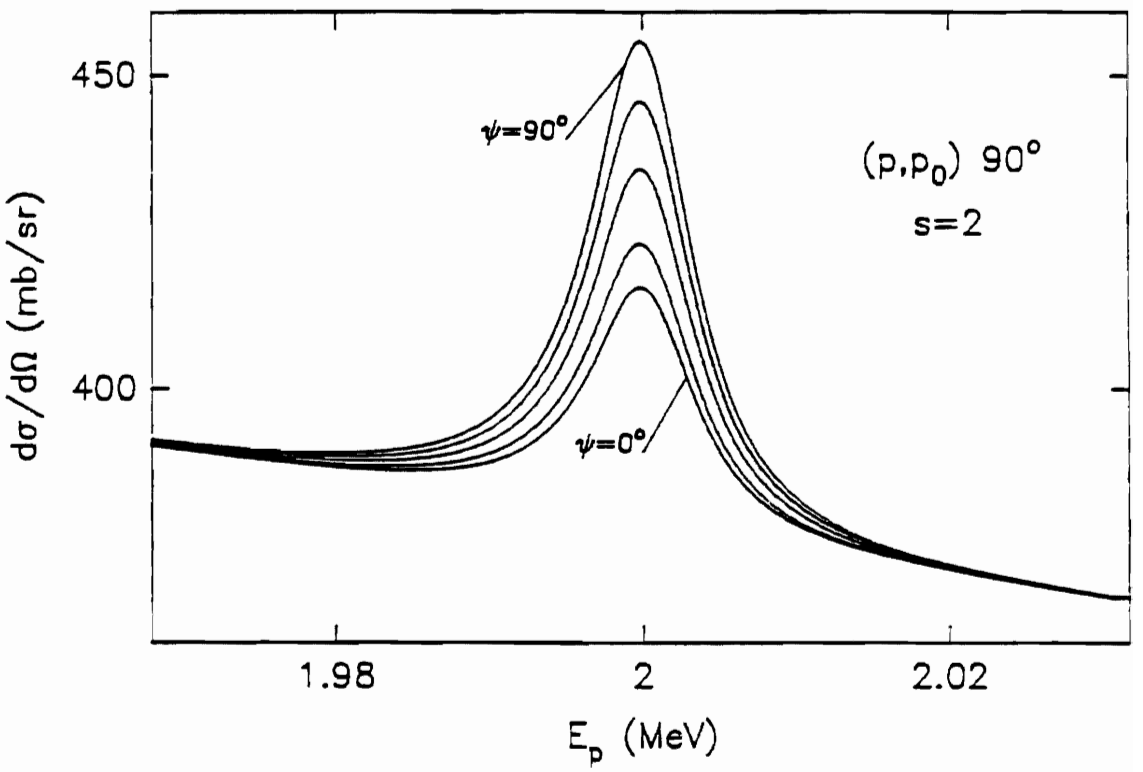

medium- sized resonances are superimposed on a much larger resonance (see the elastic scattering data from this experiment in the range 2.9 to 3.2 MeV). In this case the shapes of the smaller and intermediate-sized resonances are strongly distorted from their isolated shapes; the angular distributions for any reaction products for these resonances are often also strongly affected. Examples of the distortion of the single-level shape of a smaller resonance by a larger resonance are presented in figures 4.11 through 4.14. In figure 4.11 the elastic scattering differential cross section at $\theta = 165^{o}$ is shown, with two resonances present. In this plot the resonances have identical sets of quantum numbers, and one width is much larger than the other. The smaller resonance is shown in a number of positions with respect to the larger. The distortion of the smaller resonance is striking; its shape when the two resonances are close together is seen to be completely different from the isolated shape, and the apparent width of the smaller resonance is strongly reduced by the presence of the larger one. In figure 4.12 are shown the same two resonances at $\theta = 90^{o}$. It is evident from this plot that when the smaller resonance is approximately within the FWHM of the larger, the shape is inverted from the isolated shape. This is important to note since the resonance shape at $\theta = 90^{o}$ is usually an unambiguous indicator of the parity of the resonance (see figure 4.2).

Figures 4.13 and 4.14 are plots at $\theta = 165^{o}$ and $\theta = 90^{o}$ of the differential cross section for resonances with unlike quantum numbers and very different widths. The effect is quite different from that in the previous example; while the shape of the smaller resonance is distorted (see figure 4.13), its vertical excursion is smallest when it occurs at a lower energy than the larger one, and its vertical excursion is largest at a higher energy than that of the larger one. While this particular effect probably depends in detail on the specific quantum numbers of the two resonances, it is markedly different from the previous case. As may be seen in figure 4.14, the basic shape of the 90^{o} cross section is not changed by the presence of the larger resonance.

When there is clearly multilevel interference occurring the only recourse is to make logical guesses based on experience with isolated resonances and then to vary the available parameters in the hope of finding

Figure 4.11 Two level interference for resonances with the same spin and parity but quite different widths. In plot 1 the differential cross section shape is shown at 165^{o} for a 3^{-} p-wave resonance with s = 2 and a total width of 1 keV. In the following plots is shown the distortion of this shape due to the presence of a 35 keV resonance with the same quantum numbers. The spacings between the resonances are 80, 50, 20, 10, 5, 0, 5, 10, 20, 50, and 80 keV for plots 2 through 12. The vertical axis range is 25 to 100 mb/sr in each plot, and the horizontal axis range is 2.9 to 3.1 MeV in each plot.

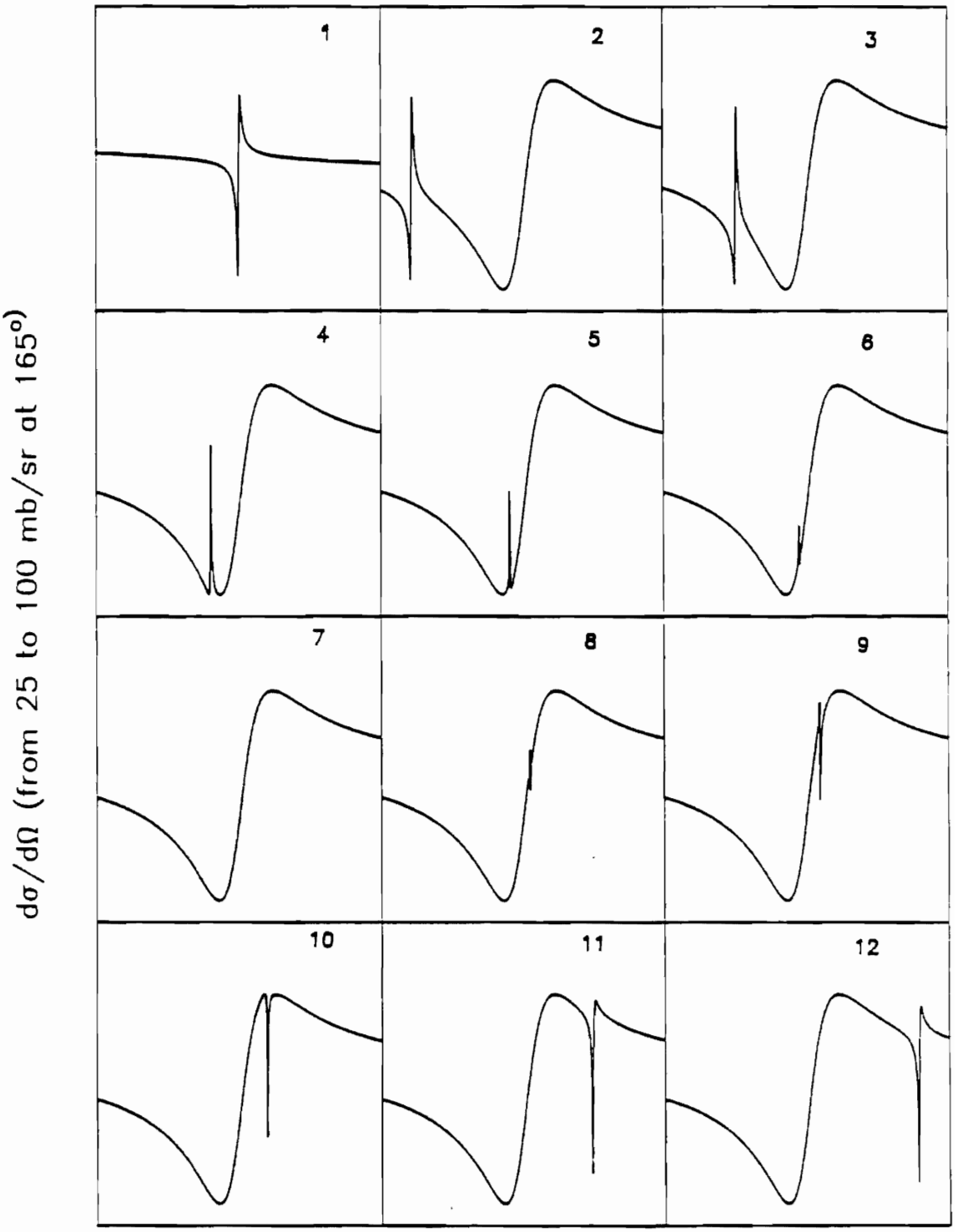
1
2
3
4
5
6
7
8
9
10
11
12
dσ/dΩ (from 25 to 100 mb/sr at 165°)
E_p (from 2.9 to 3.1 MeV)

Figure 4.12 Two level interference for levels with the same spin and parity but quite different widths. In plot 1 the differential cross section shape is shown at 90^{o} for a 3^{-} p-wave resonance with s = 2 and a total width of 1 keV. In the following plots is shown the distortion of this shape due to the presence of a 35 keV resonance with the same quantum numbers. The spacings between the resonances are 80, 50, 20, 10, 5, 0, 5, 10, 20, 50, and 80 keV for plots 2 through 12. The vertical axis range is 170 to 240 mb/sr in each plot, and the horizontal axis range is 2.9 to 3.1 MeV in each plot.

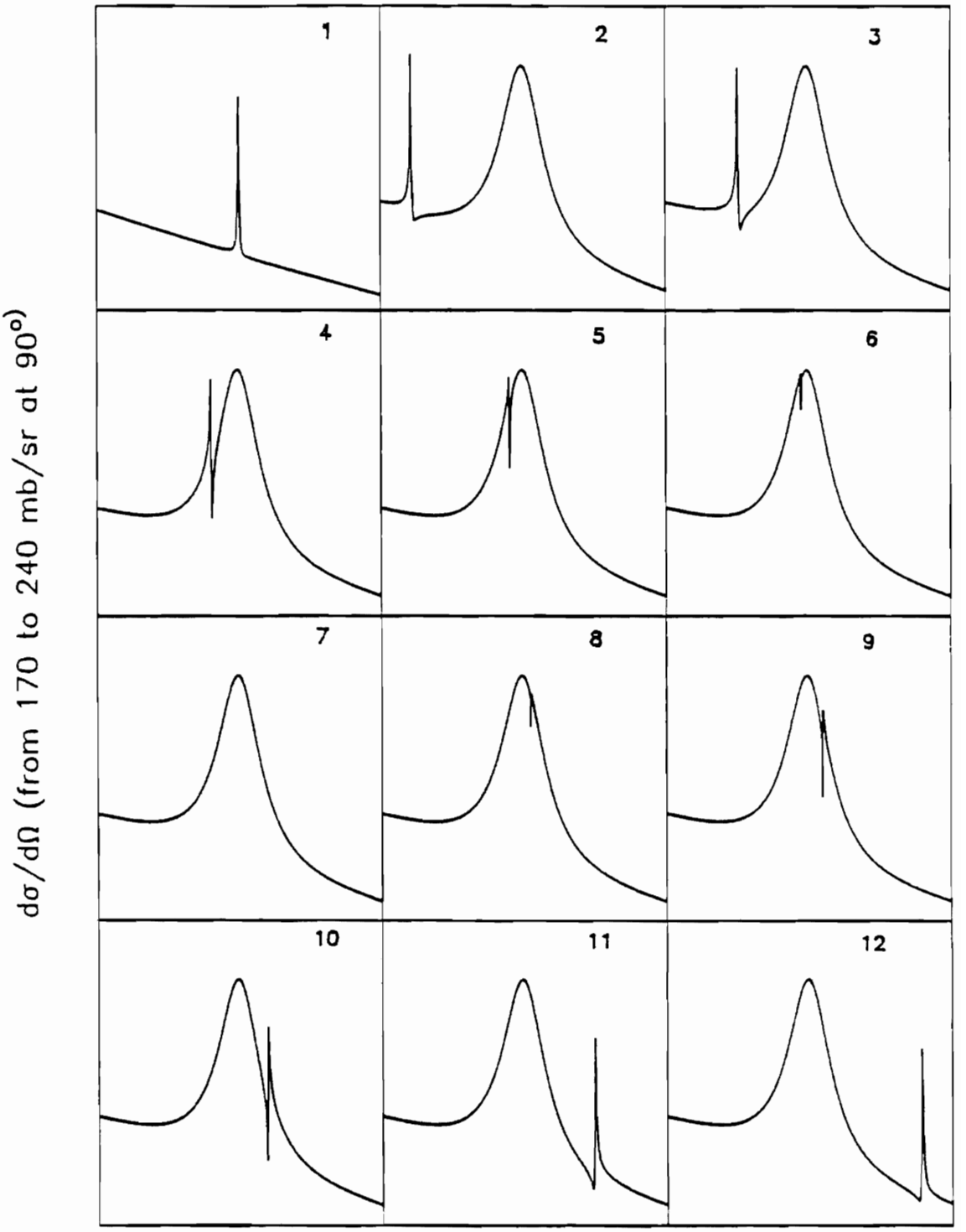
1
2
3
4
5
6
7
8
9
10
11
12
dσ/dΩ (from 170 to 240 mb/sr at 90°)
E_p (from 2.9 to 3.1 MeV)

Figure 4.13 Two level interference for levels with different spin and parity and quite different widths. In plot 1the differential cross section shape is shown at 165^{o} for a 2^{+} s-wave resonance with s = 2 and a total width of 1 keV. In the following plots is shown the distortion of this shape due to the presence of a 35 keV p-wave resonance with $J^{\pi} = 3^{-}$ and s = 2. The spacings between the resonances are 80, 50, 20, 10, 5, 0, 5, 10, 20, 50, and 80 keV for plots 2 through 12. The vertical axis range is 20 to 200 mb/sr in each plot, and the horizontal axis range is 2.9 to 3.1 MeV in each plot.

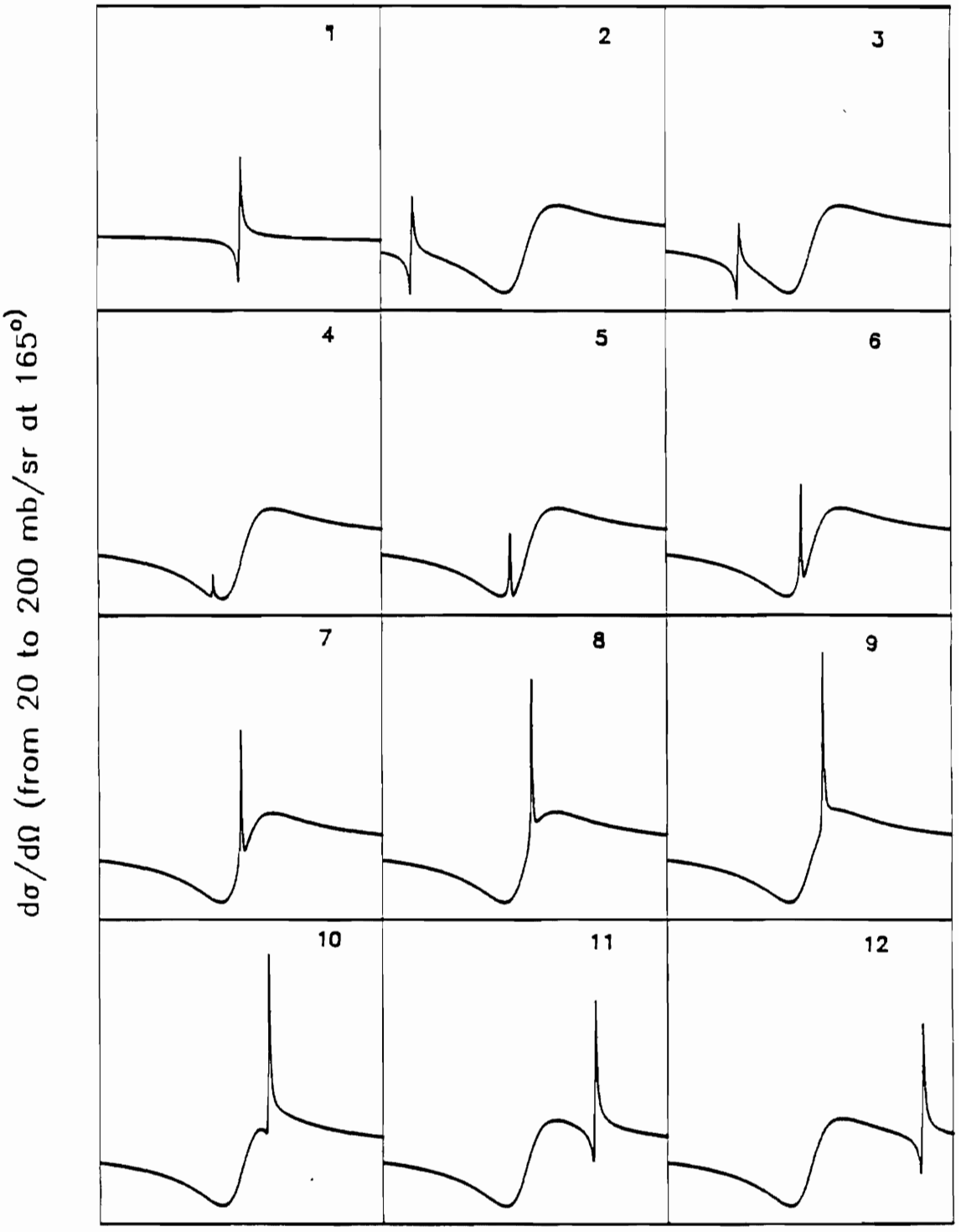
1
2
3
4
5
6
7
8
9
10
11
12
dσ/dΩ (from 20 to 200 mb/sr at 165°)
E_p (from 2.9 to 3.1 MeV)

Figure 4.14 Two level interference for levels with different spin and parity and quite different widths. In plot 1 the differential cross section shape is shown at 90^{o} for a 2^{+} s-wave resonance with s = 2 and a total width of 1 keV. In the following plots is shown the distortion of this shape due to the presence of a 35 keV p-wave resonance with $J^{\pi} = 3^{-}$ and s = 2. The spacings between the resonances are 80, 50, 20, 10, 5, 0, 5, 10, 20, 50, and 80 keV for plots 2 through 12. The vertical axis range is 90 to 250 mb/sr in each plot, and the horizontal axis range is 2.9 to 3.1 MeV in each plot.

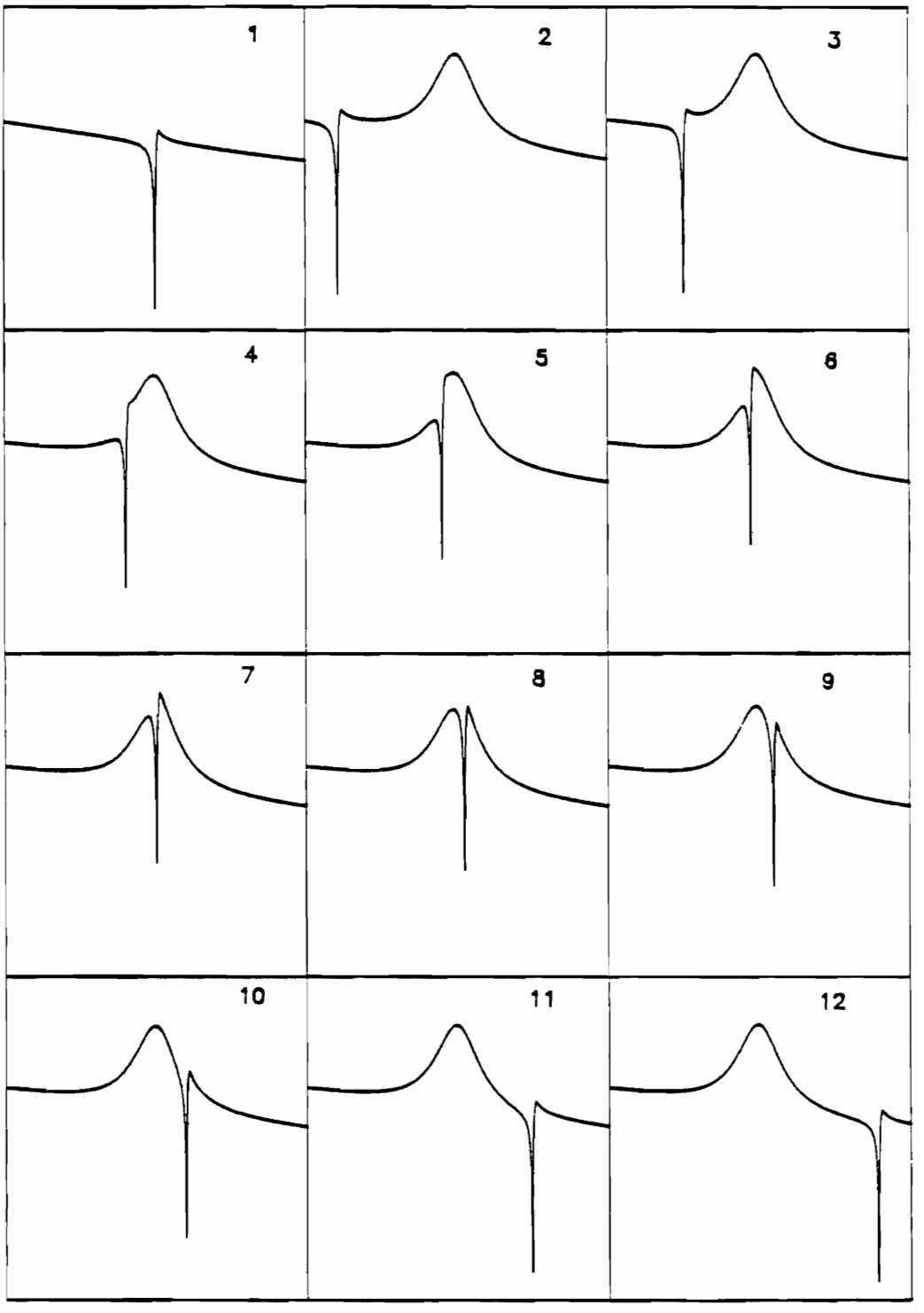
1
2
3
4
5
6
7
8
9
10
11
12
dσ/dΩ (from 90 to 250 mb/sr at 90°)
E_p (from 2.9 to 3.1 MeV)

a good fit. The interference tends to successfully limit the number of different parameter sets which give acceptable fits to few or one when such sets can be found. In cases where many resonances are involved it may be worthwhile to make a catalog of plots similar to figures 4.11 through 4.14 in order to obtain a detailed fit to a complicated region.

Two level interference can be seen in reaction channels as well. In figure 4.15 the resonance shapes for the (p,α_0) channel at five angles for a small resonance are plotted. In one column of plots the small resonance is isolated, in the other a large resonance of the same spin and parity is located nearby in energy. While the angular distribution of the smaller resonance is unchanged, the peak location is shifted and the apparent width is decreased. In figure 4.16 the same figure is plotted in the case where the large resonance also has an alpha decay width. The shapes of both alpha peaks are distorted, the smaller alpha peak energies are shifted more than in the previous plots, the apparent widths of the small alpha peaks are smaller, but the angular distribution is unchanged.

Another effect which occurs when a resonance with one open channel distorts the shape of a nearby resonance in a different channel. A typical example is a large resonance which has an alpha decay width with a smaller resonance superimposed. Even if the smaller resonance has no alpha width the shape of the larger resonance in the alpha channel can be affected. Similar results are discussed at length by Fang (1987).

A third effect is the interference of two resonances of similar width which have nearly the same resonance energies. In this case it is often extremely difficult to achieve an acceptable fit unless other reaction channels are also open. When this is the case the locations of the resonance energies (except for energy separations just below the experimental resolution) are usually apparent, and if the (p,α_0) channel is open, the possible J values for the resonances are strongly restricted.

At some point the number of overlapping levels becomes too great to analyze. When this occurs there are several productive compromises which may be adopted. First the largest resonances often may still be fitted, and this is important because the cumulative long-range effects are greatest for these strong resonances. Second, if the (p,α_0) channel is open for some of

Figure 4.15 Two level interference effects in reaction channels. The top plot in the column on the left shows the 165^{o} elastic scattering differential cross section for an isolated 3^{-} p-wave resonance with s = 2. The total width is 1 keV, with half of this in the elastic channel and half in the (p,α_o) channel. Below this plot is shown the differential cross sections at five different angles for the (p,α_o) channel. The plots in the column on the right show the effect of a large resonance on the (p,α_o) differential cross sections. The angular distribution of the resonance peaks is the same, but the peaks are all shifted to the right by 100 eV and the area under each peak is reduced. In these plots the large resonance has no alpha width, the two resonances are separated by 10 keV, the larger resonance has a total width of 35 keV and has the same quantum numbers as the small resonance. The elastic scattering plots have a vertical range of 25 to 90 mb/sr and the (p,α_o) plots have a vertical range of 0 to 25 mb/sr.

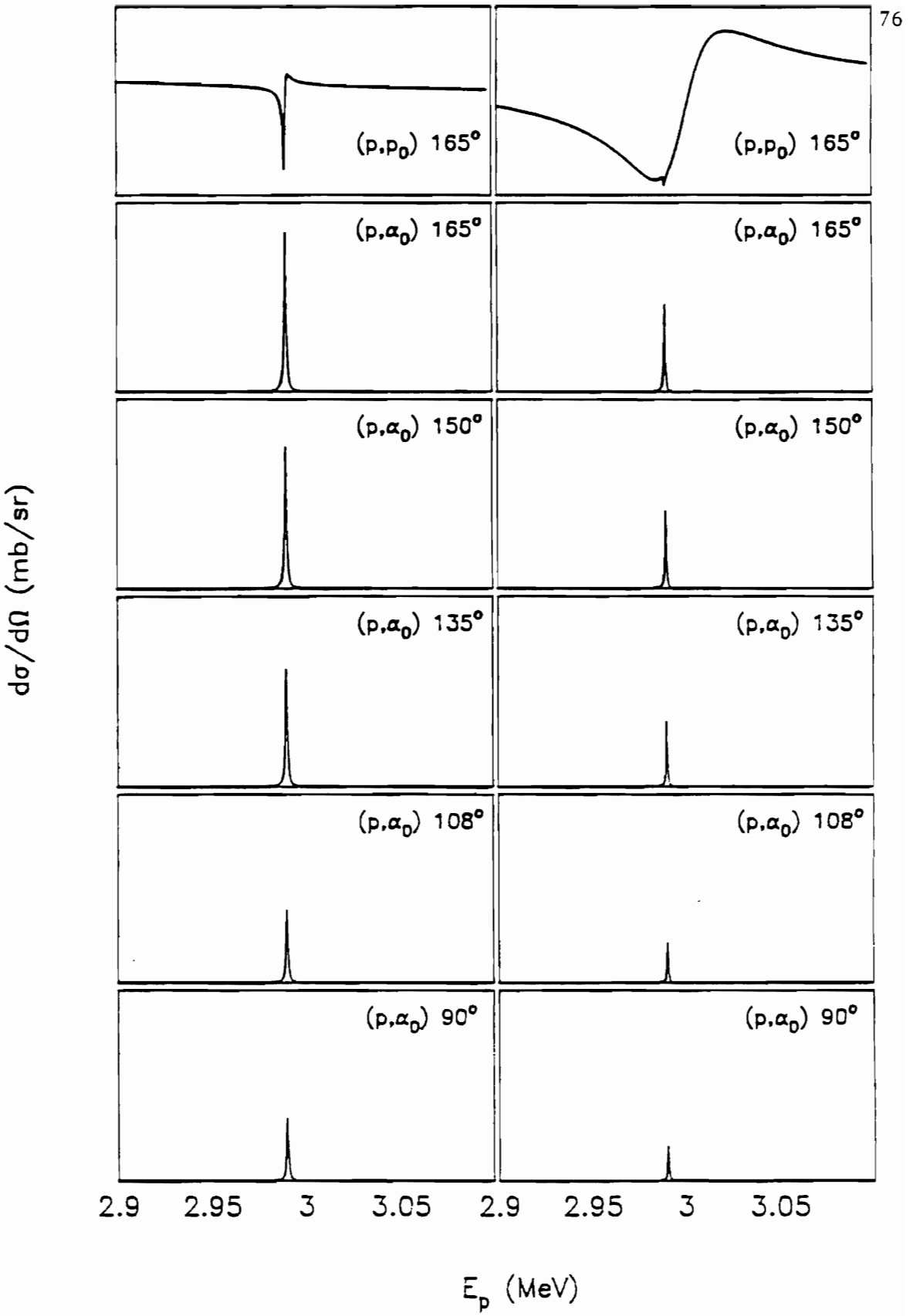
(p,p0) 165°
(p,p0) 165°
(p,α0) 165°
(p,α0) 165°
(p,α0) 150°
(p,α0) 150°
(p,α0) 135°
(p,α0) 135°
(p,α0) 108°
(p,α0) 108°
(p,α0) 90°
(p,α0) 90°
dσ/dΩ (mb/sr)
2.9
2.95
3
3.05
2.9
2.95
3
3.05
Ep (MeV)

Figure 4.16 Two level interference effects in reaction channels. The top plot in the column on the left shows the 165^{o} elastic scattering differential cross section for an isolated 3^{-} p-wave resonance with s = 2. The total width is 1 keV, with half of this in the elastic channel and half in the (p,α_o) channel. Below this plot is shown the differential cross sections at five different angles for the (p,α_o) channel. The plots in the column on the right show the effect of a large resonance on the (p,α_o) differential cross sections. The angular distribution of the resonance peaks is the same, but the peaks are all shifted to the right by 300 eV, the area under each peak is reduced and both peaks are asymmetrically distorted. In these plots the large resonance has an alpha width of 1 keV, the two resonances are separated by 10 keV, the larger resonance has a total width of 35 keV and has the same quantum numbers as the small resonance. The elastic scattering plots have a vertical range of 25 to 90 mb/sr and the (p,α_o) plots have a vertical range of 0 to 25 mb/sr.

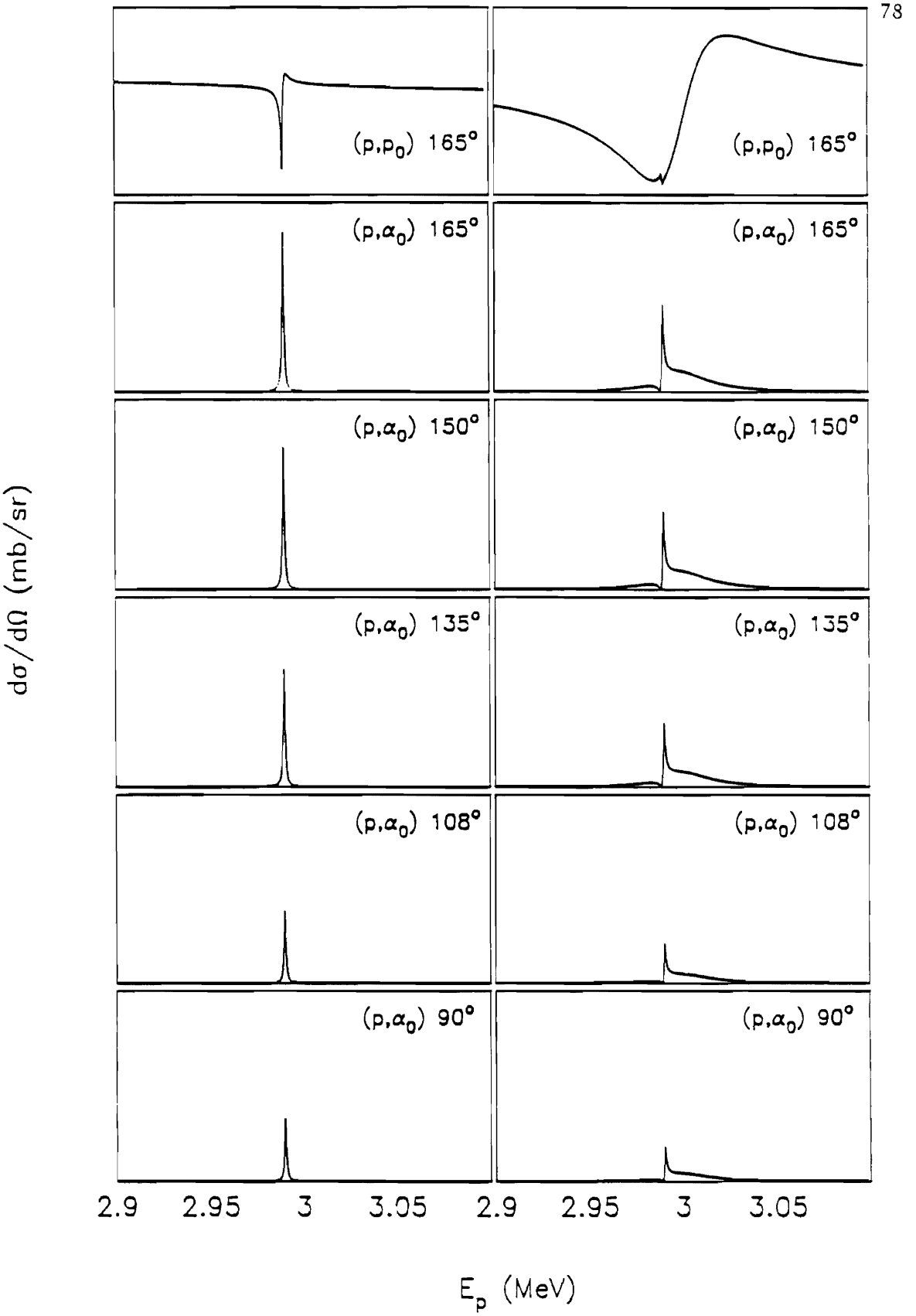
(p,p0) 165°
(p,p0) 165°
(p,α0) 165°
(p,α0) 165°
(p,α0) 150°
(p,α0) 150°
(p,α0) 135°
(p,α0) 135°
(p,α0) 108°
(p,α0) 108°
(p,α0) 90°
(p,α0) 90°
dσ/dΩ (mb/sr)
2.9
2.95
3
3.05
2.9
2.95
3
3.05
Ep (MeV)

the smaller resonances, it may still be possible to make a definitive choice between two possible J values if the background resonances are reasonably well-fitted. For resonances which have small elastic widths but large reaction channel strength it is often possible to assign a resonance energy, which can help to clarify the number of resonances in a given region. Even if the reliability of the spin and parity assignments is reduced, the general behavior of the reduced widths will still be obtained.

CHAPTER V

DATA, FIT, AND RESONANCE PARAMETERS

In this chapter the data and fit are presented and discussed.

A. Data and Fit

The data were measured at five scattering angles. The most useful channels for fitting purposes were the elastic and the (p,α_0) channels. Fitting was performed while checking all five angles for each resonance, and the angular distributions of reaction products were also checked when the channels were open.

In figures 5.1 and 5.2 the data and fit are shown for elastic scattering and the (p,α_0) channel. The plots are of differential cross sections at θ = 165°, and the energy range is 1.0 MeV for each plot. An example of the data and fit at all five angles for elastic scattering is shown in figure 5.3. Typically the quality of the data is lowest at 90° and 108°, and improves dramatically at the back angles of 135°, 150° and 165°. The parity of a resonance can nearly always be determined by the 90° differential cross section, while the values of J, s and ℓ are best determined by the 165° differential cross section.

In figure 5.4 a example of the data and fit is shown for the (p,α_0) reaction at five angles, along with the elastic scattering at 165°.

The elastic scattering and (p,α_0) differential cross section data and fit at 165° are presented in figures 5.5 through 5.9. The energy range shown is from E_p = 1.2 to 3.2 MeV in 400 keV sections. In this range the fit is relatively good and the fitting parameters are the most reliable. No resonances were observed below 1.2 MeV. Figure 5.10 displays the data in four reaction channels from E_p = 3.2 to 4.0 MeV at 165°. Tentative fitting parameters were established for these resonances; these parameters are presented in table 5.2.

Figure 5.1 Differential cross sections for the $^{35}Cl(p,p_0)^{35}Cl$ and $^{35}Cl(p,\alpha_0)^{32}S$ reactions at 165° from 1.2 to 2.2 MeV. The solid curve is an R-matrix fit.

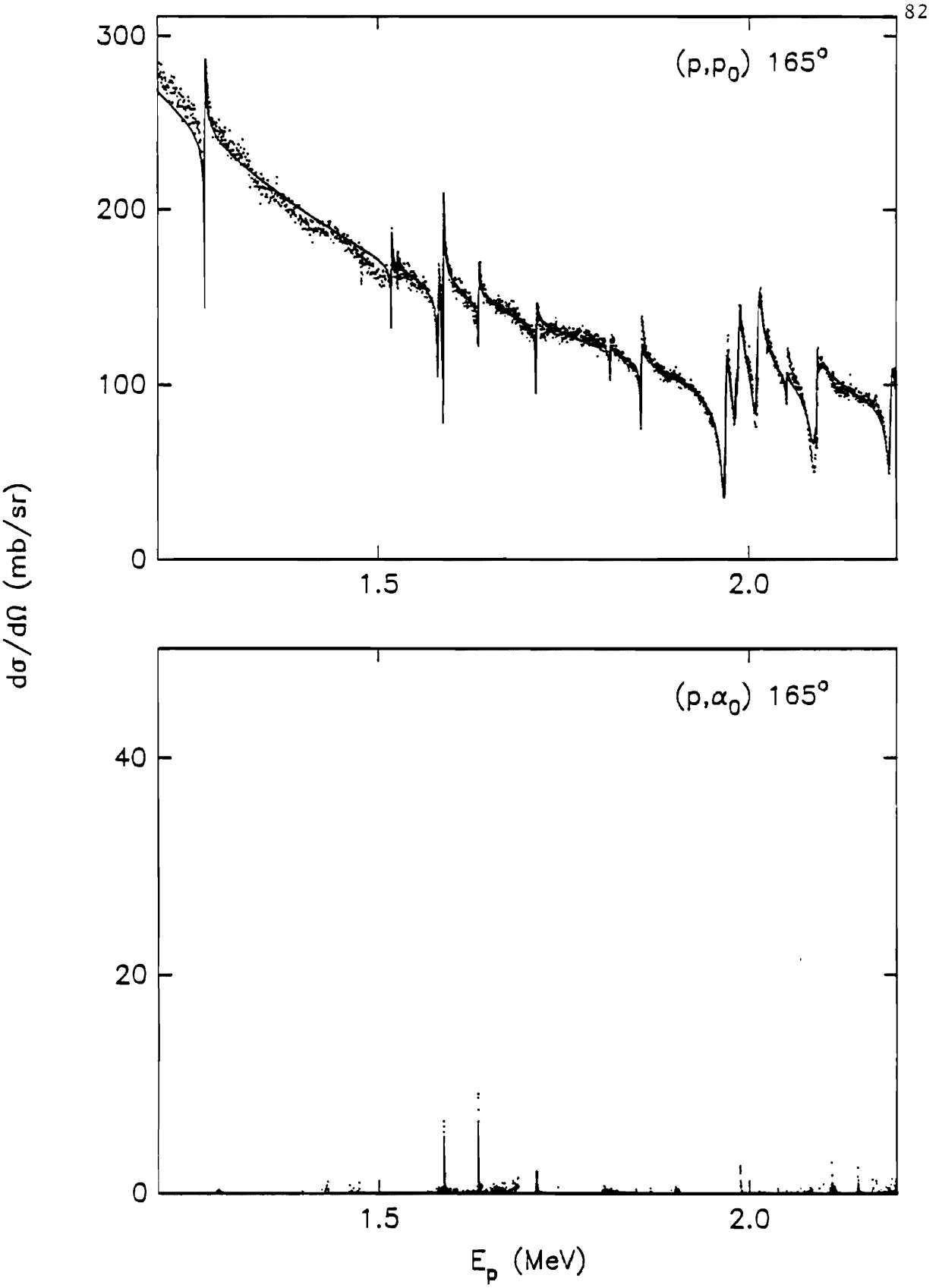
(p,p0) 165°
300
200
100
0
1.5
2.0
(p,α0) 165°
40
20
0
1.5
2.0
dσ/dΩ (mb/sr)
Ep (MeV)

Figure 5.2 Differential cross sections for the $^{35}Cl(p,p_0)^{35}Cl$ and $^{35}Cl(p,\alpha_0)^{32}S$ reactions at 165° from 2.2 to 3.2 MeV. The solid curve is an R-matrix fit.

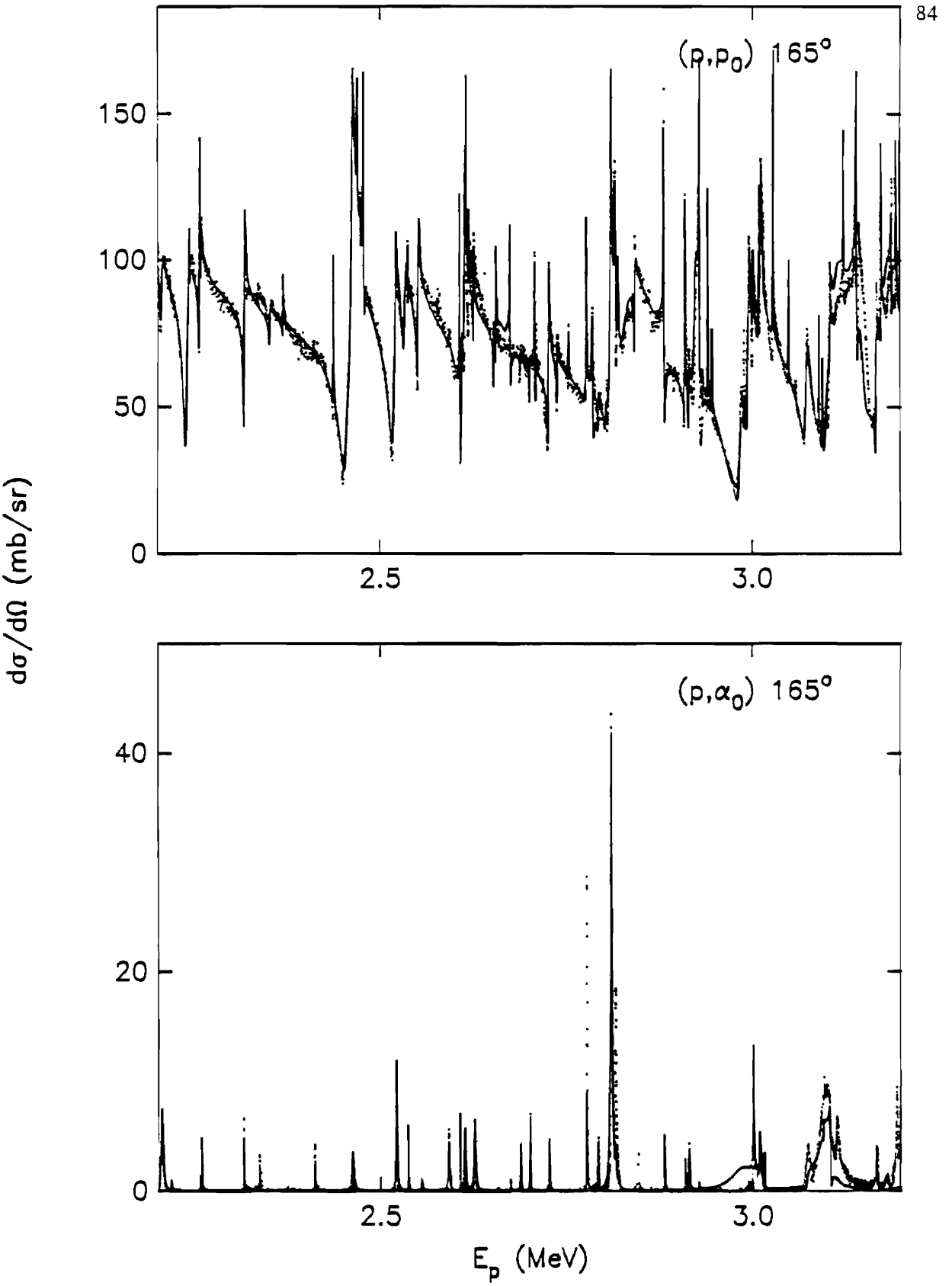
(p,p0) 165°
150
100
50
0
2.5
3.0
(p,α0) 165°
40
20
0
2.5
3.0
dσ/dΩ (mb/sr)
Ep (MeV)

Figure 5.3 Differential cross sections for the $^{35}Cl(p,p_0)^{35}Cl$ reaction at θ = 165°, 150°, 135°, 108°, and 90° from E_p = 2.4 to 2.6 MeV. The solid curve is an R-matrix fit.

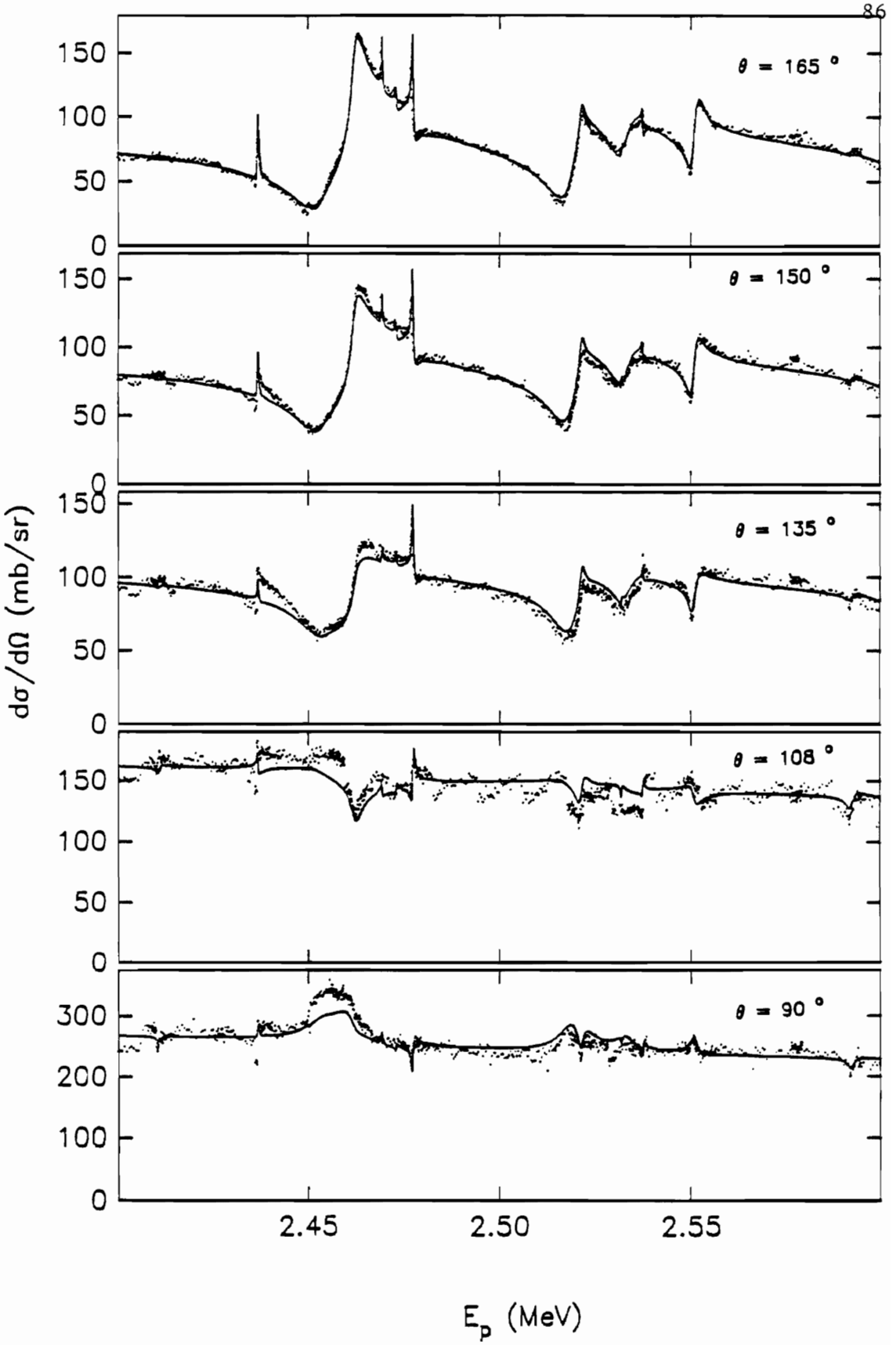
θ = 165 °
θ = 150 °
θ = 135 °
θ = 108 °
θ = 90 °
dσ/dΩ (mb/sr)
E_p (MeV)
2.45
2.50
2.55

Figure 5.4 Differential cross sections for the $^{35}Cl(p,p_0)^{35}Cl$ at 165° and for the $^{35}Cl(p,\alpha_0)^{32}S$ reaction at θ = 165°, 150°, 135°, 108°, and 90° from E_p = 2.2 to 2.3 MeV. The solid curve is an R-matrix fit.

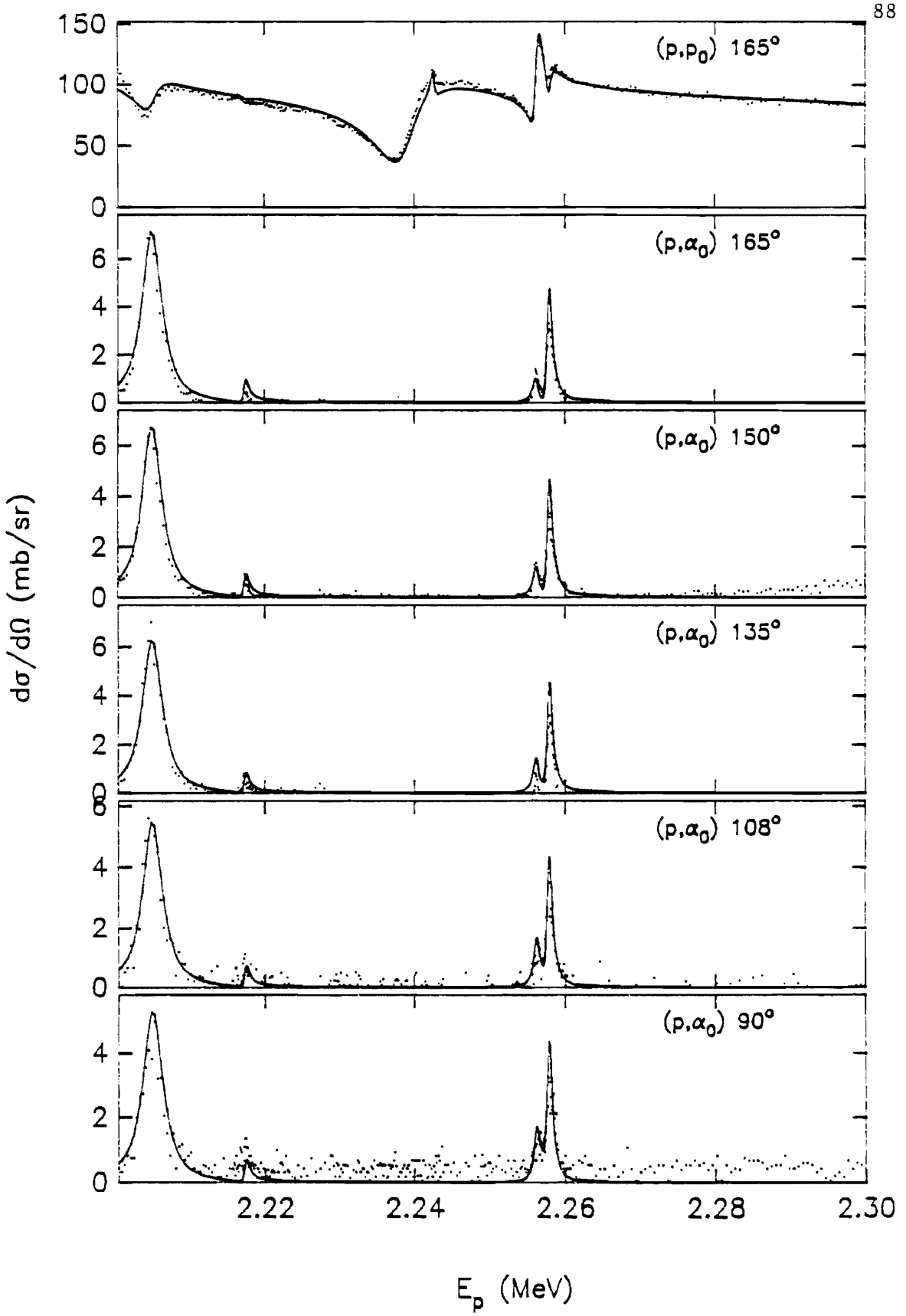
(p,p0) 165°
(p,α0) 165°
(p,α0) 150°
(p,α0) 135°
(p,α0) 108°
(p,α0) 90°
dσ/dΩ (mb/sr)
Ep (MeV)
2.22
2.24
2.26
2.28
2.30

Figure 5.5 Differential cross sections for the $^{35}Cl(p,p_0)^{35}Cl$ and $^{35}Cl(p,\alpha_0)^{32}S$ reactions at 165° from 1.2 to 1.6 MeV. The solid curve is an R-matrix fit.

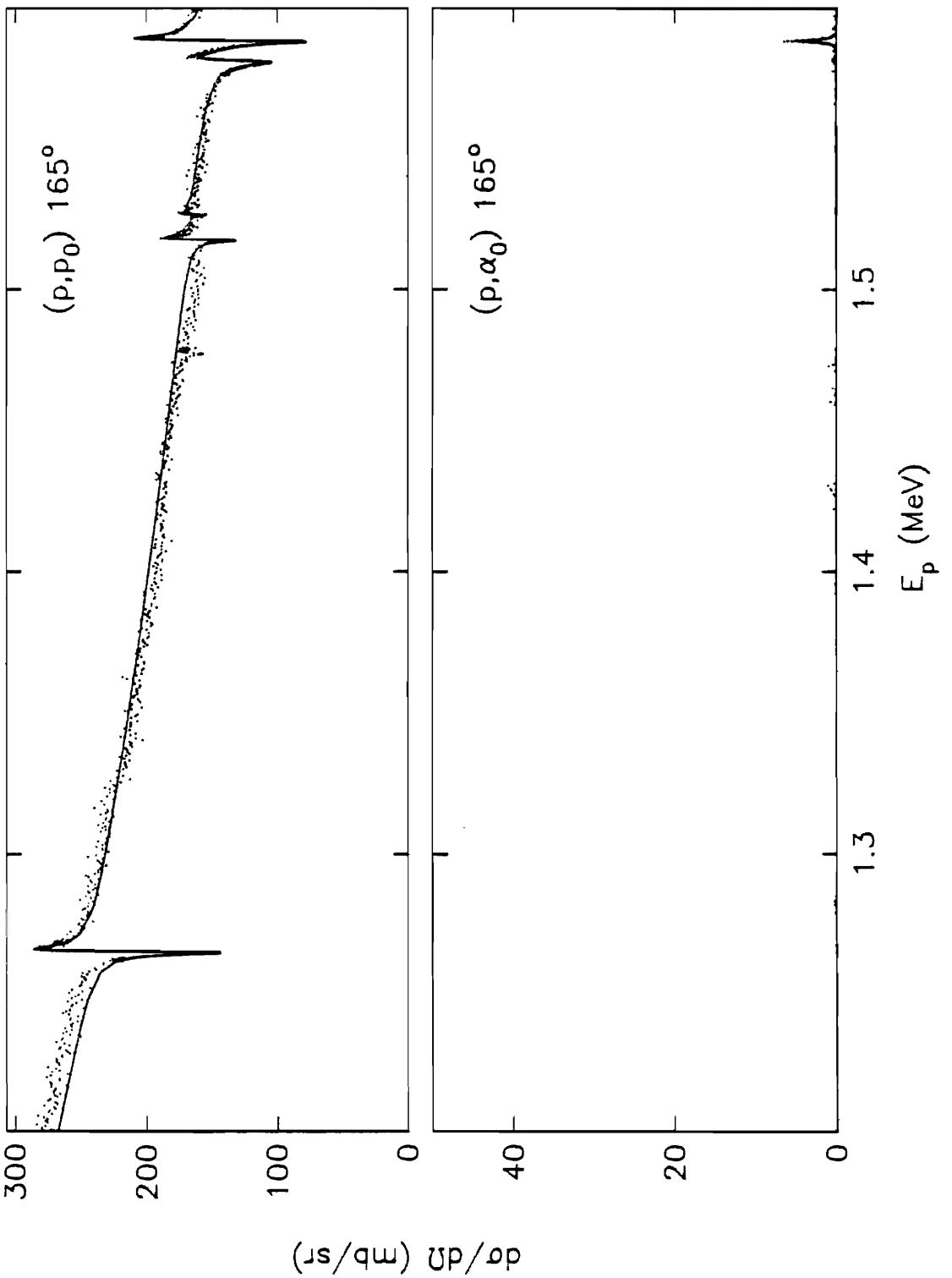
(p,p0) 165°
(p,α0) 165°
dσ/dΩ (mb/sr)
300
200
100
0
40
20
0
1.3
1.4
1.5
Ep (MeV)

Figure 5.6 Differential cross sections for the $^{35}Cl(p,p_0)^{35}Cl$ and $^{35}Cl(p,\alpha_0)^{32}S$ reactions at 165° from 1.6 to 2.0 MeV. The solid curve is an R-matrix fit.

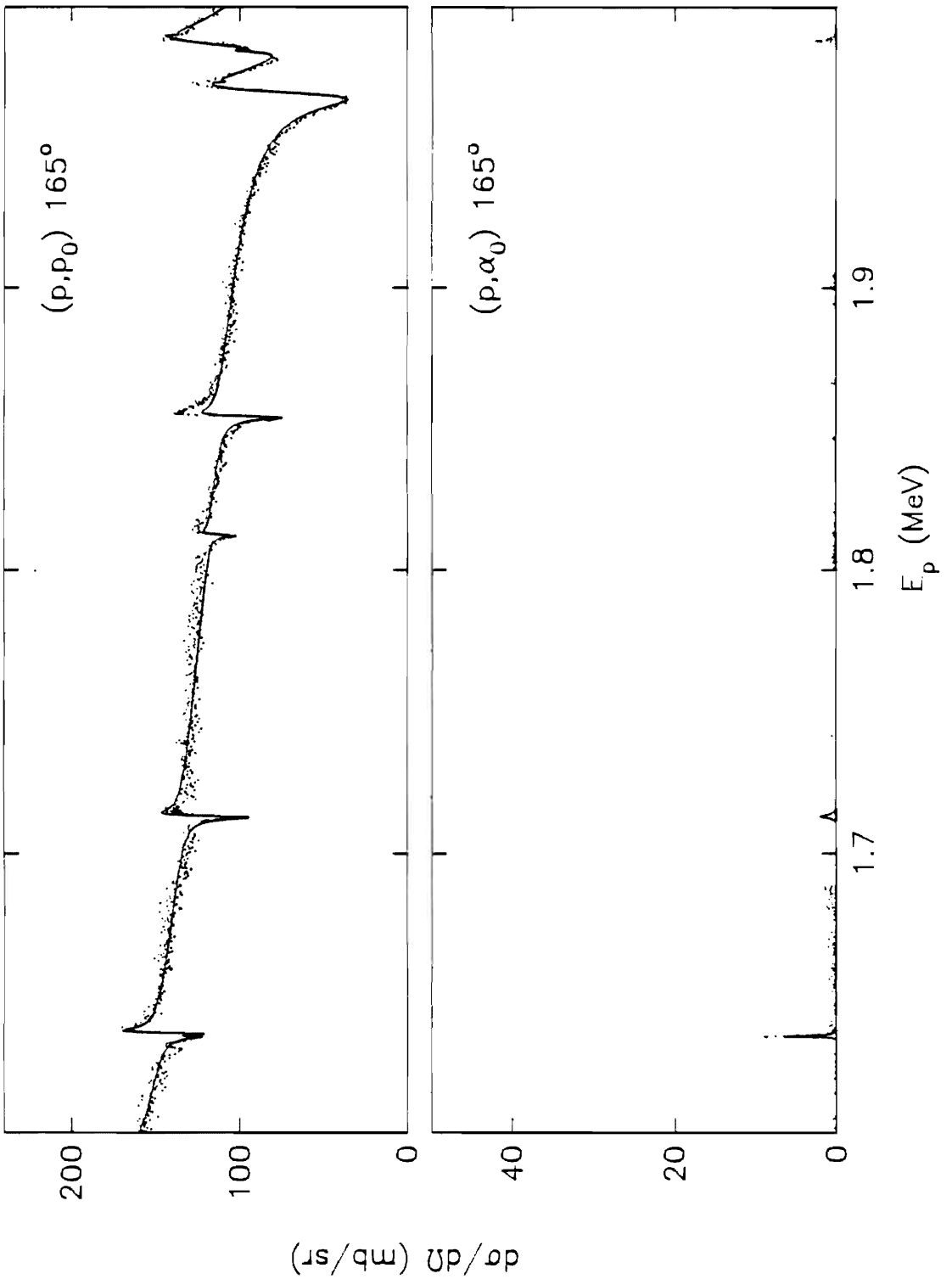
(p,p0) 165°
(p,α0) 165°
200
100
0
40
20
0
1.7
1.8
1.9
Ep (MeV)
dσ/dΩ (mb/sr)

Figure 5.7 Differential cross sections for the $^{35}Cl(p,p_0)^{35}Cl$ and $^{35}Cl(p,\alpha_0)^{32}S$ reactions at 165° from 2.0 to 2.4 MeV. The solid curve is an R-matrix fit.

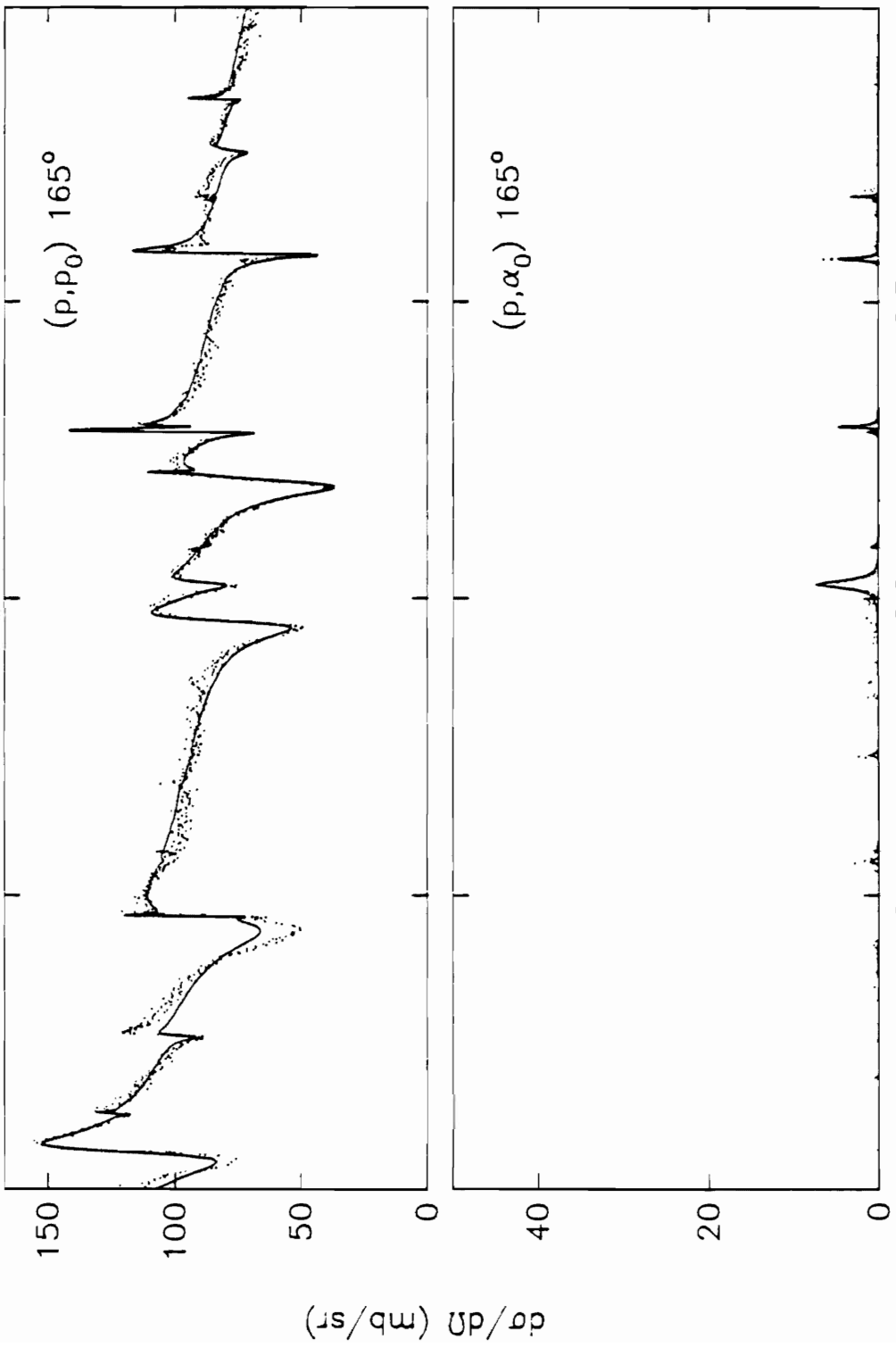
(p,p0) 165°
(p,α0) 165°
dσ/dΩ (mb/sr)
150
100
50
0
40
20
0
2.1
2.2
2.3
Ep (MeV)

Figure 5.8 Differential cross sections for the $^{35}Cl(p,p_0)^{35}Cl$ and $^{35}Cl(p,\alpha_0)^{32}S$ reactions at 165° from 2.4 to 2.8 MeV. The solid curve is an R-matrix fit.

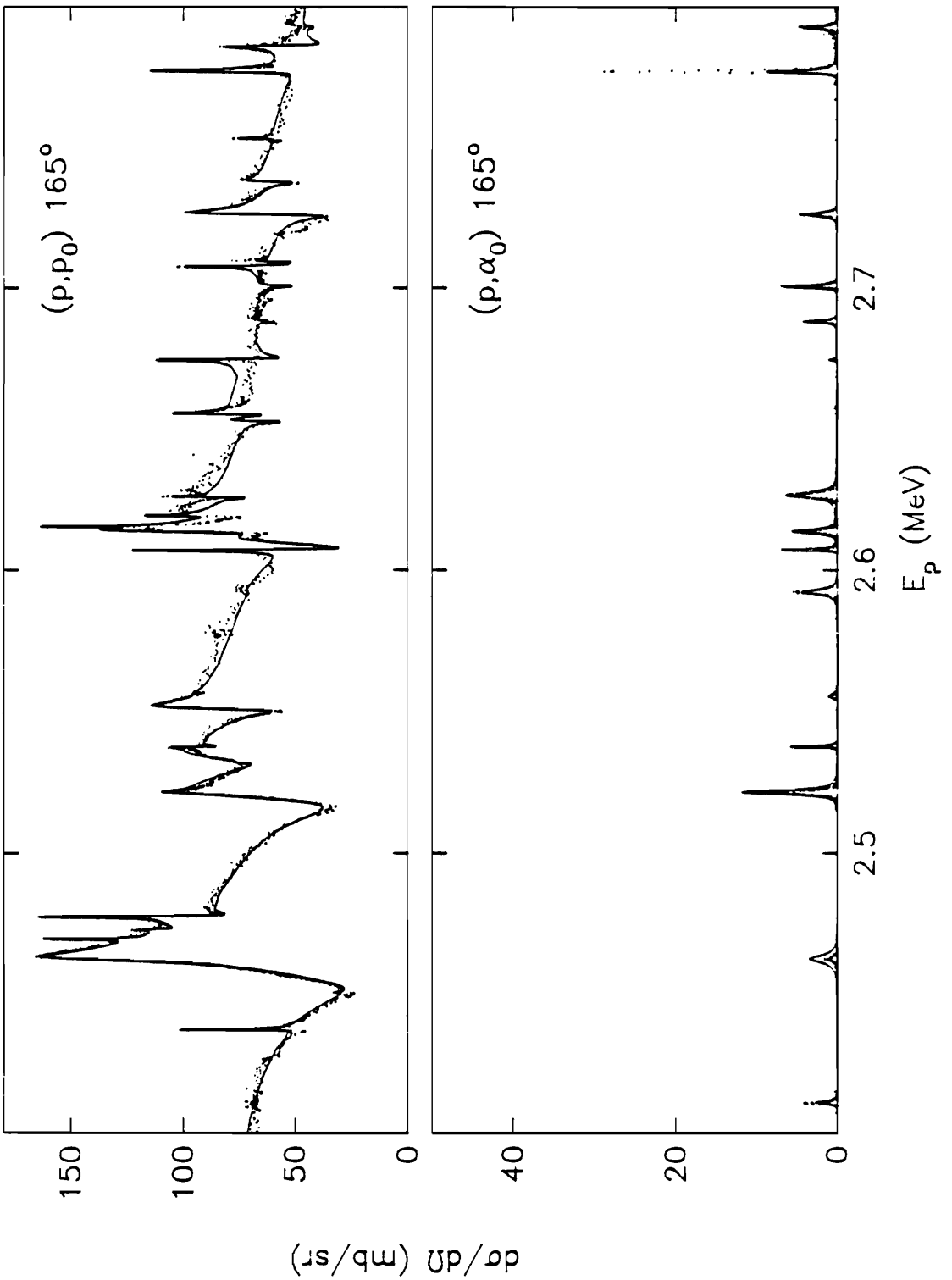
(p,p0) 165°
(p,α0) 165°
dσ/dΩ (mb/sr)
150
100
50
0
40
20
0
2.5
2.6
2.7
Ep (MeV)

Figure 5.9 Differential cross sections for the $^{35}Cl(p,p_0)^{35}Cl$ and $^{35}Cl(p,\alpha_0)^{32}S$ reactions at 165° from 2.8 to 3.2 MeV. The solid curve is an R-matrix fit.

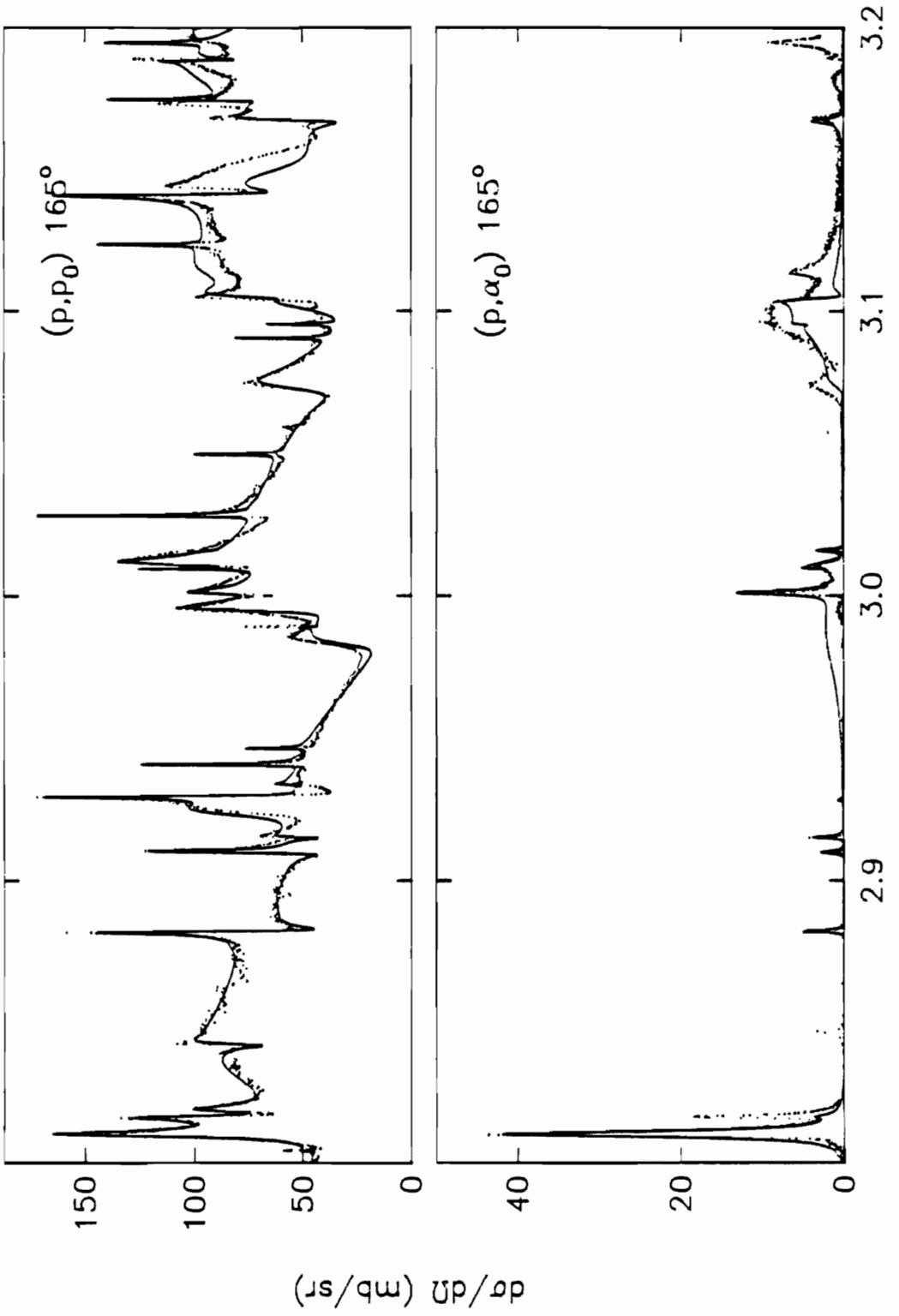
(p,p0) 165°
(p,α0) 165°
dσ/dΩ (mb/sr)
E_p (MeV)
150
100
50
0
40
20
0
2.9
3.0
3.1
3.2

Figure 5.10 Differential cross sections for the $^{35}Cl(p,p_0)^{35}Cl$, $^{35}Cl(p,\alpha_0)^{32}S$, $^{35}Cl(p,p_1)^{35}Cl$, and $^{35}Cl(p,p_2)^{35}Cl$ reactions at $\theta = 165^o$ from 3.2 to 4.0 MeV.

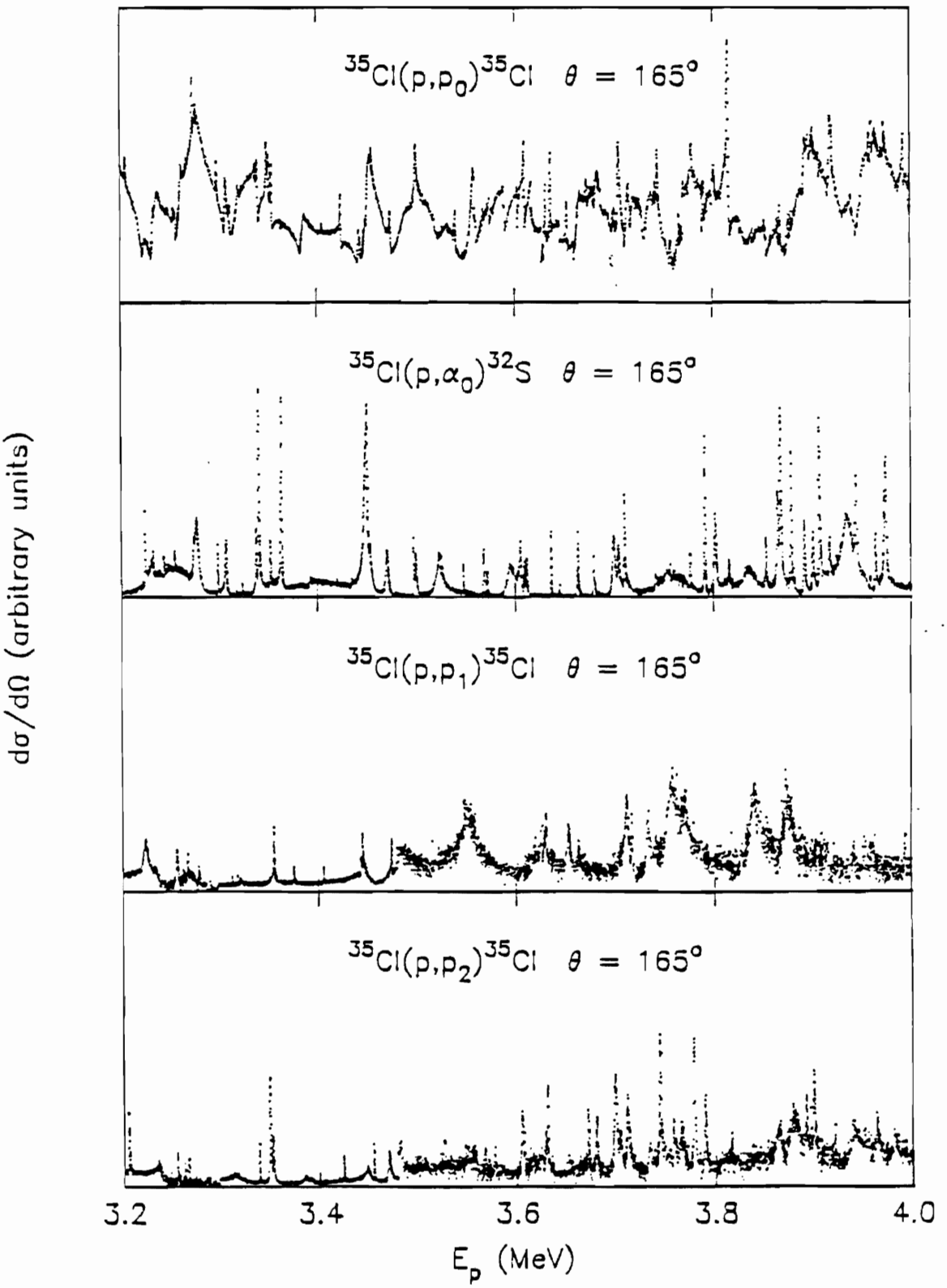
$^{35}Cl(p,p_0)^{35}Cl$ θ = 165°
$^{35}Cl(p,\alpha_0)^{32}S$ θ = 165°
$^{35}Cl(p,p_1)^{35}Cl$ θ = 165°
$^{35}Cl(p,p_2)^{35}Cl$ θ = 165°
dσ/dΩ (arbitrary units)
3.2
3.4
3.6
3.8
4.0
E_p (MeV)

B. Resonance Parameters

The resonance parameters which produced the best fits are given in Table 5.1. The reliability of the parameters vary. Isolated widths are probably reliable to 10 - 20%, and in many cases to 5%, if there are no significant ambiguities about orbital and channel spin mixing or J-assignment. For isolated elastic widths smaller than the experimental resolution the uncertainty is greater. However, if the same resonance occurs in another reaction channel the total width estimate is much better. The spin and parity assignments were unambiguous in nearly all cases. They are particularly reliable when the (p,α_0) channel is open, since for a given parity the allowed J values change in increments of 2. In general, parameters for resonances where the observed effect in the elastic channel was small are less reliable than those which are clearly visible. There were a number of resonances which were observed in the reaction channels but not in the elastic channel. Although these resonances were difficult to fit, often reasonable assignments could be made.

At higher energies the interference effects contribute to the reliability of the fit whenever the fit is good. This is because the parameters become less independent of each other and therefore the number of different equivalent fits decreases. Unfortunately these effects are difficult to quantify.

One other distinct category is that of large resonances. In this experiment there were nearly twenty resonances of width greater than 10 keV total width. For these the width assignments can be estimated to better than 20%. The spin and parity assignments are reasonably reliable, although many of the large resonances show strong interference effects with each other and with the sum of the smaller ones.

The relative signs of the reduced width amplitudes could be determined in a few cases where level-level interference ocurred. If the relative signs are not determined, the signs have arbitrarily been assigned positive.

The uncertainty in the orbital and channel spin mixing ratios varies from resonance to resonance. These values are most reliable in regions where there is level-level interference and the elastic scattering and (p,α_0) data are

both well fit. A detailed study of any given resonance would yield more precise values with smaller uncertainties than those given here. When the channel spin was not determined, it was arbitrarily assigned a value of 2.

Brooks Phd Thesis 1988

$R_0 = ?$

Table 5.1

Resonance Parameters for $^{35}Cl(p,x)$

		(p,p_0)				(p,α_0)				(p,p_1)				(p,p_2)			
E_p (MeV)	J^π	ℓ	s	Γ (keV)	γ^2 (keV)	ℓ	s	Γ (keV)	γ^2 (keV)	ℓ	s	Γ (keV)	γ^2 (keV)	ℓ	s	Γ (keV)	γ^2 (keV)
1.2652	2^-	1	1	0.7	160												
		1	2	0.2	46												
1.5177	1^-	1	1	0.55	37												
		1	2	0.05	3.4												
1.5265	1^-	1	1	0.1	6.5												
1.5810	1^-	1	2	1.4	73												
1.5882	3^-	1	2	0.8	41	3	0	0.025	37								
1.6347	2^+	0	2	0.05	0.77	2	0	0.2	78								
1.6360	1^-	1	1	0.85	36												
1.7130	1^-	1	2	1.0	32	1	0	0.05	6.7								
1.8124	0^-	1	1	1.0	23												
1.8544	1^-	1	2	1.2	25												
1.9690	3^-	1	1	5.5	81												
1.9730	0^+	2	2	0.15	13												

Table 5.1 (continued)

E_p (MeV)	J^π	(p,p_0) ℓ	s	Γ (keV)	γ^2 (keV)	(p,α_0) ℓ	s	Γ (keV)	γ^2 (keV)	(p,p_1) ℓ	s	Γ (keV)	γ^2 (keV)	(p,p_2) ℓ	s	Γ (keV)	γ^2 (keV)
1.9840	0^-	1	1	1.0	14												
1.9860	2^-	1	1	7.0	99												
1.9895	0^+	2	2	0.15	12												
2.0126	2^-	1	2	6.0	79												
		3	2	0.1	92												
2.0258	1^+	0	1	0.05	0.26												
2.0376	1^-	1	2	0.001	0.012	1	0	0.1	4.5								
2.0521	0^-	1	1	1.3	16												
2.0920	2^-	1	1	6.0	130												
2.0930	1^+	0	1	0.06	1.1												
2.1115	1^-	1	2	0.03	0.31	1	0	1.0	36								
2.1375	1^-	3	2	0.03	18												
2.1475	1^-	1	2	0.03	0.29	1	0	1.0	33								

Table 5.1 (continued)

E_p (MeV)	J^π	(p,p_0) ℓ	s	Γ (keV)	γ^2 (keV)	(p,α_0) ℓ	s	Γ (keV)	γ^2 (keV)	(p,p_1) ℓ	s	Γ (keV)	γ^2 (keV)	(p,p_2) ℓ	s	Γ (keV)	γ^2 (keV)
2.1920	2^-	1	1	1.0	8.6												
		1	2	4.0	34												
		3	2	0.2	100												
2.2049	1^-	1	1	0.3	2.5	1	0	0.65	18								
		1	2	1.7	14												
		3	2	0.25	120												
2.2174	1^-	1	2	0.017	0.14	1	0	0.5	13								
2.2390	2^-	1	1	3.2	25												
		1	2	3.2	25												
2.2426	2^+	0	2	0.05	0.17												
		2	1	0.16	6.6												
2.2562	2^+	0	2	0.6	1.9	2	0	0.025	1.2								
		2	1	0.06	2.4												
		2	2	0.07	2.8												
2.2579	1^-	1	2	0.4	3.0	1	0	0.13	3.1								
2.3147	1^-	3	2	0.1	36	1	0	0.7	14								
2.3162	3^-	1	2	1.2	7.9												

Table 5.1 (continued)

E_p (MeV)	J^π	(p,p_0) ℓ	s	Γ (keV)	γ^2 (keV)	(p,α_0) ℓ	s	Γ (keV)	γ^2 (keV)	(p,p_1) ℓ	s	Γ (keV)	γ^2 (keV)	(p,p_2) ℓ	s	Γ (keV)	γ^2 (keV)
2.3359	1^-	1	2	0.005	0.032	1	0	0.18	3.5								
		3	2	0.015	5.1												
2.3508	0^-	1	1	1.9	127												
2.3686	1^+	0	1	0.2	0.53												
		2	2	0.1	3.0												
2.4110	2^+	0	2	0.04	0.1	2	0	1.0	31								
		2	1	0.06	1.6												
2.4370	2^-	3	2	0.15	38												
2.4503	1^-	1	1	0.13	0.67												
2.4540	1^-	1	1	9.0	46												
2.4600	3^-	1	2	10.0	50												
2.4622	1^-	1	2	2.5	13	1	0	0.4	5.6	1	0	0.07	23				
		3	2	0.05	12												
2.4696	2^-	1	2	0.01	0.049												
		3	2	0.1	24												
2.4734	1^+	2	1	0.1	2.4												

Table 5.1 (continued)

E_p (MeV)	J^π	(p,p_0) ℓ	s	Γ (keV)	γ^2 (keV)	(p,α_0) ℓ	s	Γ (keV)	γ^2 (keV)	(p,p_1) ℓ	s	Γ (keV)	γ^2 (keV)	(p,p_2) ℓ	s	Γ (keV)	γ^2 (keV)
2.4777	3^+	2	1	0.3	7.0												
2.5193	3^-	1	2	8.0	36												
2.5215	2^+	0	2	0.3	0.63	2	0	0.8	19								
		2	1	0.15	3.2												
		2	2	0.15	3.2												
2.5320	1^+	0	1	0.05	0.1												
2.5330	1^-	1	1	3.5	15.6					1	0	0.5	108				
		1	2	1.5	6.7												
2.5376	2^+	2	2	0.1	2.1	2	0	0.08	1.8								
2.5510	1^-	1	2	0.05	8.2					1	0	1.5	20				
2.5552	1^-	1	2	0.05	0.21	1	0	1.5	17								
2.5922	2^+	0	2	0.15	0.28	2	0	1.5	30								
		2	1	0.15	2.8												
2.6071	4^+	2	2	0.31	5.6	4	0	0.02	3.7								
2.6096	2^-	1	1	5.4	21												
2.6137	2^+	0	2	1.1	2.0	2	0	0.2	3.4								
		2	2	0.1	1.8												

Table 5.1 (continued)

E_p (MeV)	J^π	(p,p_0) ℓ	s	Γ (keV)	γ^2 (keV)	(p,α_0) ℓ	s	Γ (keV)	γ^2 (keV)	(p,p_1) ℓ	s	Γ (keV)	γ^2 (keV)	(p,p_2) ℓ	s	Γ (keV)	γ^2 (keV)
2.6154	1^-	1	2	0.03	0.12												
		3	2	0.07	11												
2.6192	1^+	0	1	0.2	0.37												
		2	1	0.1	1.8												
2.6260	1^+	0	1	0.175	0.32												
2.6267	1^-	1	2	0.3	1.1	1	0	1.6	15								
		3	2	0.1	16												
2.6527	2^-	1	2	0.33	1.2					1	1	0.07	8.1				
2.6554	1^+	0	1	0.3	0.53												
2.6747	2^+	2	2	0.4	6.3	2	0	0.009	0.14								
2.6884	1^-	1	1	0.053	0.18	1	0	0.36	3.0	1	0	0.1	9.8				
		1	2	0.078	0.27												
		3	2	0.037	5.1												
2.7007	1^-	1	2	0.3	1.0	1	0	0.3	2.4								
2.7078	2^+	2	2	0.275	4.1												
2.7095	2^-	1	2	0.2	0.67												

Table 5.1 (continued)

E_p (MeV)	J^π	(p,p_0) ℓ	s	Γ (keV)	γ^2 (keV)	(p,α_0) ℓ	s	Γ (keV)	γ^2 (keV)	(p,p_1) ℓ	s	Γ (keV)	γ^2 (keV)	(p,p_2) ℓ	s	Γ (keV)	γ^2 (keV)
2.7261	2^+	0	2	1.1	1.8	2	0	0.12	1.7	2	0	0.02	12				
2.7376	2^-	1	2	0.7	2.3					3	1	0.1	900				
2.7529	1^-	3	2	0.12	14												
2.7768	3^-	1	2	0.1	0.30	3	0	0.3	9.9								
		3	2	0.4	45												
2.7857	1^+	2	1	0.8	10												
2.7925	2^+	0	2	0.08	0.12	2	0	0.8	9.9								
2.8041	2^-	3	2	0.035	3.7												
2.8101	4^+	2	2	1.3	16	4	0	0.8	86								
2.8160	1^-	1	2	8.0	23												
2.8163	2^+	2	1	1.0	12	2	0	0.2	2.3								
2.8184	1^+	0	1	1.8	2.6												
2.8270	3^-	1	2	35.0	99												
2.8420	2^-	1	1	1.0	2.8					1	1	0.4	20				

Table 5.1 (continued)

E_p (MeV)	J^π	(p,p_0) ℓ	s	Γ (keV)	γ^2 (keV)	(p,α_0) ℓ	s	Γ (keV)	γ^2 (keV)	(p,p_1) ℓ	s	Γ (keV)	γ^2 (keV)	(p,p_2) ℓ	s	Γ (keV)	γ^2 (keV)
2.8821	4^+	2	2	0.65	7.0	4	0	0.03	2.7								
2.9099	2^+	0	2	0.9	1.2	2	0	0.05	0.48								
		2	2	0.05	0.52												
2.9108	1^+	2	1	0.6	6.2												
2.9153	1^-	1	2	0.6	1.5	1	0	0.07	0.36								
		3	2	0.04	3.4												
2.9238	2^-	1	2	4.5	11												
		3	2	1.0	83												
2.9297	3^+	2	1	0.65	6.5												
2.9338	1^-	1	1	0.25	0.62												
2.9409	2^-	3	2	0.37	30												
2.9466	1^-	3	2	0.2	16												
2.9830	1^-	1	1	5.5	13												
2.9890	3^-	1	2	37.0	85	3	0	1.0	20								
2.9891	1^-	3	2	0.08	5.8												

Table 5.1 (continued)

E_p (MeV)	J^π	(p,p_0) ℓ	s	Γ (keV)	γ^2 (keV)	(p,α_0) ℓ	s	Γ (keV)	γ^2 (keV)	(p,p_1) ℓ	s	Γ (keV)	γ^2 (keV)	(p,p_2) ℓ	s	Γ (keV)	γ^2 (keV)
2.9952	1^+	0	1	3.0	3.6												
3.0010	1^-	1	2	0.8	1.8	1	0	0.5	2.2								
3.0095	2^+	0	2	0.3	0.36												
3.0113	2^+	0	2	1.5	1.8	2	0	0.3	2.3								
		2	2	1.0	8.8												
3.0160	2^+	2	2	0.05	0.44	2	0	1.0	7.7								
3.0282	2^-	3	1	0.4	27												
3.0497	1^-	3	2	0.3	19												
3.0730	1^-	1	2	5.2	11	1	0	0.6	2.3								
		3	2	0.8	50												
3.0905	2^-	3	2	0.25	15												
3.0955	1^-	3	2	0.35	21												
3.0980	1^-	1	2	10.0	20	1	0	10.0	36								
		3	2	0.4	24												

Table 5.1 (continued)

E_p (MeV)	J^π	(p,p_0) ℓ	s	Γ (keV)	γ^2 (keV)	(p,α_0) ℓ	s	Γ (keV)	γ^2 (keV)	(p,p_1) ℓ	s	Γ (keV)	γ^2 (keV)	(p,p_2) ℓ	s	Γ (keV)	γ^2 (keV)
3.1020	2^-	1	1	2.0	4.0												
		1	2	8.0	16												
		3	2	0.7	41												
3.1050	1^-	1	2	3.0	6.0												
3.1112	2^-	1	1	12.0	24												
3.1235	1^-	3	2	0.3	17												
3.1410	4^+	2	2	0.85	6.1												
3.1485	1^+	2	1	16.0	110												
3.1675	3^-	1	2	1.8	3.4	3	0	0.08	1.1								
3.1745	2^+	0	2	0.35	0.36												

Table 5.2

Tentative Resonance Parameter Assignments for $^{35}Cl(p,x)$

E_p (MeV)	J^π	(p,p_0) ℓ	s	Γ (keV)	γ^2 (keV)	(p,α_0) ℓ	s	Γ (keV)	γ^2 (keV)	(p,p_1) ℓ	s	Γ (keV)	γ^2 (keV)	(p,p_2) ℓ	s	Γ (keV)	γ^2 (keV)
3.1840	2^-	1	2	18.0	33												
		3	2	18.0	900												
3.1885	3^+	2	2	0.25	1.7												
3.1945	1^-	3	2	0.5	25												
3.2280	1^-	3	2	3.5	160												
3.2350	1^-	1	2	6.0	11												
3.2410	2^-	1	2	35.0	61												
3.2475	1^-	1	1	15.0	26	1	0	15.0	42								
		1	2	15.0	26												
3.2610	1^-	1	2	4.5	7.7												
3.2760	2^+	0	2	7.0	6.6	2	0	0.7	3.3								
		2	2	3.0	18												
3.3060	2^+	0	2	0.6	0.55	2	0	0.08	0.36								
		2	2	0.6	3.4												
3.3112	1^+	2	2	0.45	2.6					0	1	0.03	0.14				

Table 5.2 (continued)

E_p (MeV)	J^π	(p,p_0) ℓ	s	Γ (keV)	γ^2 (keV)	(p,α_0) ℓ	s	Γ (keV)	γ^2 (keV)	(p,p_1) ℓ	s	Γ (keV)	γ^2 (keV)	(p,p_2) ℓ	s	Γ (keV)	γ^2 (keV)
3.3160	2^-	1	2	20.0	32												
3.3190	1^+	0	1	0.45	0.41					0	1	0.03	0.14				
3.3375	1^-	3	2	0.3	12	1	0	0.03	0.07	1	1	0.009	0.10	1	2	0.03	2.0
3.3395	2^+	2	2	0.9	4.9	2	0	0.09	0.38								
3.3482	1^-	3	2	1.0	38									1	2	0.08	5.0
3.3510	2^+	2	2	0.4	2.2	2	0	0.05	0.20					0	2	0.05	1.1
3.3535	1^+	2	2	0.4	2.2					0	1	0.05	0.22				
3.3850	1^-	1	2	5.0	7.5									1	2	0.1	5.4
3.4052	1^-	3	2	0.25	8.6					1	0	0.01	0.09				
3.4245	2^+	2	2	1.0	4.9									0	2	0.07	1.2
3.4425	2^+	0	2	0.65	0.54					2	0	0.04	1.9				
3.4440	2^-	1	2	20.0	29					1	1	2.0	17				
3.4459	1^-	3	2	0.6	19					1	0	0.04	0.34				
3.4499	3^-	1	2	4.0	5.7	3	0	0.5	4.0	3	0	0.03	15	1	2	0.09	3.8

Table 5.2 (continued)

E_p (MeV)	J^π	(p,p_0) ℓ	s	Γ (keV)	γ^2 (keV)	(p,α_0) ℓ	s	Γ (keV)	γ^2 (keV)	(p,p_1) ℓ	s	Γ (keV)	γ^2 (keV)	(p,p_2) ℓ	s	Γ (keV)	γ^2 (keV)
3.4504	2^+	2	2	1.3	6.2	2	0	0.1	0.34								
3.4553	1^-	3	2	0.15	4.8									1	2	0.15	6.2
3.4745	3^-	3	2	0.24	7.4												
3.4820	2^-	1	2	22.0	30					1	1	1.3	10				
3.5000	2^+	0	2	1.0	0.80	2	0	0.1	0.32								
3.5250	2^+	0	2	2.0	1.6	2	0	6.0	18								
3.5400	1^-	3	2	0.4	11												
3.5475	1^-	1	1	0.2	0.26	1	0	1.0	1.8								
3.5580	2^-	1	1	0.8	1.0												
		3	1	2.8	76												
3.5685	1^-	3	2	0.2	5.4	1	0	0.2	0.34					1	2	0.1	2.8
3.5720	2^-	1	2	45.0	58												
3.5725	1^-	3	2	0.2	5.3	1	0	1.0	1.7								
3.5897	1^+	2	1	0.35	1.4												

Table 5.2 (continued)

E_p (MeV)	J^π	(p,p_0) ℓ	s	Γ (keV)	γ^2 (keV)	(p,α_0) ℓ	s	Γ (keV)	γ^2 (keV)	(p,p_1) ℓ	s	Γ (keV)	γ^2 (keV)	(p,p_2) ℓ	s	Γ (keV)	γ^2 (keV)
3.5925	1^-	1	2	0.5	0.63	1	0	5.0	8.3								
3.6045	1^-	1	1	0.3	0.37	1	0	2.0	3.3					1	2	1.5	37
3.6094	2^+	2	1	0.9	3.5	2	0	0.08	0.22								
3.6124	1^-	1	1	0.15	0.19	1	0	0.4	0.64								
3.6305	1^-	3	2	0.6	15					1	0	0.1	0.59	1	2	0.1	2.3
3.6360	3^-	3	1	0.4	9.7	3	0	0.1	0.57								
3.6520	1^+	0	1	0.9	0.65					0	1	0.1	0.26				
3.6600	2^-	1	2	15.0	18												
3.6625	1^-	1	2	3.5	4.2	1	0	0.2	0.30								
3.6725	1^-	3	2	0.35	8.0									1	2	0.08	1.6
3.6785	1^-	1	1	0.1	0.12	1	0	0.1	0.15								
3.6800	1^-	1	2	0.3	0.35	1	0	0.1	0.15					1	2	0.1	2.0
3.6990	1^-	3	2	1.0	22	1	0	1.0	1.4					1	2	0.5	9.3

Table 5.2 (continued)

		(p,p_0)				(p,α_0)				(p,p_1)				(p,p_2)			
E_p (MeV)	J^π	ℓ	s	Γ (keV)	γ^2 (keV)	ℓ	s	Γ (keV)	γ^2 (keV)	ℓ	s	Γ (keV)	γ^2 (keV)	ℓ	s	Γ (keV)	γ^2 (keV)
3.7040	1^-	1	2	2.0	2.3	1	0	0.1	0.14					1	2	0.1	1.8
		3	2	0.5	11												
3.7105	1^-	1	2	2.4	2.7	1	0	0.2	0.28	1	0	0.3	1.5	1	2	0.3	5.4
3.7170	1^-	1	2	2.4	2.7					1	0	0.2	1.0				
3.7330	1^-	1	1	5.0	5.6												
3.7420	1^-	3	2	0.3	6.2												
3.7440	1^-	3	2	1.0	20.7									1	2	0.2	3.3
3.7640	0^-	1	1	16.0	18					1	1	1.0	4.6				
3.7665	1^-	3	2	0.4	8.0												
3.7700	3^-	1	2	20.0	22												
3.7720	1^-	3	2	0.4	8.0												
3.7775	1^-	1	1	0.04	0.04	1	0	0.1	0.13								
3.7790	1^-	1	1	0.1	0.11									1	2	2.0	30
3.7905	2^-	1	2	0.8	0.86									1	2	0.1	1.4

Table 5.2 (continued)

E_p (MeV)	J^π	(p,p_0) ℓ	s	Γ (keV)	γ^2 (keV)	(p,α_0) ℓ	s	Γ (keV)	γ^2 (keV)	(p,p_1) ℓ	s	Γ (keV)	γ^2 (keV)	(p,p_2) ℓ	s	Γ (keV)	γ^2 (keV)
3.7930	1^-	1	2	1.0	1.08	1	0	0.2	0.26								
3.8030	2^+	2	1	0.1	0.32	2	0	3.0	6.1								
3.8150	1^+	0	1	0.4	0.26												
		2	2	0.6	1.9												
3.8157	2^-	3	2	1.2	23												
3.8161	4^+	2	2	1.4	4.4	4	0	0.07	0.86								
3.8390	1^-	1	1	10.0	10	1	0	1.0	1.2								
3.8400	0^-	1	1	10.0	10					1	1	1.0	4.1				
3.8530	2^+	2	1	0.8	2.4	2	0	0.8	1.5								
3.8640	0^+	2	2	4.0	12									2	2	5.0	340
3.8652	3^-	1	2	1.5	1.5	3	0	0.2	0.79								
3.8677	3^-	1	2	1.5	1.5	3	0	0.35	1.4								
3.8720	0^-	1	1	9.0	9.2					1	1	4.0	15				
3.8752	1^-	1	2	1.0	1.0												

Table 5.2 (continued)

E_p (MeV)	J^π	(p,p_0) ℓ	s	Γ (keV)	γ^2 (keV)	(p,α_0) ℓ	s	Γ (keV)	γ^2 (keV)	(p,p_1) ℓ	s	Γ (keV)	γ^2 (keV)	(p,p_2) ℓ	s	Γ (keV)	γ^2 (keV)
3.8782	3^-	1	2	0.8	0.81	3	0	0.7	2.7								
3.8800	1^+	2	2	3.0	8.8									2	2	6.0	390
3.8850	3^-	1	2	35.0	35												
3.8920	3^-	1	2	0.7	0.70	3	0	0.45	1.7					1	2	0.45	5.0
3.8980	1^-	1	1	0.1	0.10									1	2	0.8	8.8
3.9000	1^-	3	2	0.8	13	1	0	0.9	1.0								
3.9075	2^+	2	1	0.4	1.1	2	0	0.6	1.1								
3.9180	3^-	1	2	0.8	0.79	3	0	0.1	0.36								
3.9360	0^+	2	2	6.0	17	0	0	4.0	3.4								
3.9455	0^+	2	2	1.0	2.8	0	0	3.0	2.6								
3.9480	3^-	1	2	27.0	26												
3.9640	1^-	3	2	0.5	7.7	1	0	0.6	0.62					1	2	0.4	3.7
3.9730	3^-	3	1	0.7	11	3	0	0.2	0.67								

Table 5.2 (continued)

E_p (MeV)	J^π	(p,p_0) ℓ	s	Γ (keV)	γ^2 (keV)	(p,α_0) ℓ	s	Γ (keV)	γ^2 (keV)	(p,p_1) ℓ	s	Γ (keV)	γ^2 (keV)	(p,p_2) ℓ	s	Γ (keV)	γ^2 (keV)
3.9730	2^+	2	1	0.7	1.9	2	0	2.0	3.2								
3.9945	1^+	2	2	0.9	2.4					2	1	0.08	1.1				

CHAPTER VI

ANALYSIS AND RESULTS

A. Statistical Tests

The statistical properties of nuclear levels are properly understood within the context of random matrix theory, in which the nuclear Hamiltonian is treated as a random variable with which is associated a probability distribution. Such theories do not consider the details of the Hamiltionian for the system; rather they typically impose a few fundamental symmetry requirements and make basic statistical assumptions. For instance, if it is assumed that the Hamiltonian for the system satisfies time reversal invariance, rotational invariance, and has statistically independent elements, then the resulting distributions of nuclear statistical properties (such as reduced widths and level spacings) are in good agreement with available data (Liou et al. 1972) This more modern approach has given theoretical justification to what were initially empirically derived relations describing nuclear systems such as the Porter-Thomas distribution (Porter 1956), a chi-squared distribution with one degree of freedom which describes the distribution of reduced widths for a single channel:

$$P(y) = \frac{1}{\sqrt{2\pi y}} \exp(-y/2) , \qquad y = \frac{\gamma^2}{\langle\gamma^2\rangle} \quad . \tag{6.1}$$

This relation cannot be applied to the total elastic widths measured in this experiment, since there are several partial widths involved in most channels. We therefore consider the partial widths separately, for example for 1^- states the distributions of the partial widths s=1, ℓ =1; s=2, ℓ =1 and s=2, ℓ =3 are considered. In general, the multi-channel amplitude distribution (Krieger and Porter 1963) is appropriate, but in practice the relative signs are not measured and the mixing ratios are not well determined. The α_0 decay channel measured in this experiment does provide a unique channel width,

which should obey the Porter-Thomas distribution. Resonances which had a statistically significant number of levels were compared to the Porter-Thomas distribution and an estimate obtained of the fraction of missing levels.

In figure 6.1 a plot is shown of the distribution of the cumulative square root of the variable y, normalized to a Porter Thomas distribution, for 1^- resonances with s = 1 and ℓ = 1. There were 20 resonances, and about 6% of the levels were missed. Since the strength is concentrated in the larger widths, this small missing fraction indicates that essentially all the strength was measured for this channel.

In figure 6.2 the Porter-Thomas distribution is plotted for 37 1^-, s = 2 f-wave resonances. The agreement is only qualitative; the calculated fraction of missed levels is 31%. This may indicate a problem with the fitting procedures, since the ℓ = 3 resonances have a strong effect in the differential cross section and should have been difficult to miss. One possible explanation is that the measurement of f-wave strength is intrinsically less sensitive than that for lower ℓ -values. Due to the very small Coulomb penetrability for this channel, a large change in the reduced width produces only a small effect in the differential cross section.

Figures 6.3 through 6.5 show the resonances which have s = 2 and ℓ = 1. In figure 6.3 data are plotted for 36 1^- states; the calculated fraction of levels missed is 3%. In figure 6.4 data are shown for 19 2^- states; the calculated fraction of levels missed is 4%. In figure 6.5 data are plotted for the 3^- states. Here the calculated fraction of missed levels was 6% for 19 resonances. In each of these latter cases the number of resonances was statistically significant, and the number of missed levels was quite small. It appears that virtually all of the resonance strength for these channels has been observed. Analyses have been performed for all elastic channels with more than a few levels, and there is qualitatively good agreement in almost all cases, even when the number of resonances is small. Thus it is quite likely that in this study very little strength in the elastic channels was missed.

Figure 6.1 Porter-Thomas distribution for 1^- proton widths with s = 1 and $\ell = 1$.

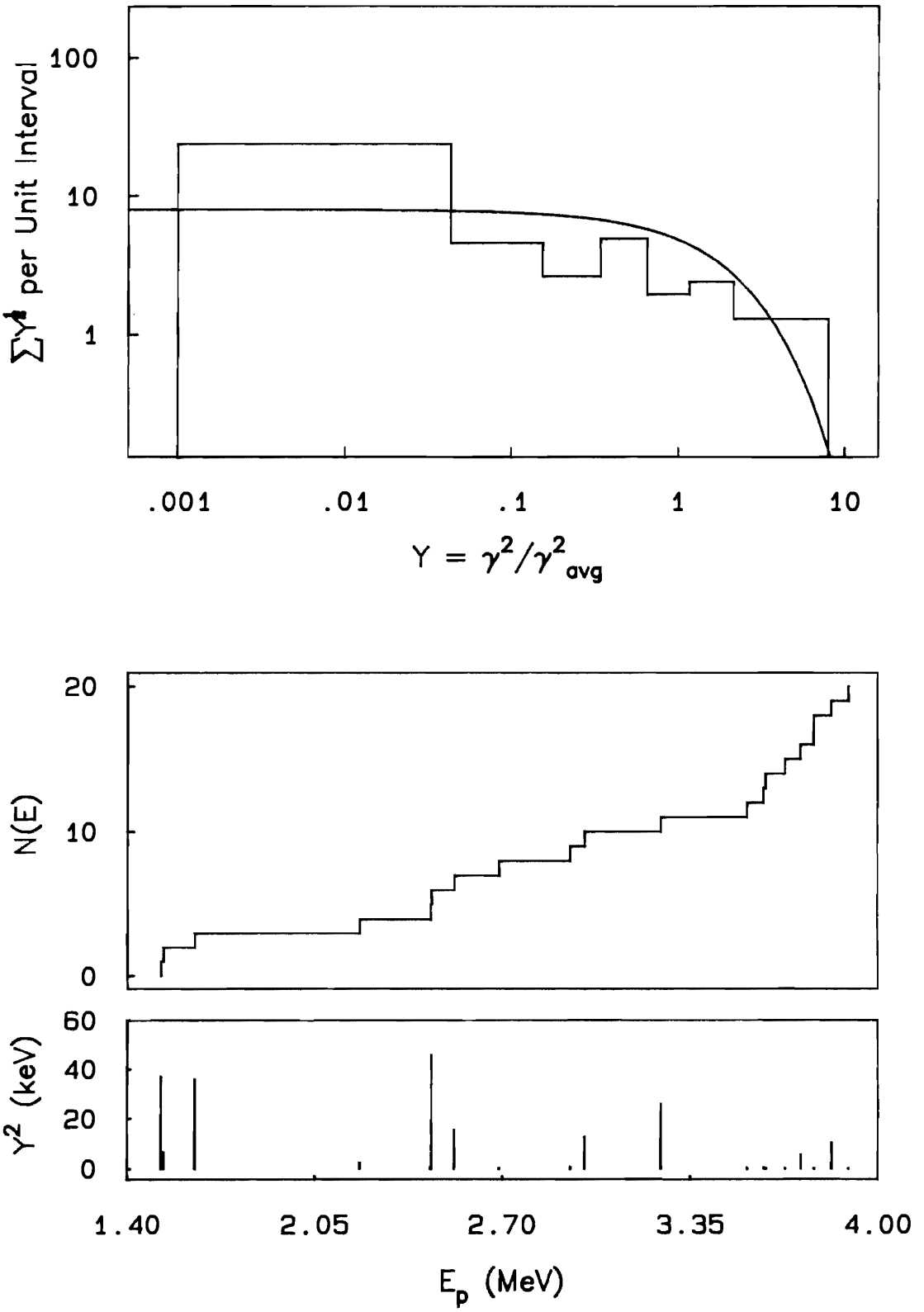
100
10
1
$\sum Y^4$ per Unit Interval
.001
.01
.1
1
10
$Y = \gamma^2/\gamma^2_{avg}$
20
10
0
N(E)
60
40
20
0
Y^2 (keV)
1.40
2.05
2.70
3.35
4.00
E_p (MeV)

Figure 6.2 Porter-Thomas distribution for 1^- proton widths with s = 2 and ℓ = 3.

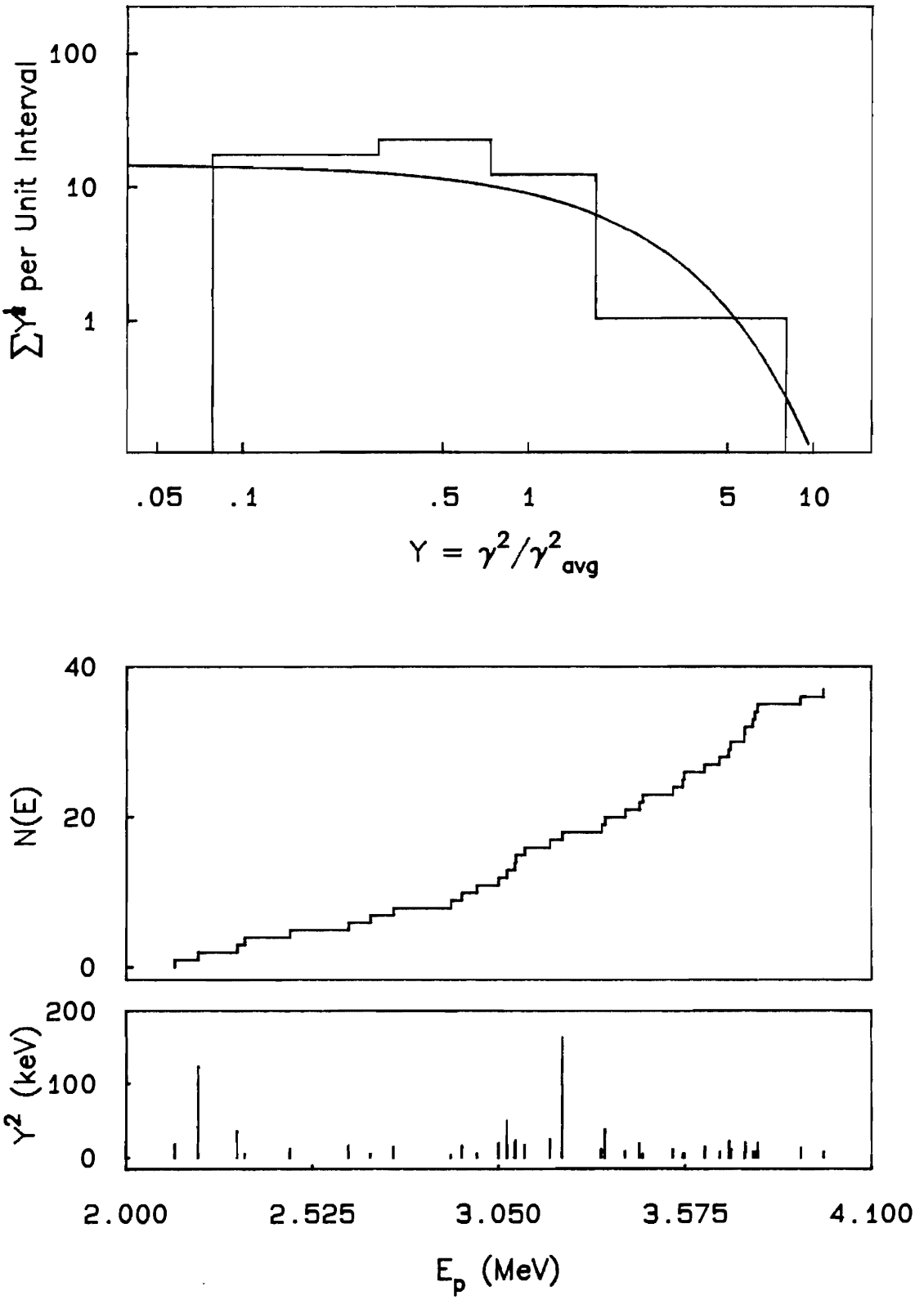
100
10
1
$\sum Y^4$ per Unit Interval
.05
.1
.5
1
5
10
$Y = \gamma^2/\gamma^2_{avg}$
40
20
0
N(E)
200
100
0
Y^2 (keV)
2.000
2.525
3.050
3.575
4.100
E_p (MeV)

Figure 6.3 Porter-Thomas distribution for 1^- proton widths with s = 2 and $\ell = 1$.

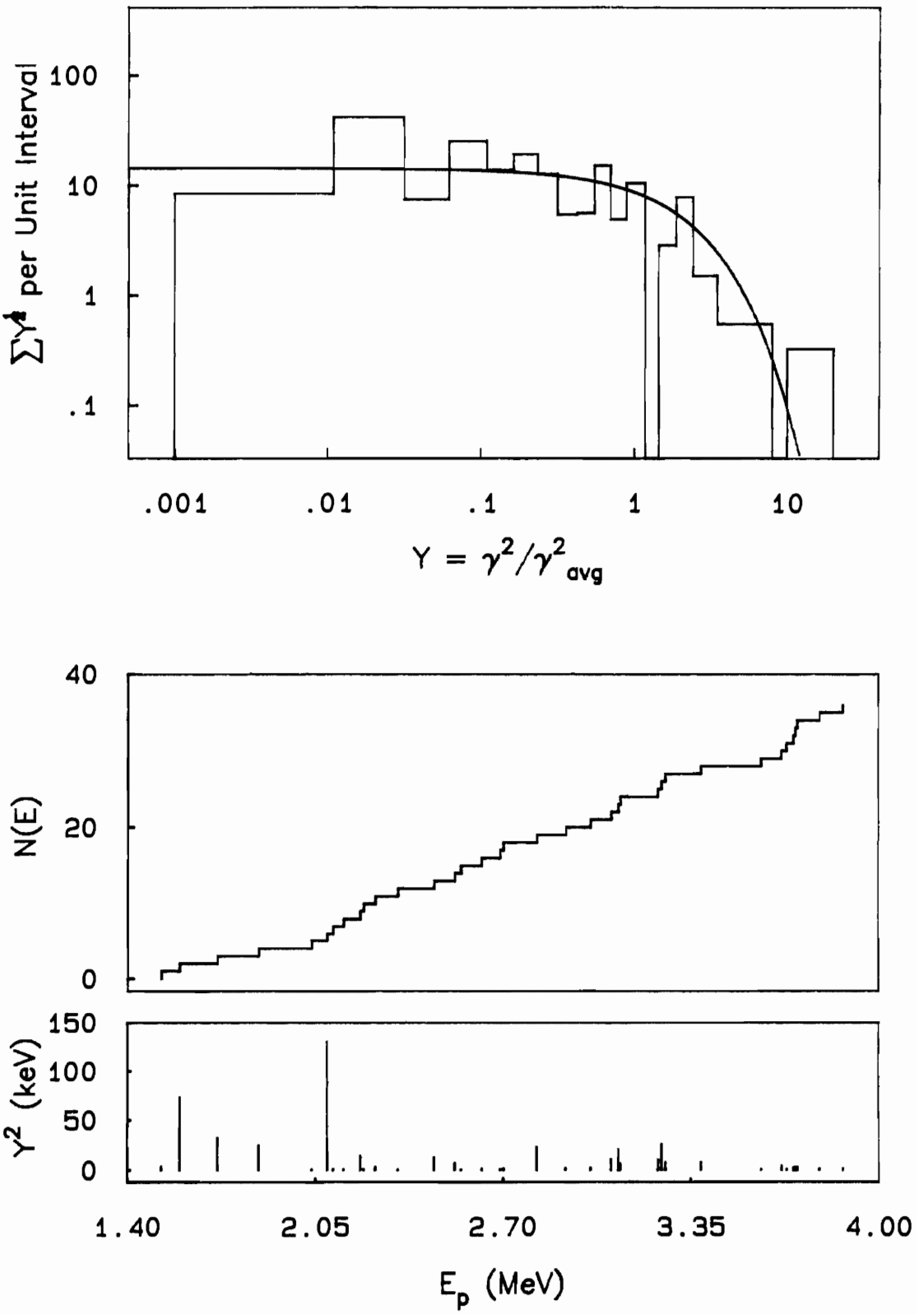
100
10
1
.1
$\sum Y^4$ per Unit Interval
.001
.01
.1
1
10
$Y = \gamma^2/\gamma^2_{avg}$
40
20
0
N(E)
150
100
50
0
Y^2 (keV)
1.40
2.05
2.70
3.35
4.00
E_p (MeV)

Figure 6.4 Porter-Thomas distribution for 2^- proton widths with s = 2 and $\ell = 1$.

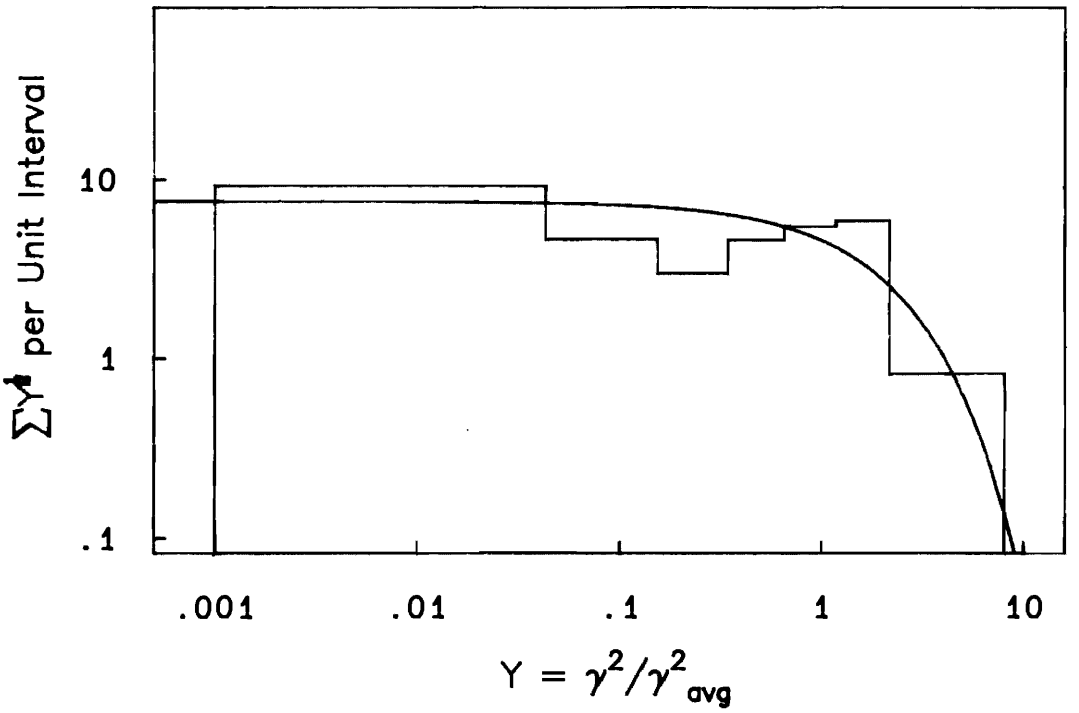
$\sum Y^4$ per Unit Interval
10
1
.1
.001
.01
.1
1
10
$Y = \gamma^2/\gamma^2_{avg}$

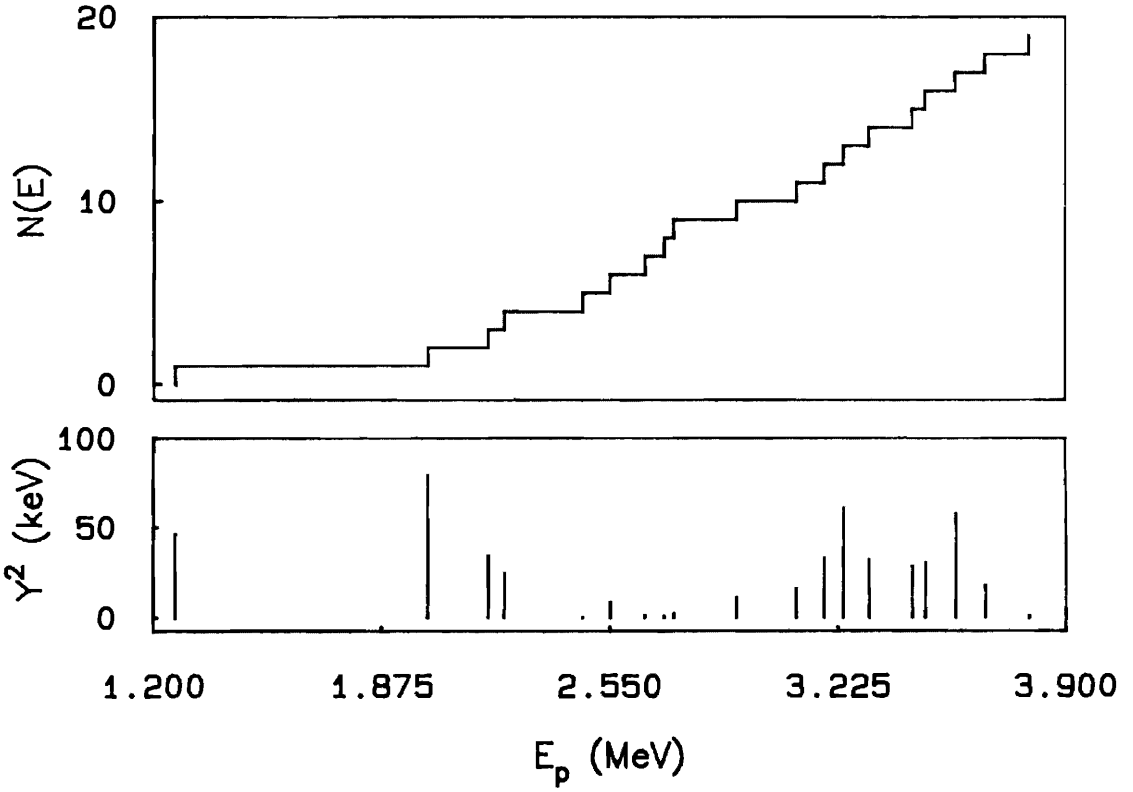
N(E)
20
10
0
Y^2 (keV)
100
50
0
1.200
1.875
2.550
3.225
3.900
E_p (MeV)

Figure 6.5 Porter-Thomas distribution for 3^- proton widths with s = 2 and $\ell = 1$.

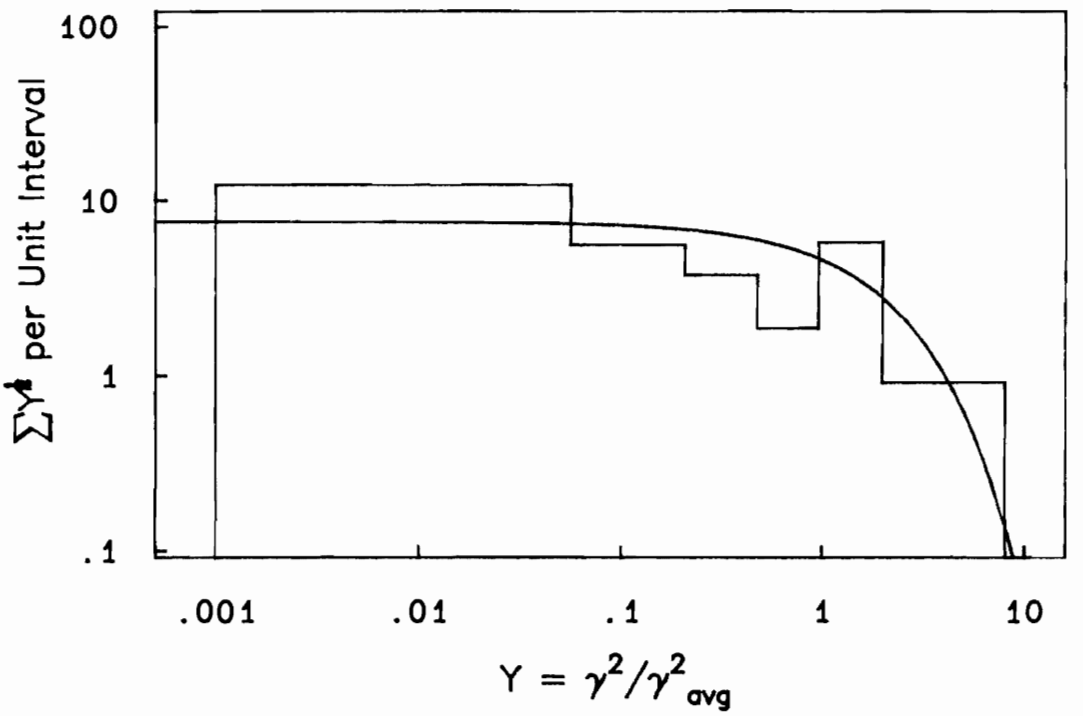
100
10
1
.1
$\sum Y^4$ per Unit Interval
.001
.01
.1
1
10
$Y = \gamma^2/\gamma^2_{avg}$

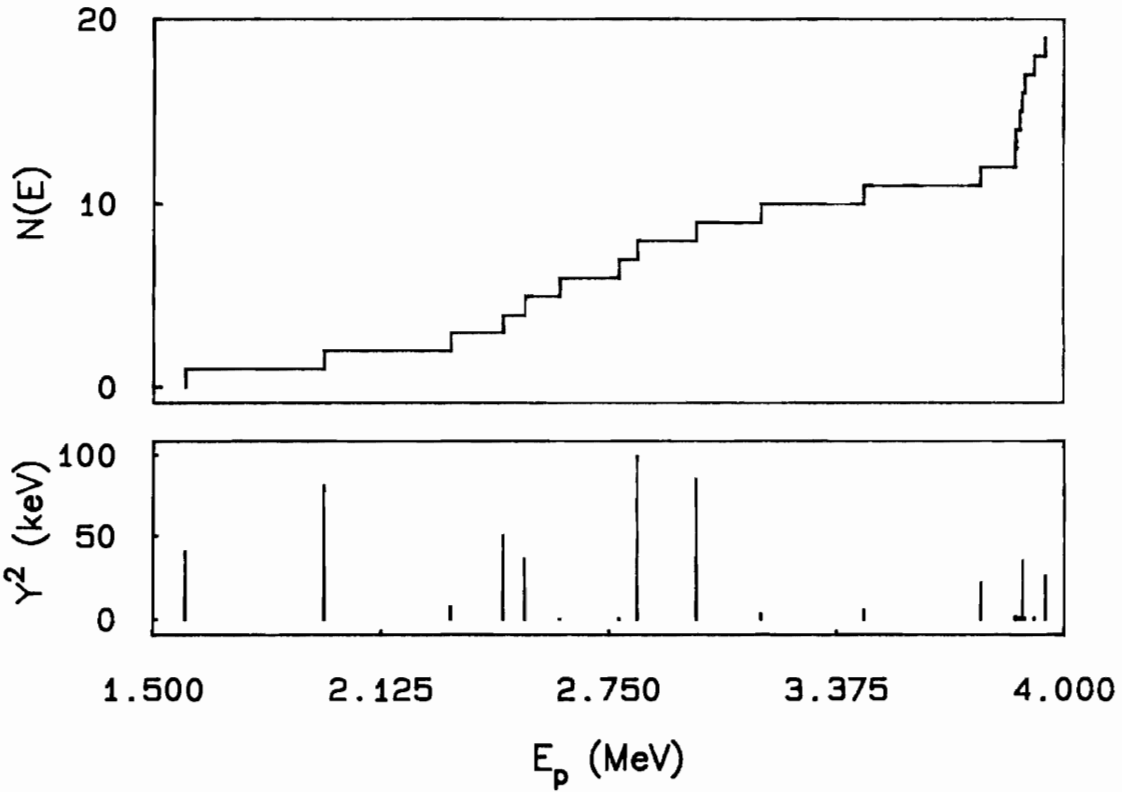
20
10
0
N(E)
100
50
0
Y^2 (keV)
1.500
2.125
2.750
3.375
4.000
E_p (MeV)

In figure 6.6 the data are plotted for the alpha strength for 2^+ resonances. Here there is no ambiguity about the number of channels, since only one exit channel is allowed and the Porter-Thomas distribution should apply. There are 25 levels and the fraction of missing levels is estimated to be 13%. In figure 6.7 the alpha strength data are shown for the 1^- resonances. There were 37 resonances observed, and the fraction of missing levels is 8%. Since most of the strength is concentrated in the larger levels, and since the fit to the Porter-Thomas curve is rather good, it is probable that nearly all the strength in these channels has been observed.

The level spacing distributions did not agree very well with the Wigner distribution. Some difficulties may be caused by the energy dependence of the level density, which is evident in the plots of N(E) versus E_p in figures 6.1 through 6.7. This effect could be removed using a model for the energy dependence. However, since the number of levels is already small, further detailed analysis does not seem appropriate for these data. When N(E) versus E_p was fit approximately with the prescription of Gilbert and Cameron (1965), in most cases the resulting nuclear temperature was about 1.5 to 2.0 MeV.

B. Resonance Strengths

The resonance laboratory width $\Gamma=2P\gamma^2$ is a function of kinematic effects as well as nuclear structure effects. The penetrability factor P changes by several orders of magnitude for various values of ℓ and for varying E_p. The nuclear structure information is contained in the reduced widths $\gamma_{\lambda c}^2 = (\hbar^2/2M_c a_c)(\langle\phi_c|X_c\rangle)^2$.

The reduced widths, cumulative reduced width, and number of resonances versus proton energy for a given spin and parity are plotted in figures 6.8 through 6.21. The reduced width plot displays the magnitudes of the individual widths most clearly, so that large single or slightly fragmented states are easily seen. Highly fragmented states, as well as large individual states, are apparent in the width sum plots. The resonance position plot most clearly shows level density trends since the small states are not obscured.

Figure 6.6 Porter-Thomas distribution for 2^+ alpha widths.

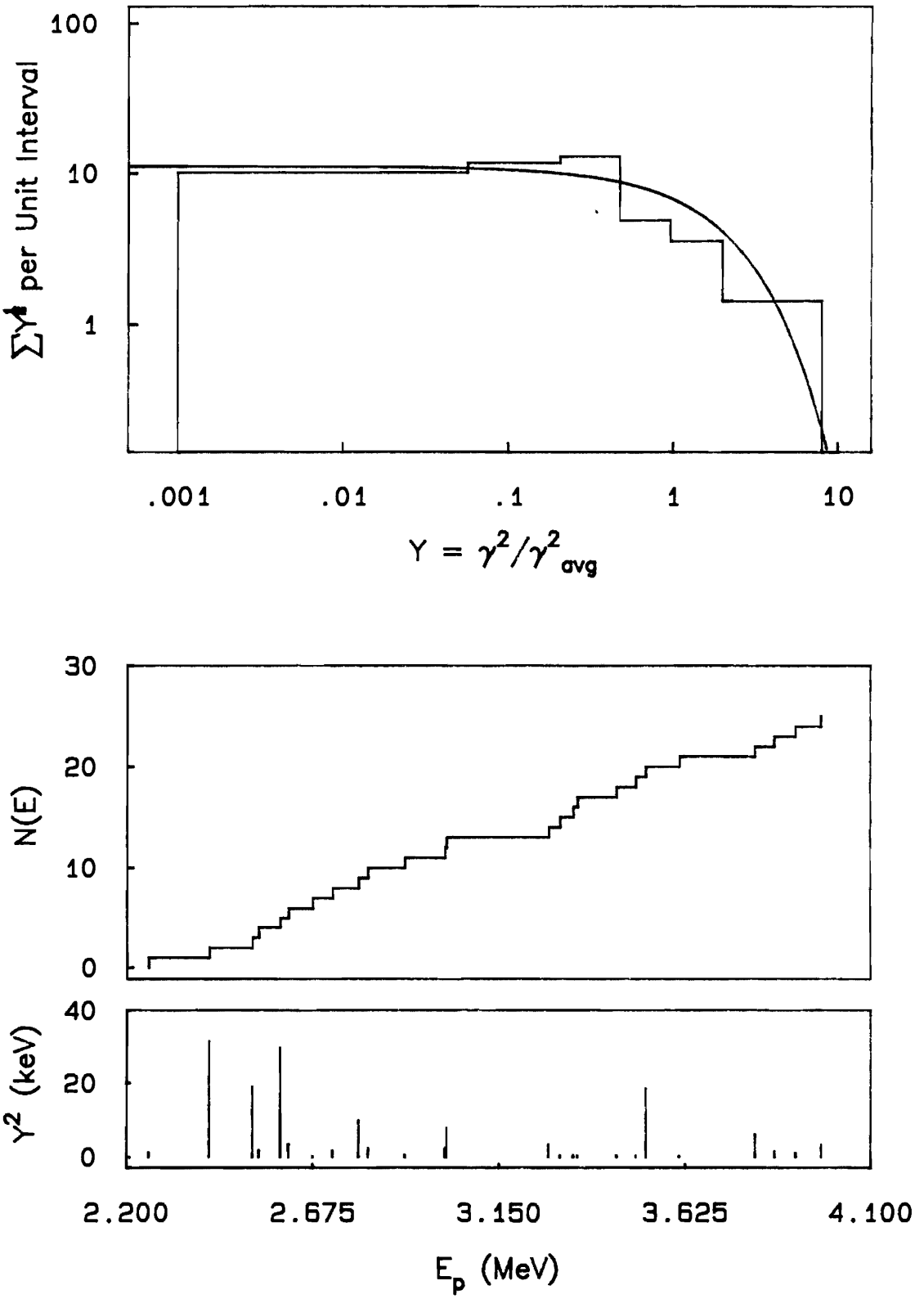
100
10
1
$\sum Y^4$ per Unit Interval
.001
.01
.1
1
10
$Y = \gamma^2/\gamma^2_{avg}$
30
20
10
0
N(E)
40
20
0
Y^2 (keV)
2.200
2.675
3.150
3.625
4.100
E_p (MeV)

Figure 6.7 Porter-Thomas distribution for 1^- alpha widths.

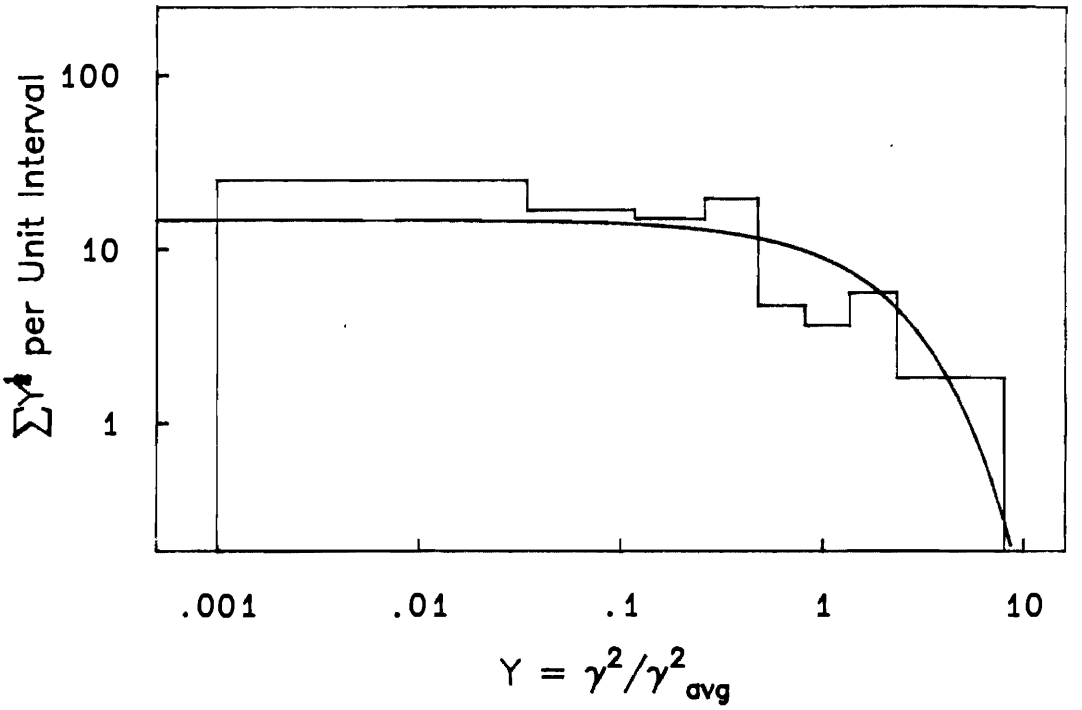
100
10
1
$\sum Y^4$ per Unit Interval
.001
.01
.1
1
10
$Y = \gamma^2/\gamma^2_{avg}$

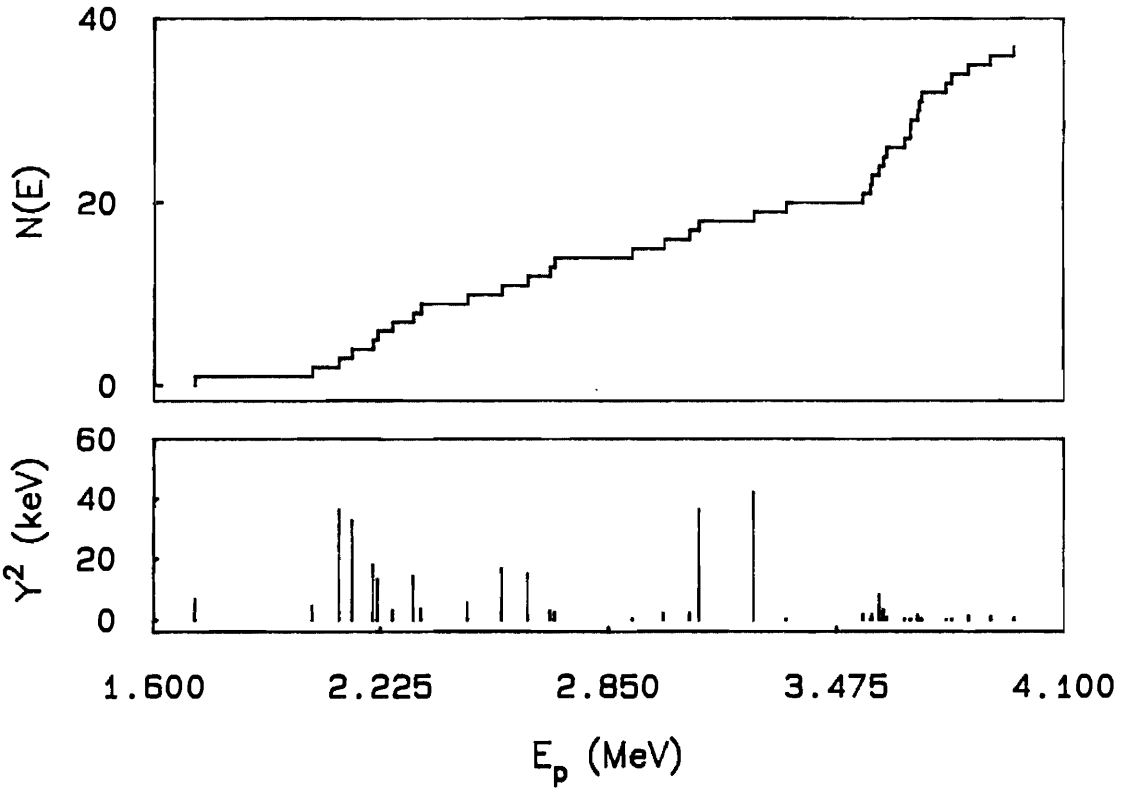
40
20
0
N(E)
60
40
20
0
Y^2 (keV)
1.600
2.225
2.850
3.475
4.100
E_p (MeV)

Figure 6.8 Proton reduced widths versus energy for $J^{\pi} = 0^{-}$ p-wave resonances.

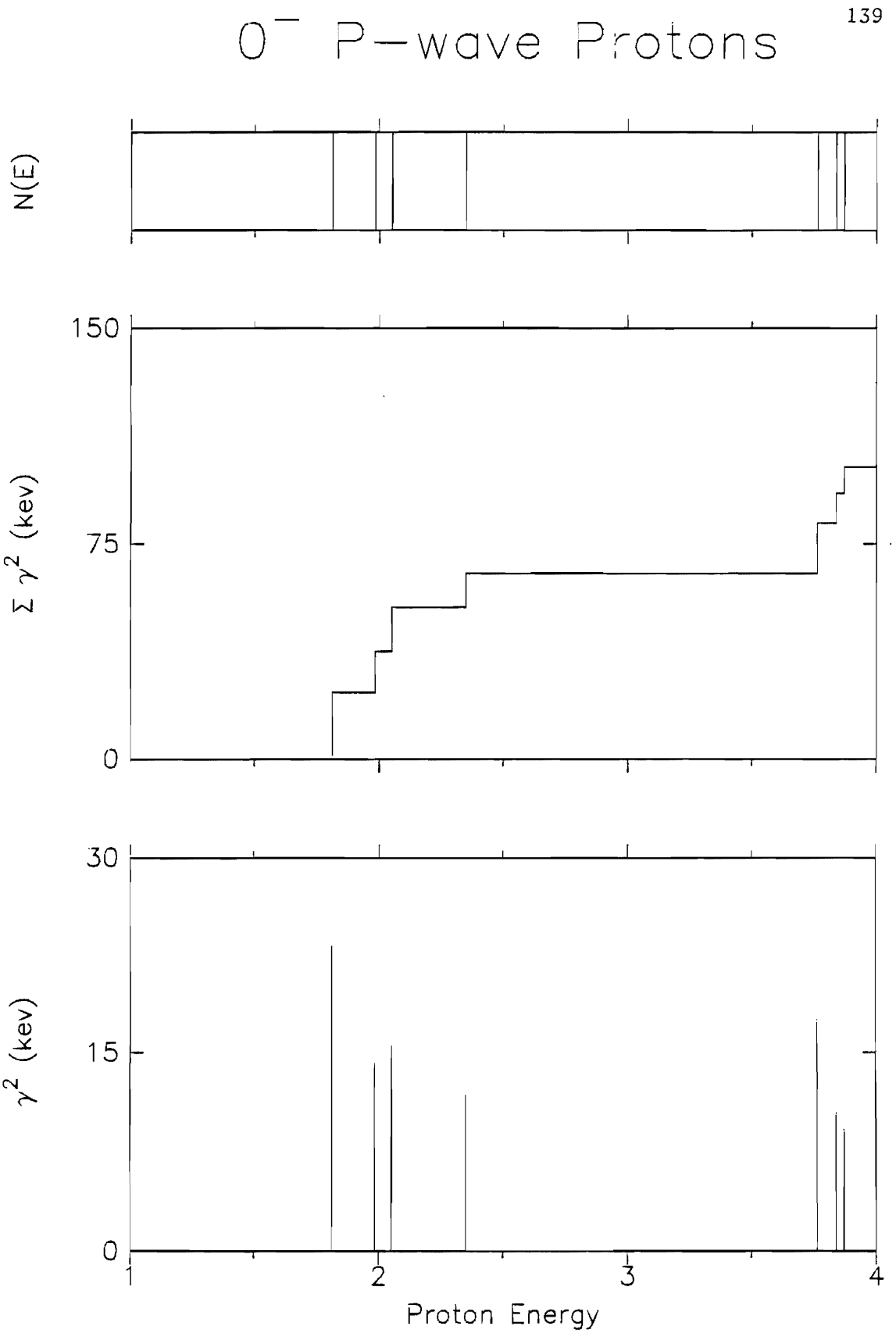
0⁻ P-wave Protons
N(E)
150
75
0
Σ γ² (kev)
30
15
0
γ² (kev)
1
2
3
4
Proton Energy

Figure 6.9 Proton reduced widths versus energy for $J^{\pi} = 0^{+}$ d-wave resonances.

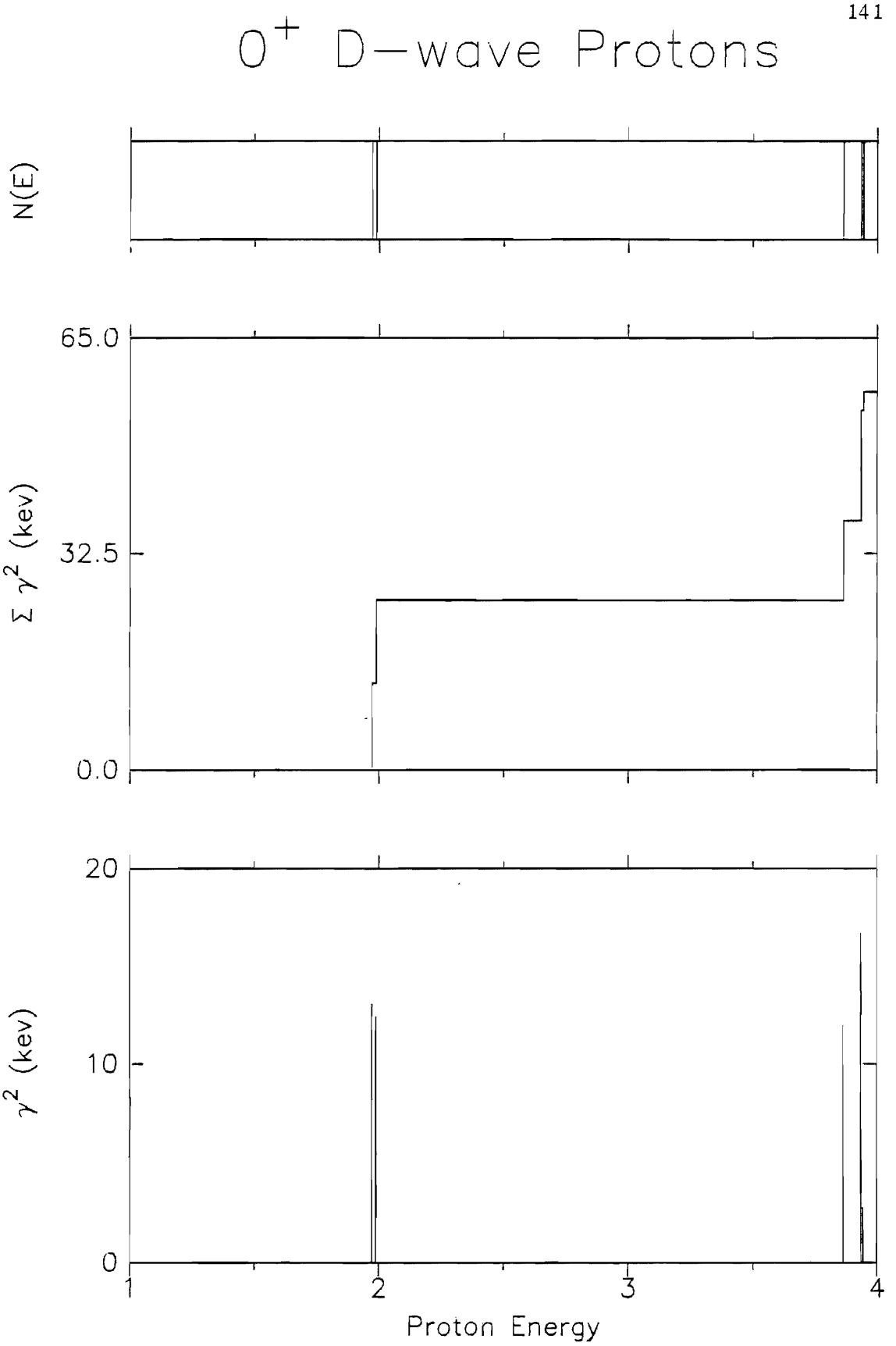
0+ D-wave Protons
N(E)
65.0
32.5
0.0
Σ γ2 (kev)
20
10
0
γ2 (kev)
1
2
3
4
Proton Energy

Figure 6.10 Proton reduced widths versus energy for $J^{\pi} = 1^-$ p-wave resonances. Both channel spin values are included.

1^- P—wave Protons

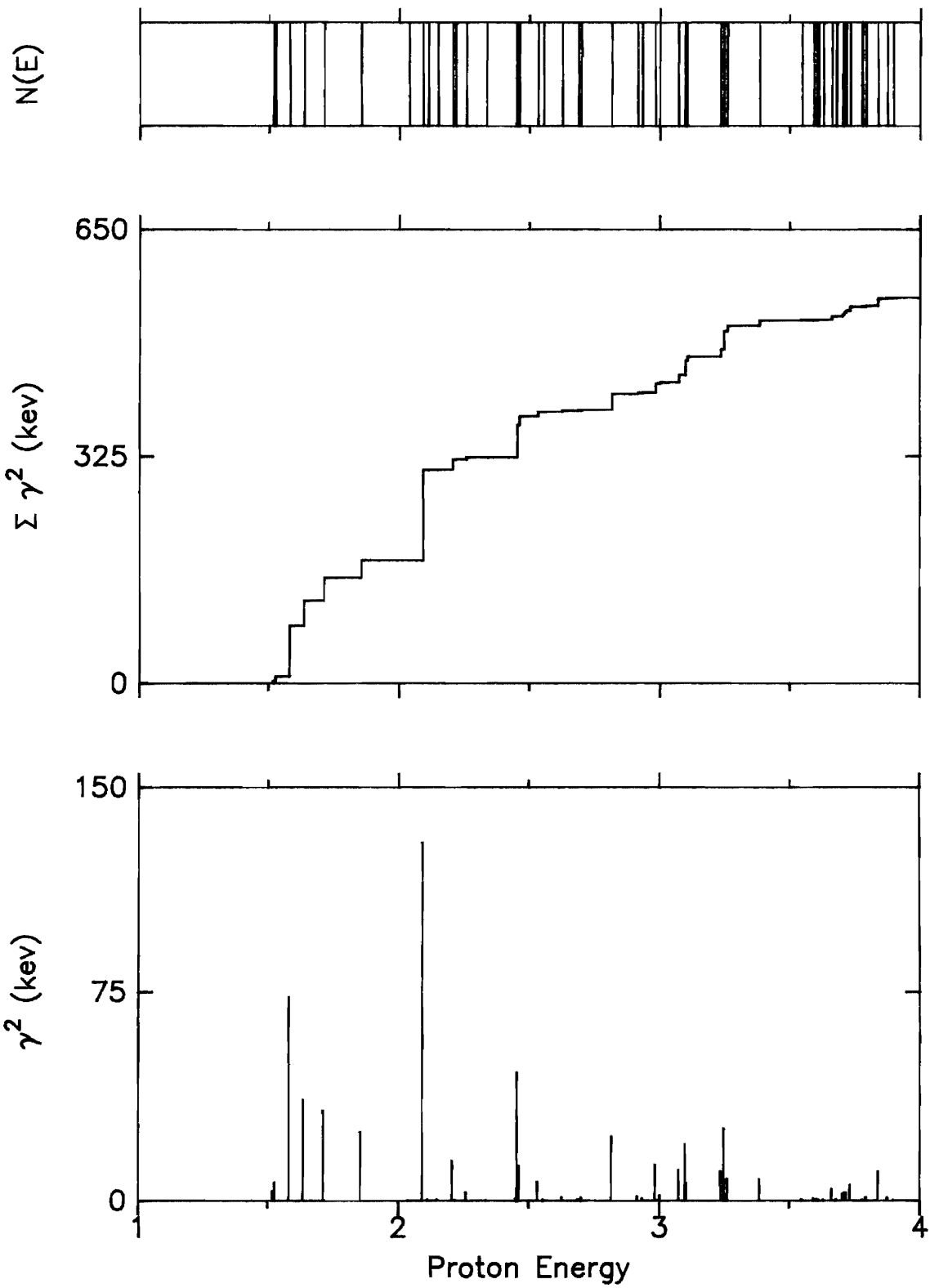

Figure 6.11 Proton reduced widths versus energy for $J^{\pi} = 1^-$ f-wave resonances.

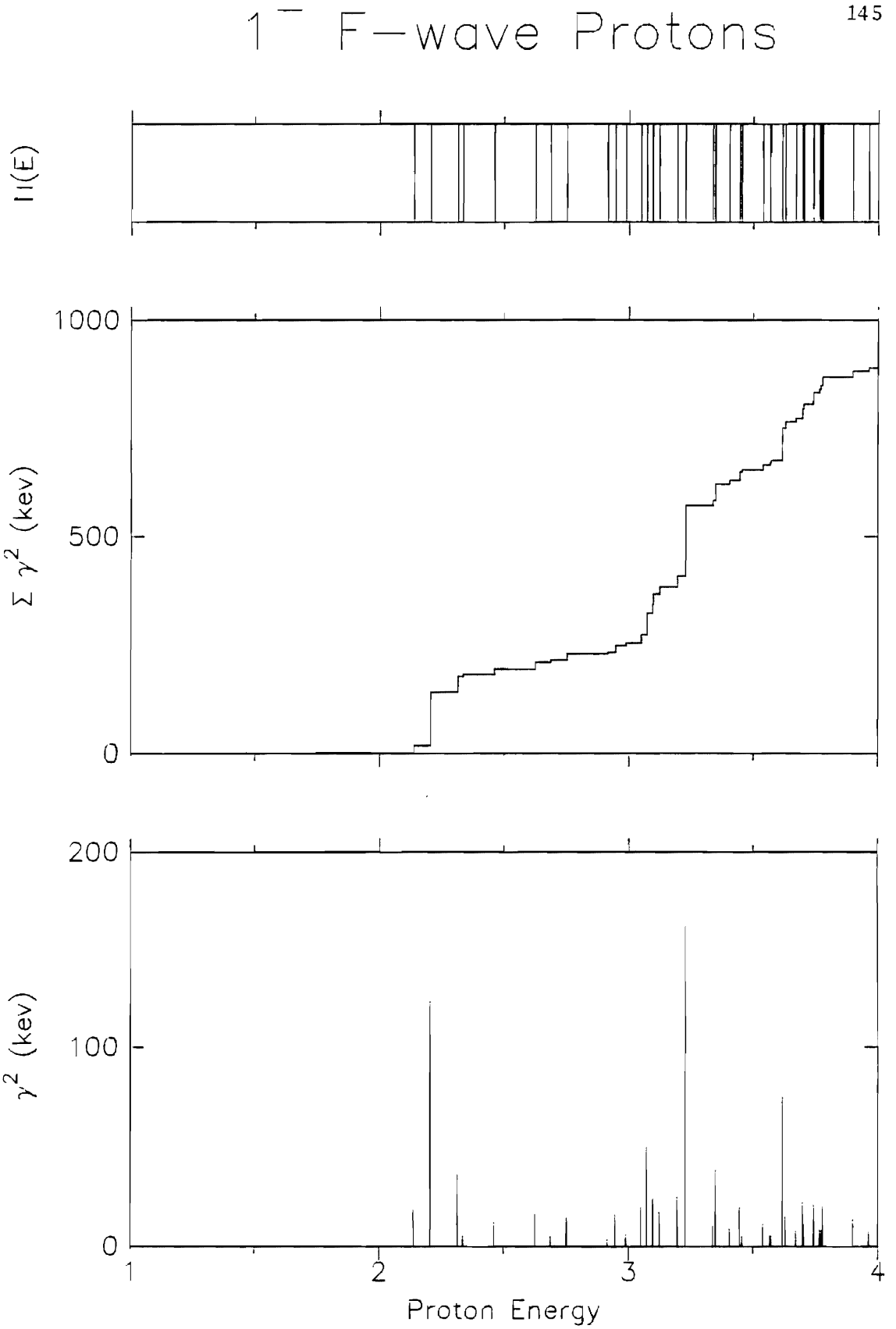
1⁻ F—wave Protons
Π(E)
1000
500
0
Σ γ² (kev)
200
100
0
γ² (kev)
1
2
3
4
Proton Energy

Figure 6.12 Proton reduced widths versus energy for $J^{\pi} = 1^{+}$ s-wave resonances.

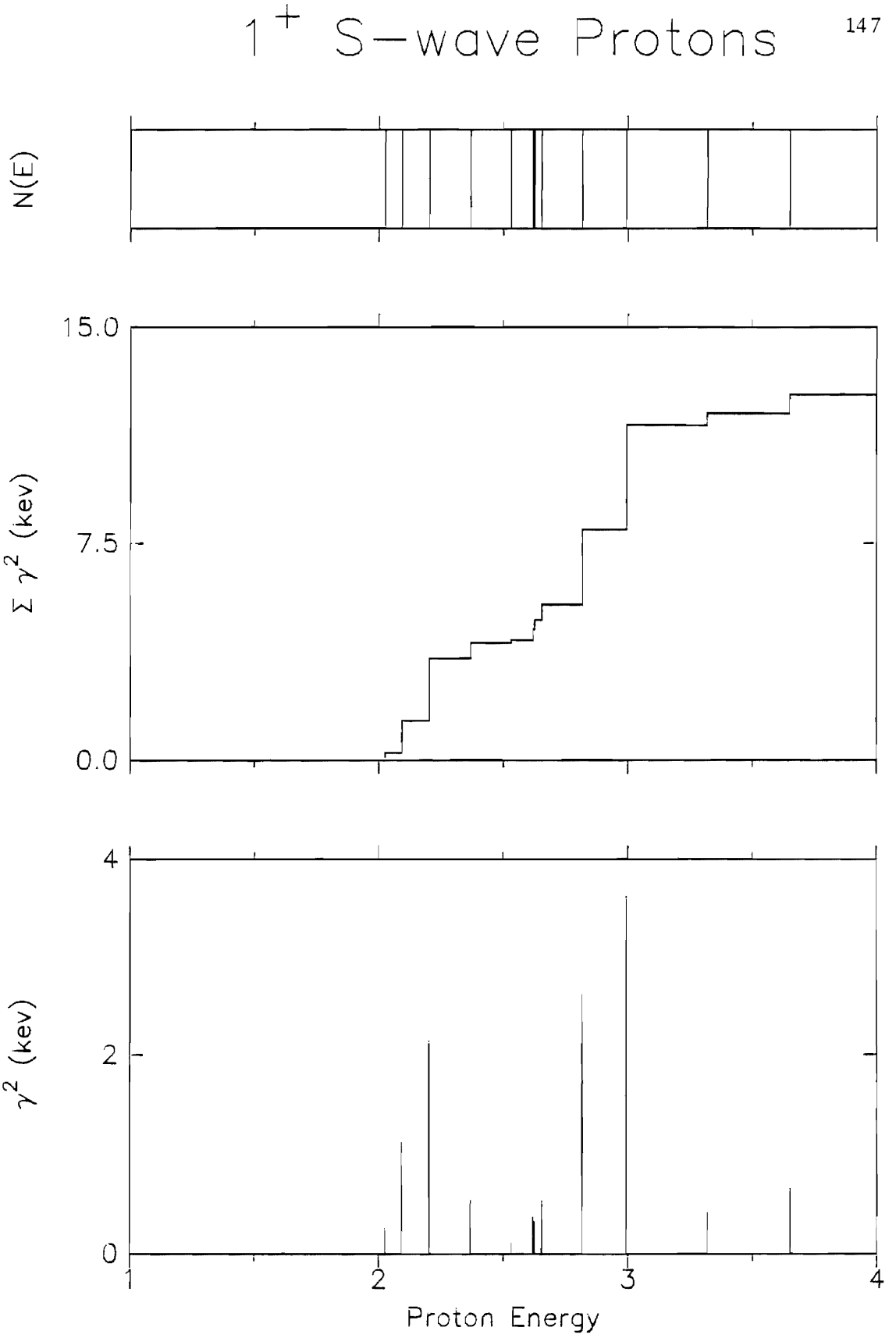
1+ S-wave Protons
N(E)
15.0
7.5
0.0
Σ γ² (kev)
4
2
0
γ² (kev)
1
2
3
4
Proton Energy

Figure 6.13 Proton reduced widths versus energy for $J^{\pi} = 1^{+}$ d-wave resonances. Both channel spin values are included.

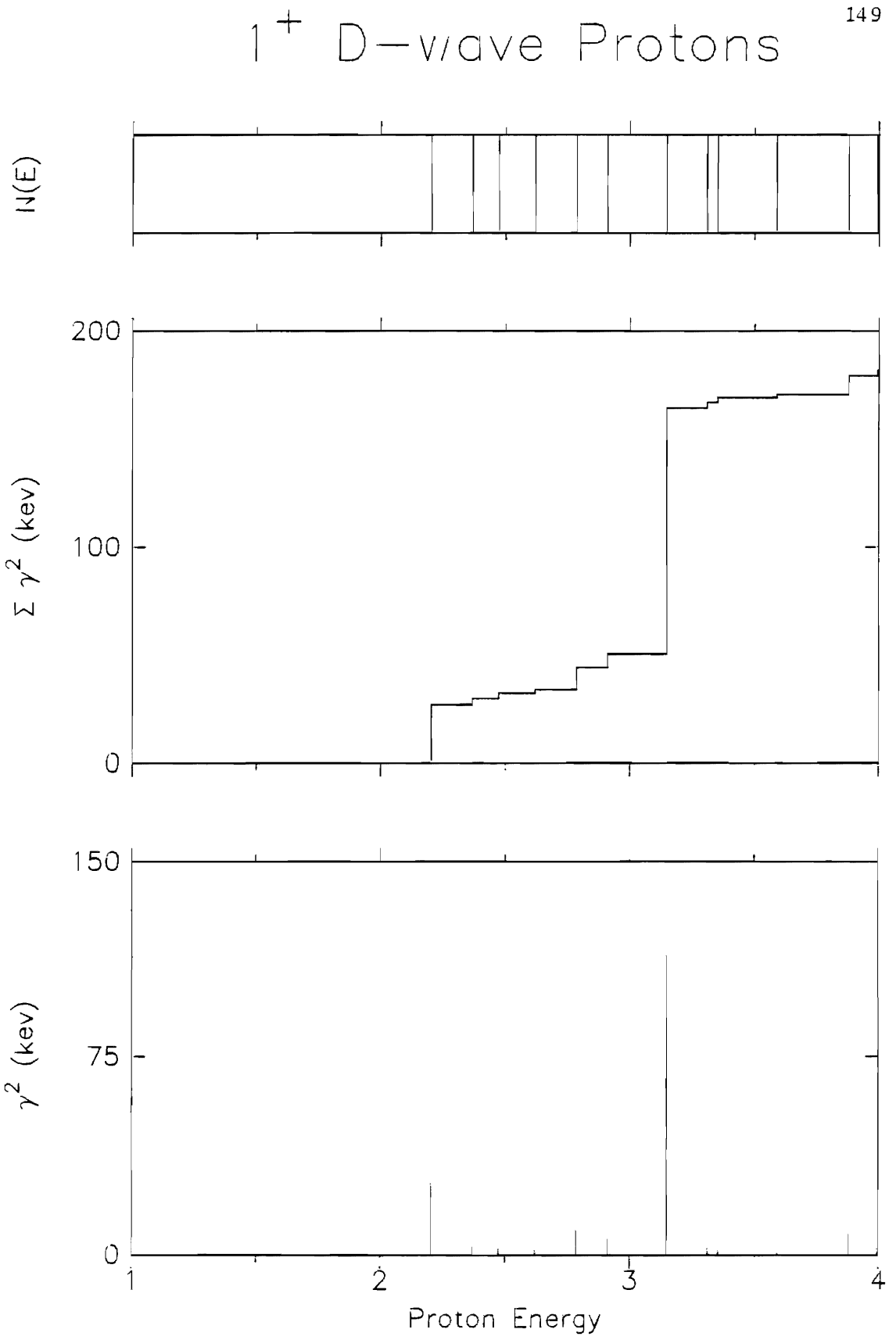
1+ D-wave Protons
N(E)
200
100
0
Σ γ² (kev)
150
75
0
γ² (kev)
1
2
3
4
Proton Energy

Figure 6.14 Proton reduced widths versus energy for $J^{\pi} = 2^{-}$ p-wave resonances. Both channel spin values are included.

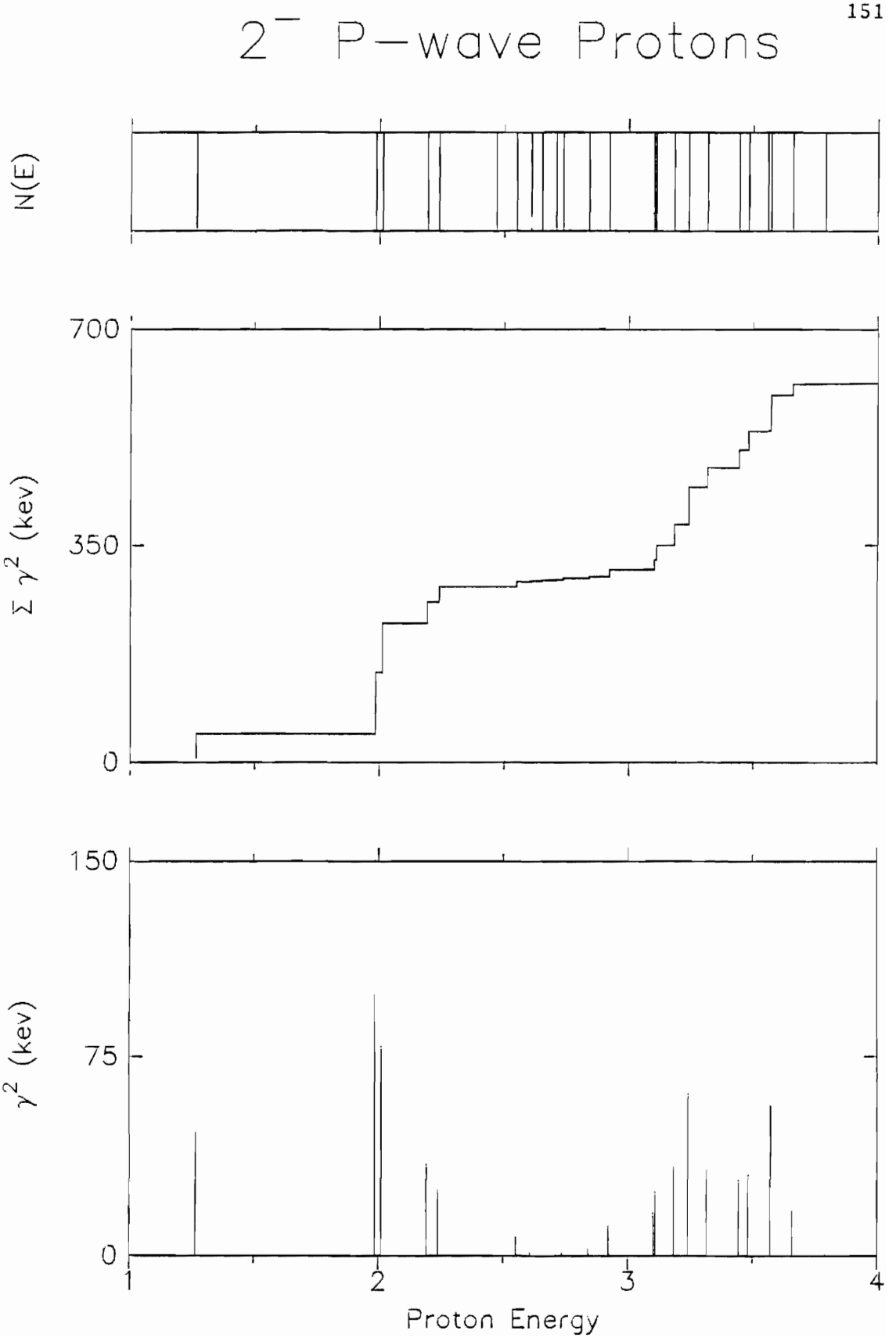
2⁻ P-wave Protons
N(E)
700
350
0
Σ γ² (kev)
150
75
0
γ² (kev)
1
2
3
4
Proton Energy

Figure 6.15 Proton reduced widths versus energy for $J^{\pi} = 2^{-}$ f-wave resonances. Both channel spin values are included.

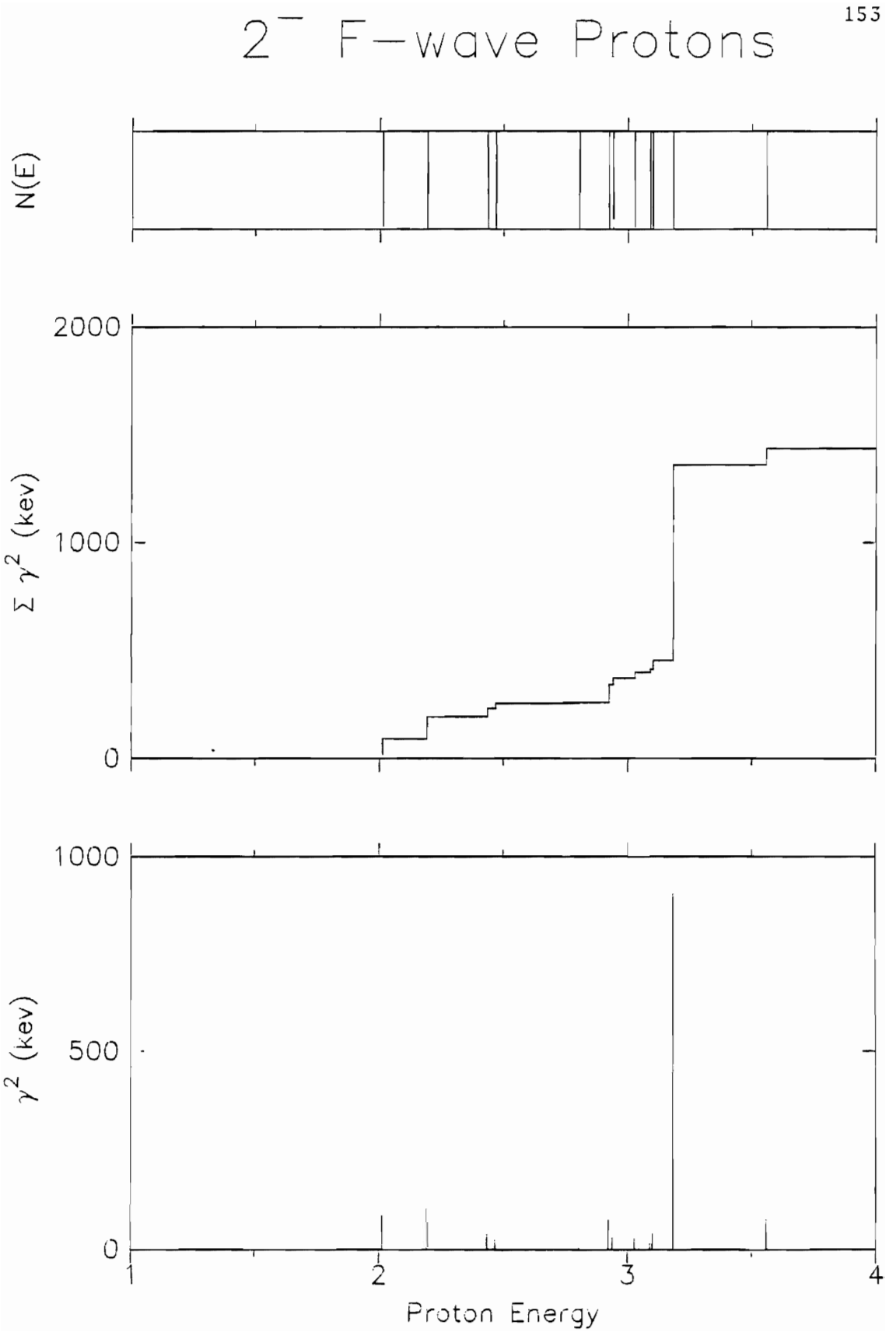
2⁻ F-wave Protons
N(E)
2000
1000
0
Σ γ² (kev)
1000
500
0
γ² (kev)
1
2
3
4
Proton Energy

Figure 6.16 Proton reduced widths versus energy for $J^{\pi} = 2^{+}$ s-wave resonances.

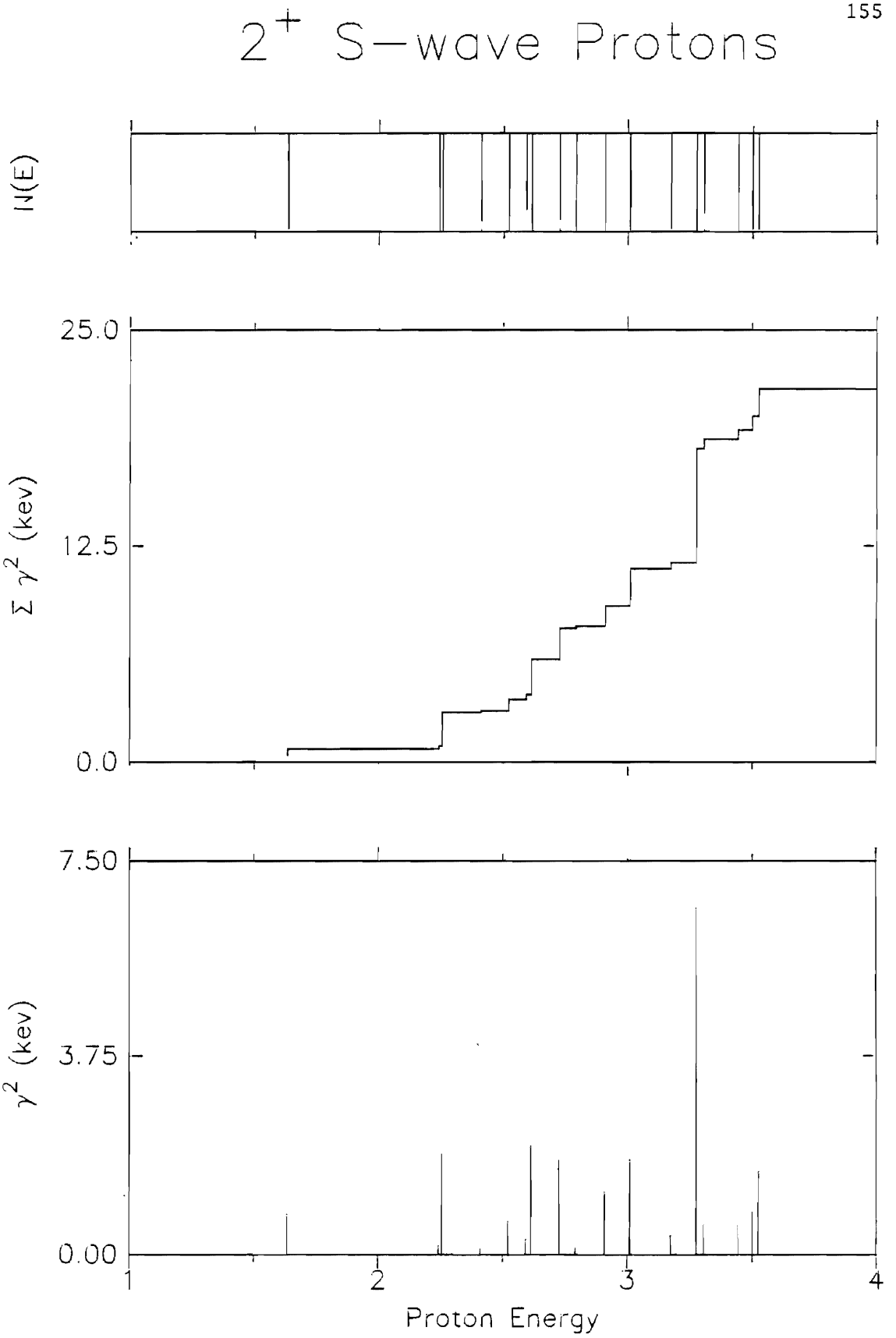
2+ S—wave Protons
N(E)
25.0
12.5
0.0
Σ γ2 (kev)
7.50
3.75
0.00
γ2 (kev)
1
2
3
4
Proton Energy

Figure 6.17 Proton reduced widths versus energy for $J^{\pi} = 2^{+}$ d-wave resonances. Both channel spin values are included.

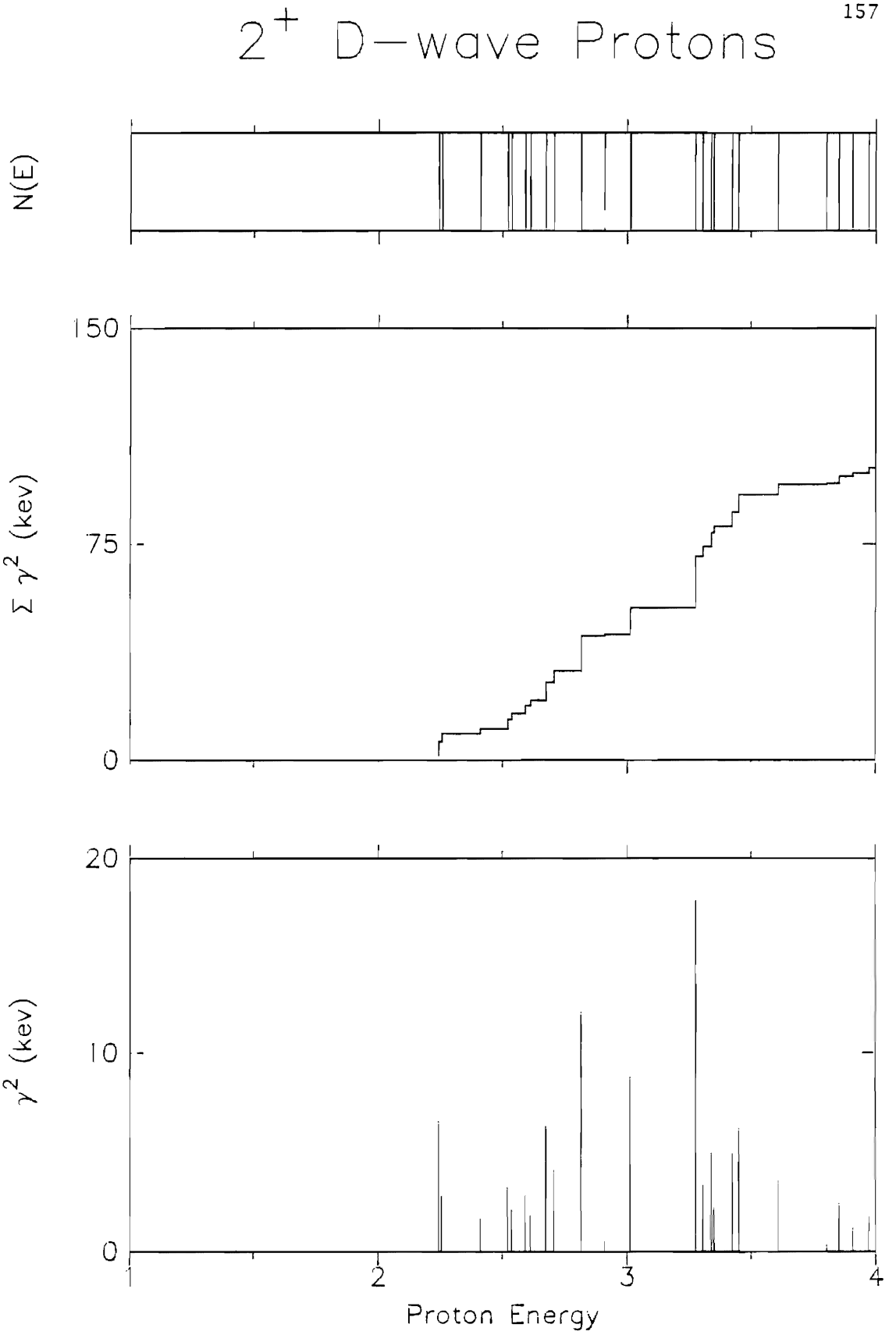
2+ D-wave Protons
N(E)
150
75
0
Σ γ2 (kev)
20
10
0
γ2 (kev)
1
2
3
4
Proton Energy

Figure 6.18 Proton reduced widths versus energy for $J^{\pi} = 3^{-}$ p-wave resonances.

3^- P-wave Protons

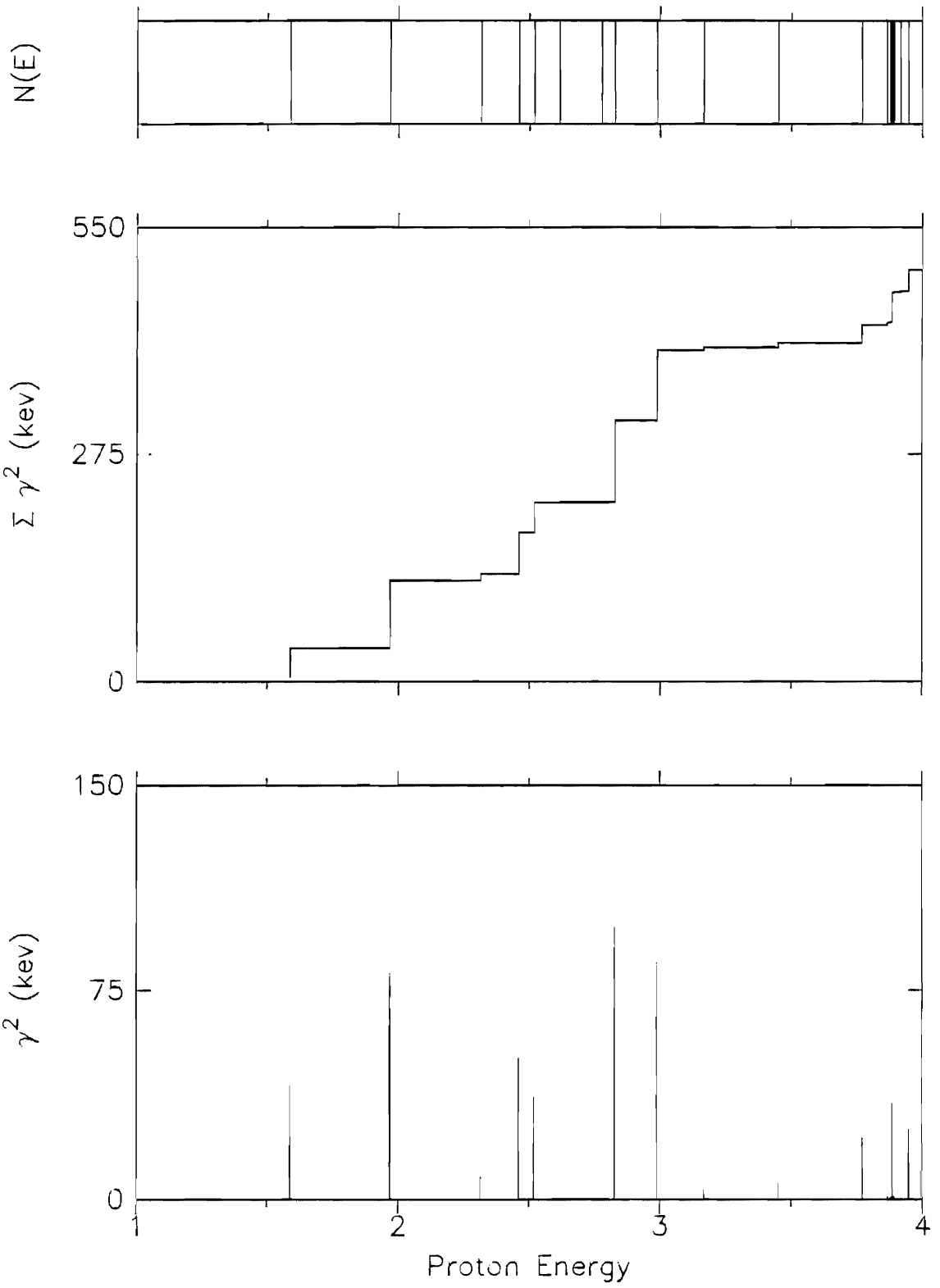

Figure 6.19 Proton reduced widths versus energy for $J^{\pi} = 3^-$ f-wave resonances.

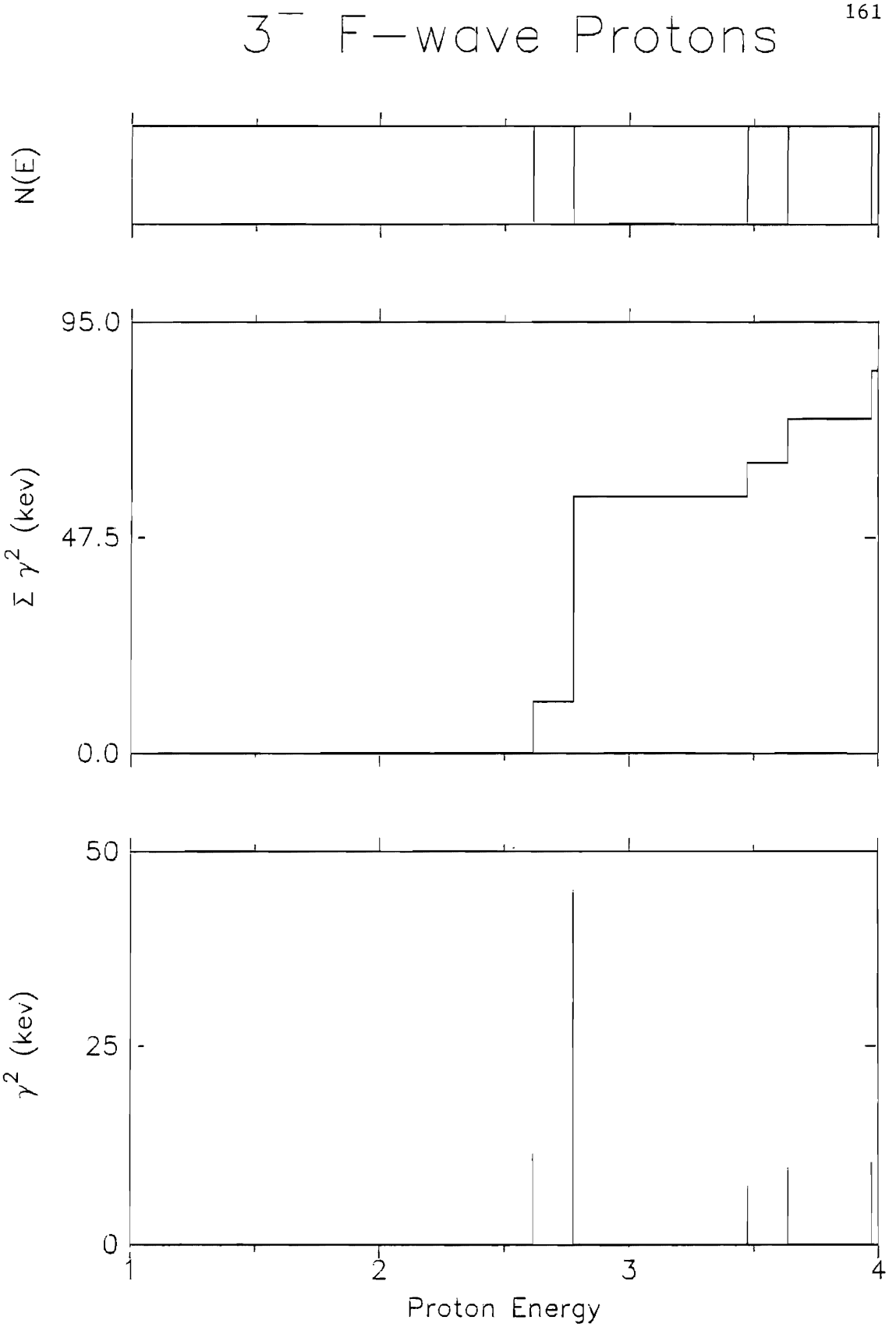
3⁻ F-wave Protons
N(E)
95.0
47.5
0.0
Σ γ² (kev)
50
25
0
γ² (kev)
1
2
3
4
Proton Energy

Figure 6.20 Proton reduced widths versus energy for $J^{\pi} = 3^{+}$ d-wave resonances. Both channel spin values are included.

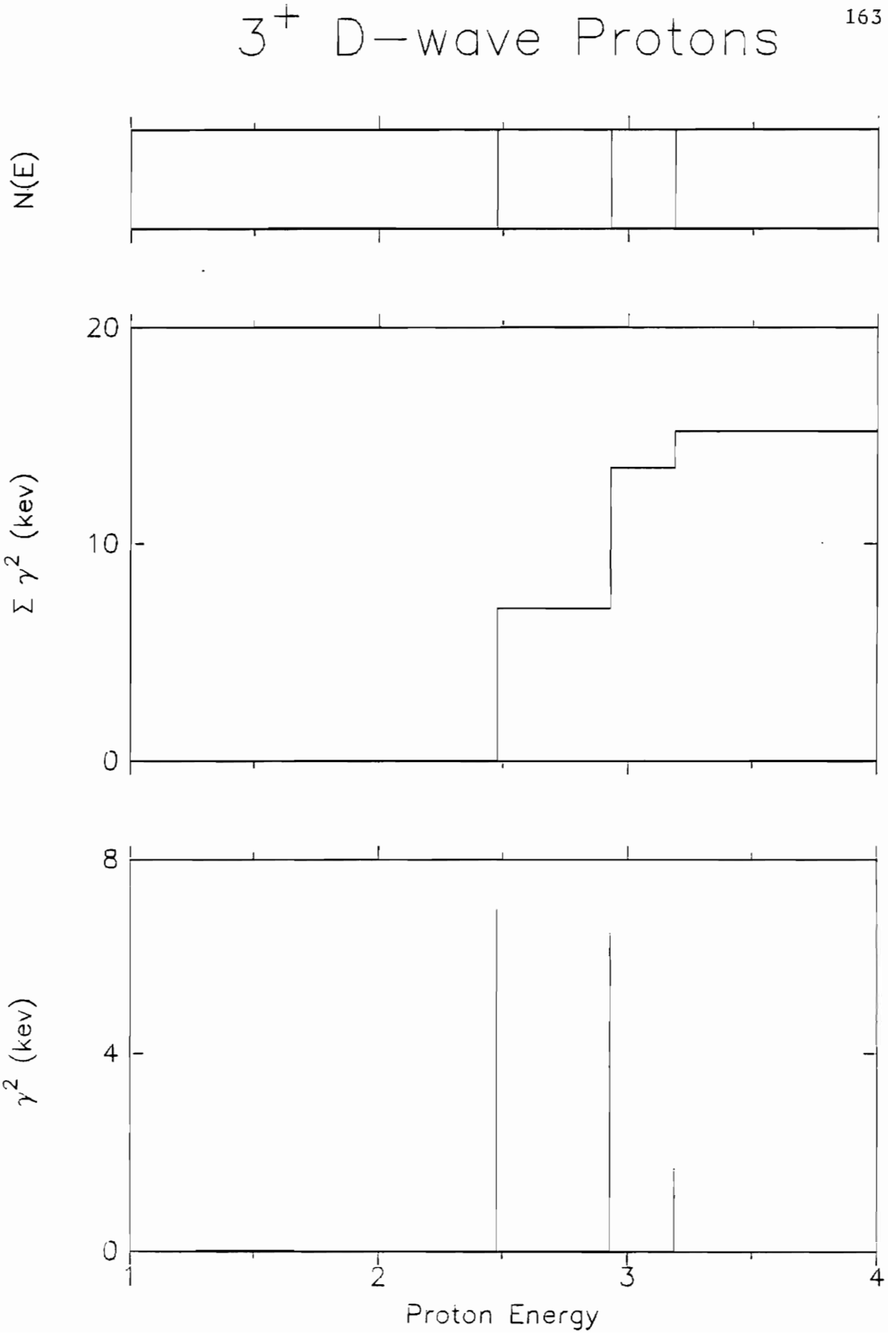
3+ D—wave Protons
N(E)
Σ γ² (kev)
20
10
0
γ² (kev)
8
4
0
1
2
3
4
Proton Energy

Figure 6.21 Proton reduced widths versus energy for $J^{\pi} = 4^{+}$ d-wave resonances.

4^+ D-wave Protons

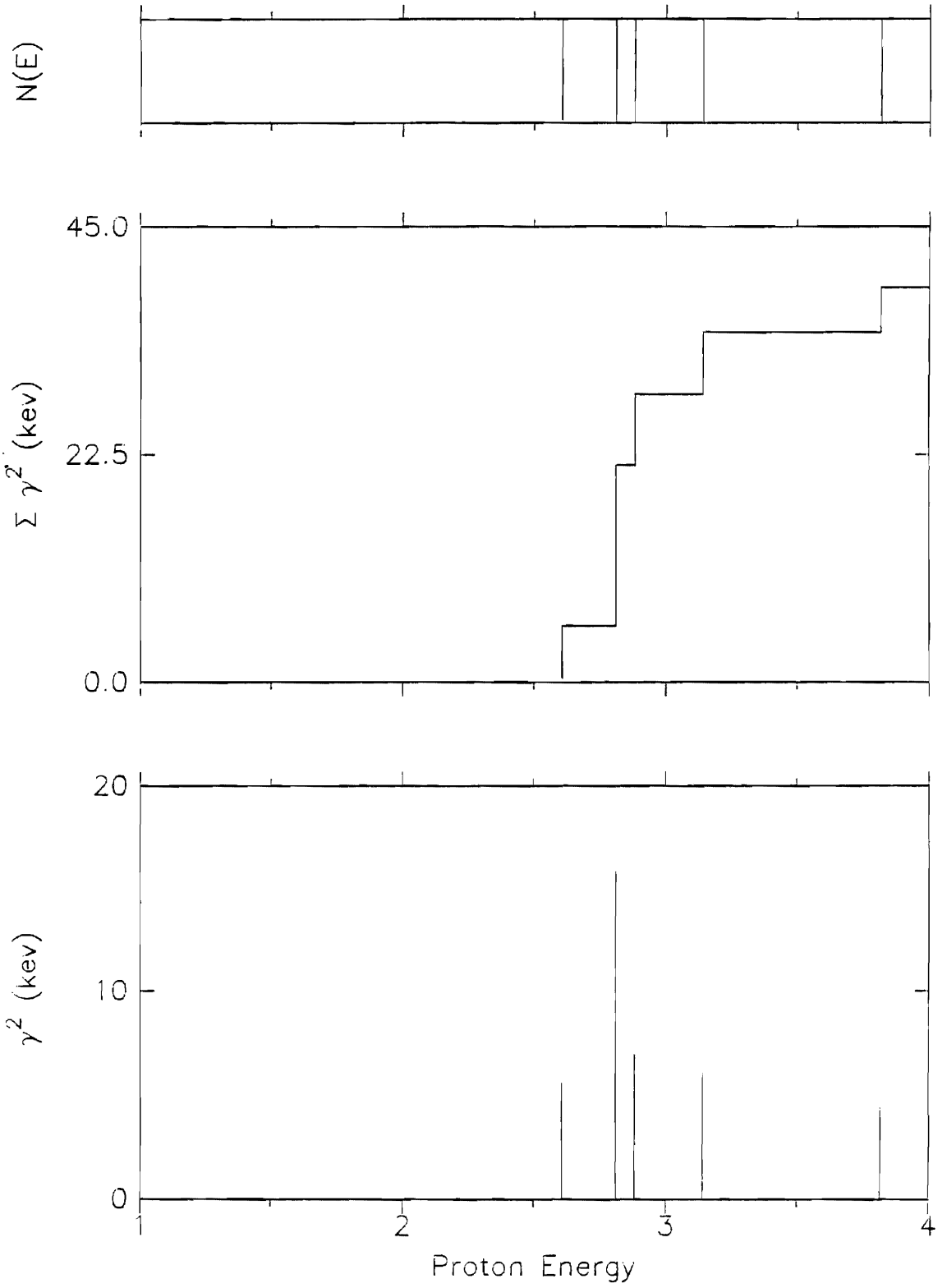

1. Proton Strength

In the proton reduced width plots both channel spins are included for each spin and parity and ℓ value. (The channel spin assignments were often ambiguous, except where there was strong interference.) A measure of the size of the proton reduced widths is the single particle reduced width. This number is taken to be $5/8(\hbar^2/M_c a_c^2)$ (following Bilpuch 1976) which in this case is 950 keV.

A number of the figures merit some comment. Figures 6.8 and 6.9 show the results for 0^- and 0^+ resonances. The number of resonances shown is probably artificially low, however, since J = 0 resonances have little vertical excursion and thus are easier to miss in the cross section.

There were more 1^- states than for any other spin. The largest cumulative width was in the f-wave component of the 1^-, 2^-, and 3^- states. On the other hand, the large f-wave strength for the 1^- resonances arises from many small states, and should be qualitatively correct. Due to the higher ℓ-value the effect on the cross section of adding a small amount of f-wave strength is much less than the effect in the reduced width. Therefore the error in the cumulative sum of reduced widths may be large.

2. Alpha Strengths

The alpha reduced widths are usually much better known than the elastic reduced widths. The laboratory width is usually apparent from the reaction resonance lineshape and the spin is likely to be correct if there is sufficient elastic width to determine the parity. The reduced widths are to be compared to the single particle estimate given above, which for this channel is about 200 keV.

The 0^+ alpha (fig. 6.22) level density is likely to be artificially low due to the difficulty of observing these states in elastic scattering. The 1^- states (fig. 6.23) exhibit two clusters of strength; the lower cluster is in a region where the fit is good, while the upper cluster is in a region where the fit is less reliable.

The 2^+ alpha reduced widths (fig. 6.24) show a cluster of strength near

Figure 6.22 Alpha reduced widths versus energy for $J^{\pi} = 0^{+}$ resonances.

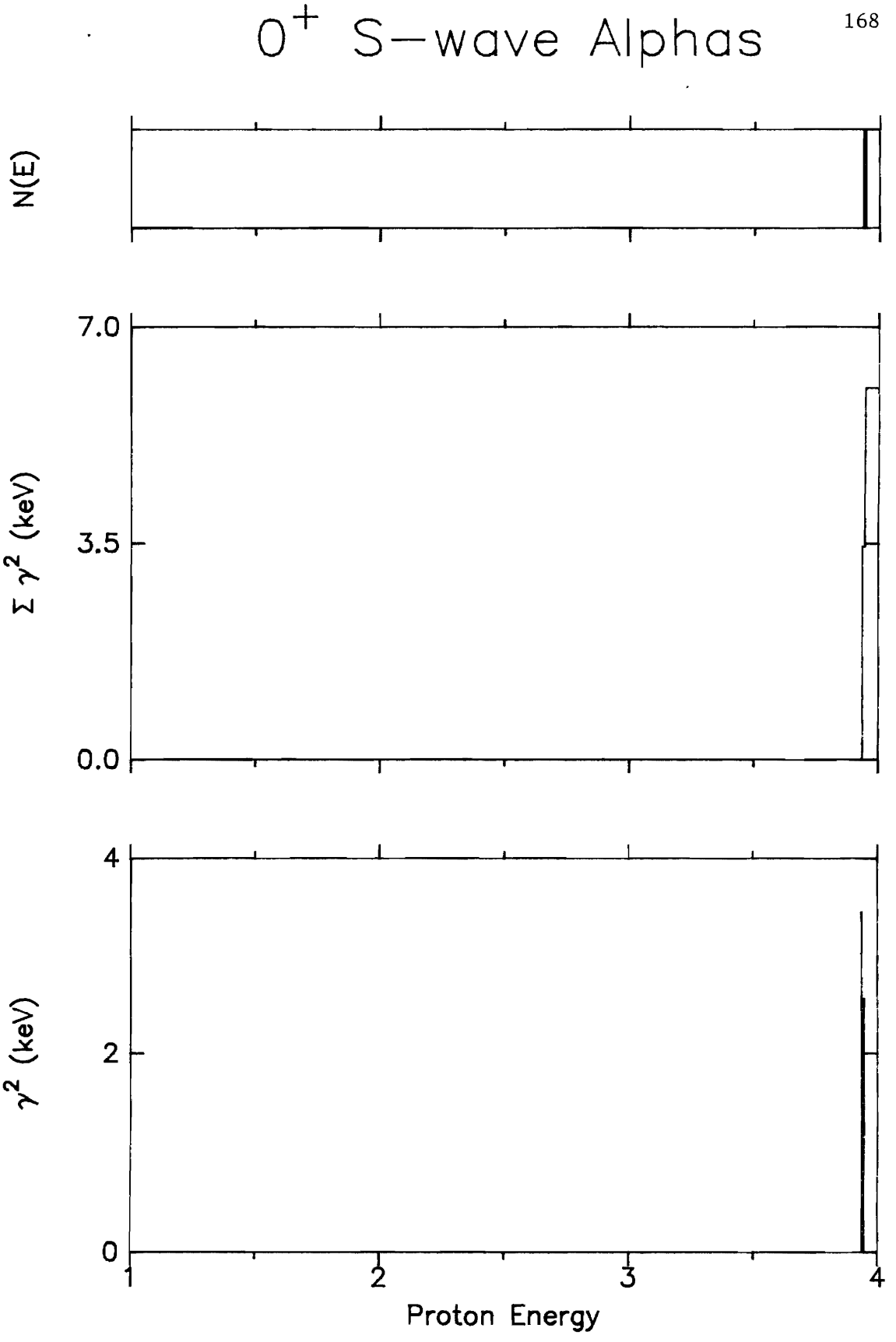
0^+ S−wave Alphas
N(E)
7.0
3.5
0.0
$\Sigma\ \gamma^2$ (keV)
4
2
0
γ^2 (keV)
1
2
3
4
Proton Energy

Figure 6.23 Alpha reduced widths versus energy for $J^{\pi} = 1^-$ p-wave resonances.

1^- P-wave Alphas

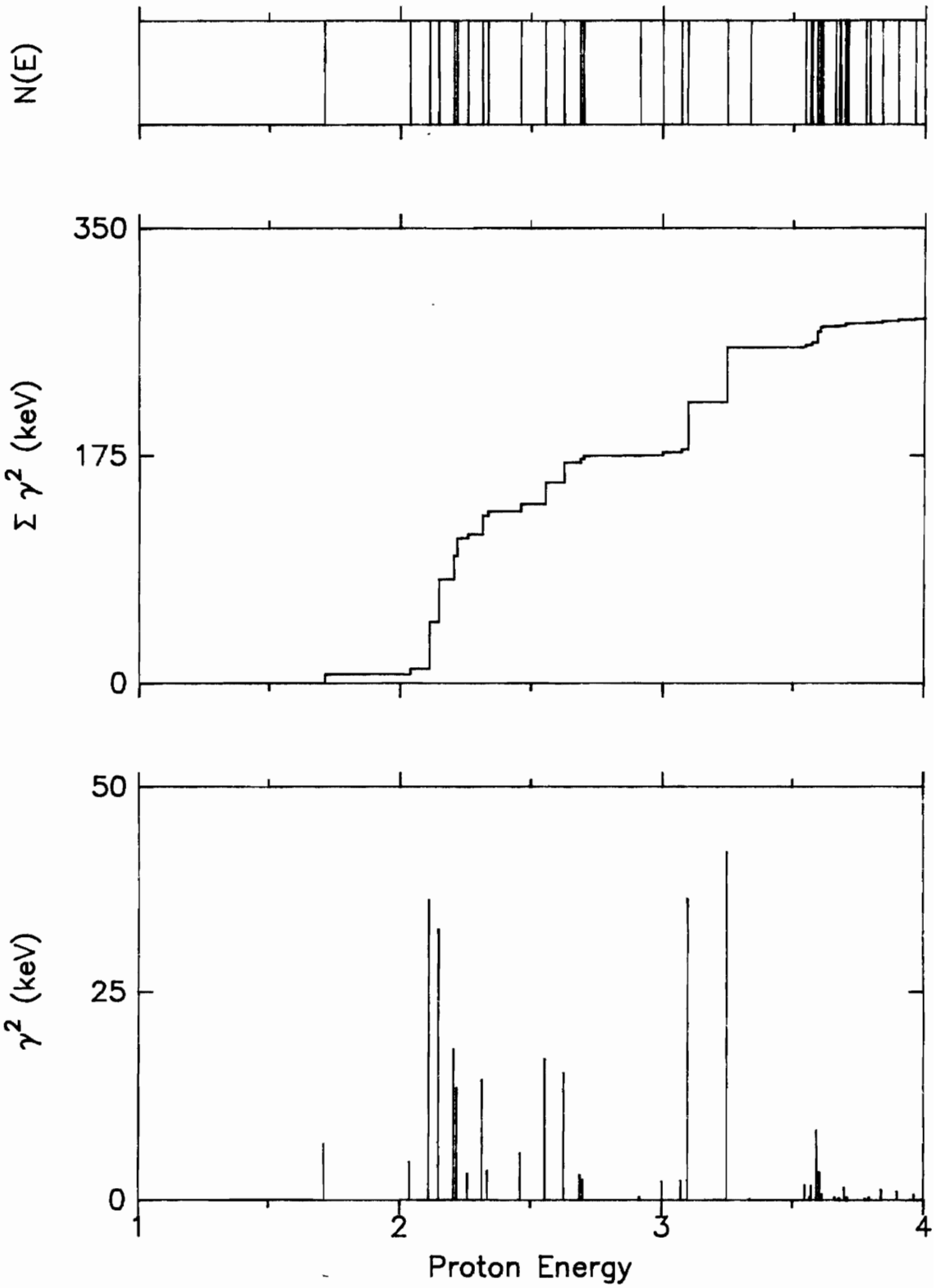

E_p = 2.5 MeV which in total is greater than one-third the single particle width quoted above. In this region the fit in the elastic channel is good and the alpha widths should be reliable.

The 3^- alpha reduced widths (fig. 6.25) include two states larger than 20 keV. The higher energy state near E_p = 3.0 MeV is in a region in which the data are not very well fit. The larger state near E_p = 1.6 MeV should be reliable.

C. Sum Rules

In table 6.1 the number of levels are listed for each channel. The total proton strength is listed as an absolute value and as a percentage of the single particle width. The results are summed over channel spin. Several of the single particle fractions are large, the largest being for the 3^-, $\ell = 1$ states and the 1^-, $\ell = 3$ states. As was noted in section A of this chapter, the results for the $\ell = 1$ strength should be reliable, while the results for the $\ell = 3$ strength are more open to question. In general the s-wave and d-wave strengths are small, while the p-wave strength is much larger. The f-wave strength is very large, but also has a much larger error. The range of resonance energies considered for this evaluation was E_p = 1.20 to 3.18 MeV, the region in which the data were best fitted and the parameters most reliable.

In table 6.2 similar information is listed for the α_0 decay channel. This alpha strength is of special interest because the fraction of single "particle" width for 1^- and 2^+ states is approximately one hundred percent! This estimate takes into account resonances in the same energy range given above. This extimate is conservative, since there is a considerable amount of alpha strength between 3.2 and 4.0 MeV which is not included. These results would tend to suggest an appreciable alpha cluster character in this nucleus at these energies.

D. Astrophysical Reaction Rates

Nuclear astrophysics in recent years has progressed to the stage of

Figure 6.24 Alpha reduced widths versus energy for $J^{\pi} = 2^{+}$ d-wave resonances.

2^+ D—wave Alphas

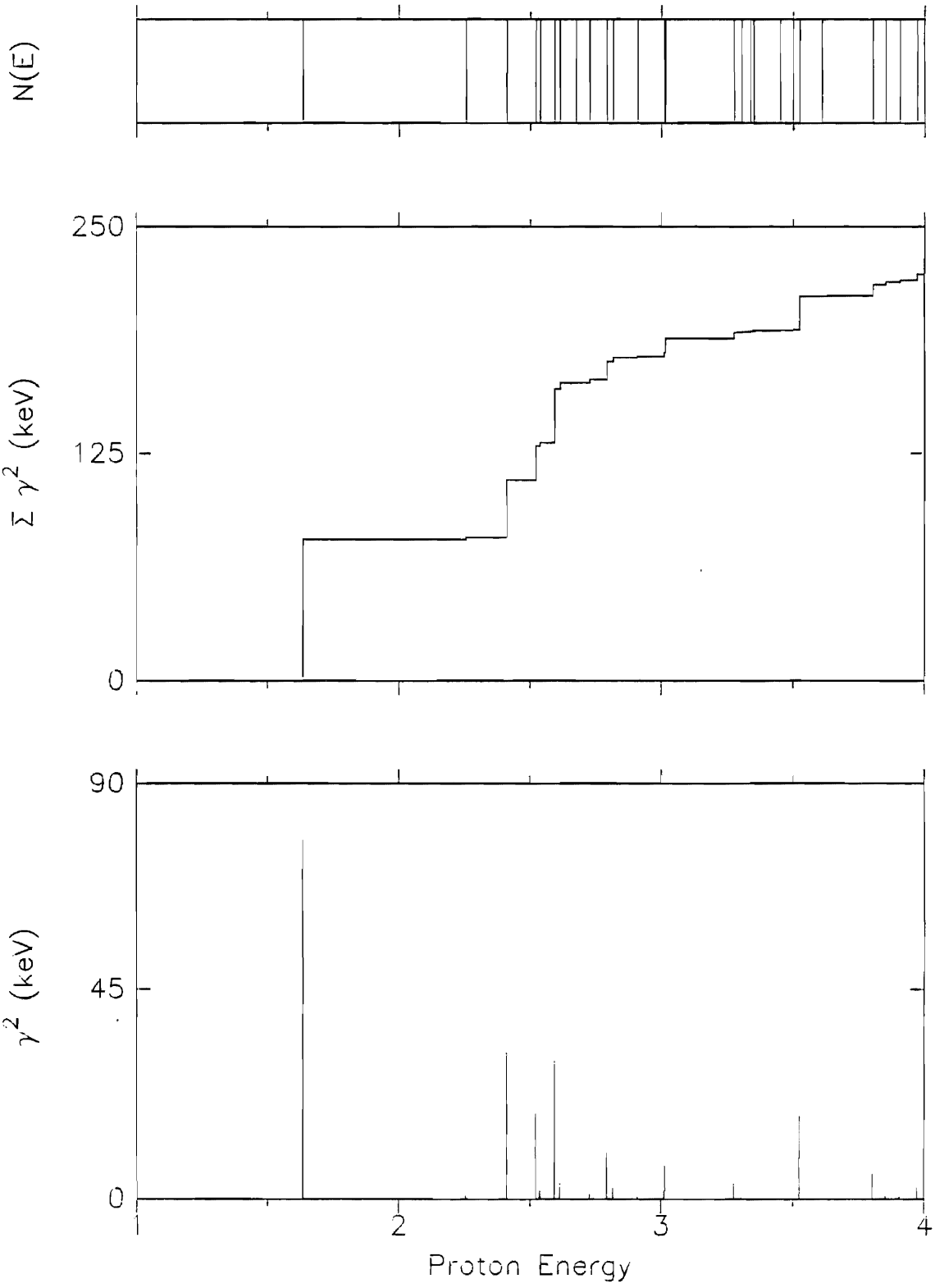

Figure 6.25 Alpha reduced widths versus energy for $J^{\pi} = 3^-$ f-wave resonances.

3^- F-wave Alphas

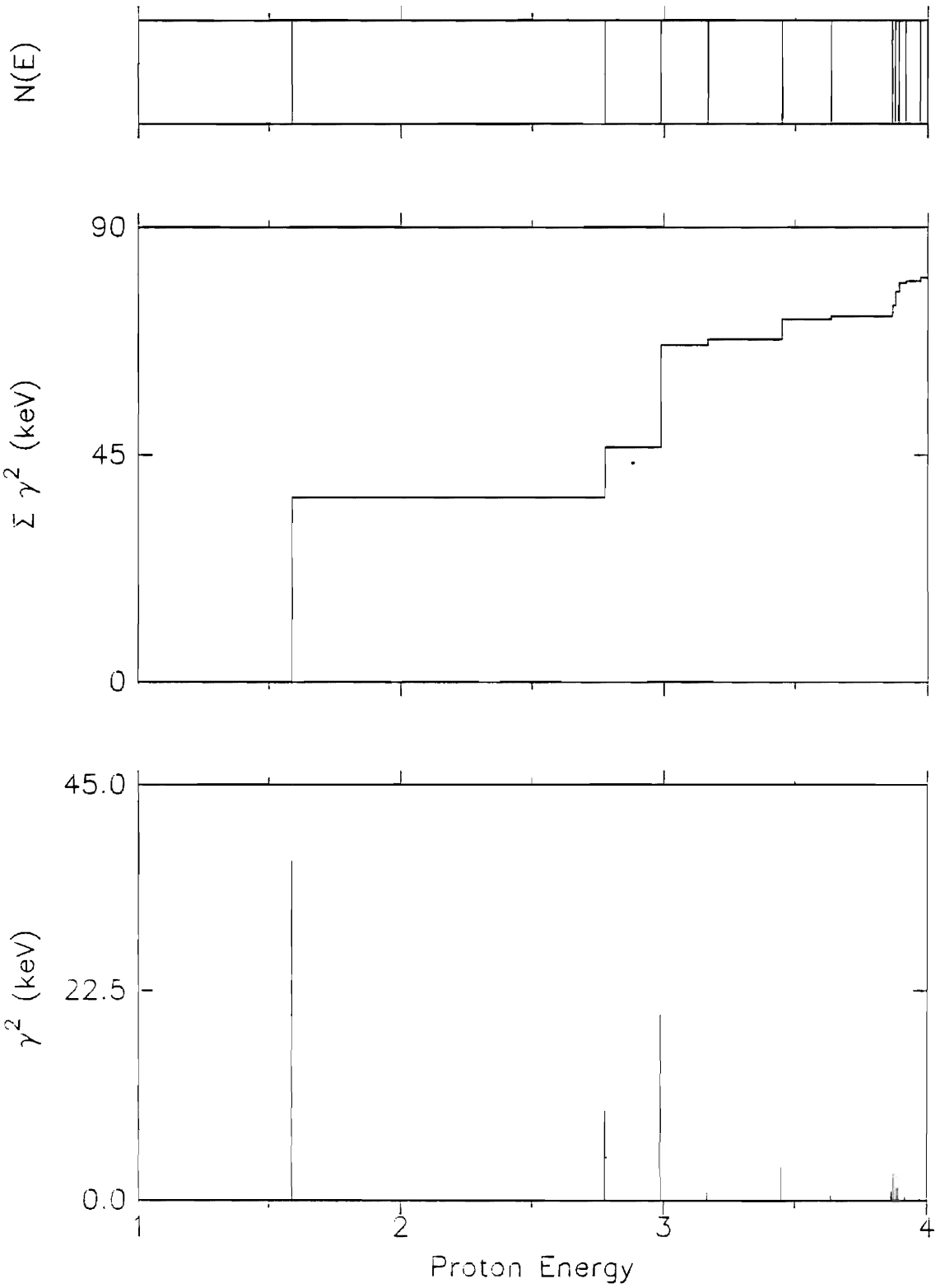

Table 6.1

Proton Strength Observed in ^{36}Ar

J^{π}	ℓ	Number of Levels[a]	Number of Channels[b]	Proton Strength (keV)	Fraction of Single Particle Limit (%)[c]
1^+	0	9	1	9	1.0
2^+	0	13	1	12	1.2
0^-	1	4	1	65	6.8
1^-	1	34	2	524	28
2^-	1	20	2	600	32
3^-	1	10	1	400	43
0^+	2	2	1	25	2.7
1^+	2	6	2	140	7.4
2^+	2	15	2	120	3.1
3^+	2	3	2	15	0.8
4^+	2	4	1	35	3.6
1^-	3	17	1	410	43
2^-	3	10	2	430	23
3^-	3	2	2	57	3.0

[a]All results quoted are for resonances between E_p = 1.20 and 3.18 MeV.
[b]Each row is specified by J, ℓ and summed over channel spin.
[c]The single particle limit is taken here to be 950 keV.

Table 6.2

Alpha Strength Observed in ^{36}Ar

J^{π}	ℓ	Number of Levels[a]	Number of Channels	Alpha Strength (keV)	Fraction of Single Particle Limit (%)[b]
0^+	0	0	1	0	0.0
1^-	1	18	1	220	110
2^+	2	14	1	190	92
3^-	3	4	1	68	33

[a]All results quoted are for resonances between E_p = 1.20 and 3.18 MeV.
[b]The single particle limit is taken here to be 200 keV.

successfully reproducing observed elemental abundances of many of the heavier nuclei in the universe. In the early days of nuclear astrophysics most studies concentrated on the hydrogen and helium burning phases. Following these successes the models have become increasingly more sophisticated and new models have been developed which pertain to presupernova and supernova conditions in stars. These models seek to predict the observed abundances of masses greater than approximately that of oxygen. These conditions are characterized by temperatures in the range of a few billion Kelvin, which corresponds to two-particle center of mass energies of a few MeV. Thus the data measured in this experiment may contribute to the abundance calculations. A recent and useful review article on nucleosynthesis is found in Truran (1984).

The current models of nucleosynthesis are constrained by elemental abundance data from four sources: The solar system, cosmic rays, stars and galaxies, and meteorites. Stellar evolution proceeds through several stages, and in each stage different mass ranges of elements are synthesized. Hydrogen burning, the conversion of hydrogen to helium, occurs in the core of a star for 90% of its active burning lifetime. The conversion occurs through the proton-proton chains and through the CNO cycles, and the key products are ^{4}He and ^{14}N. The second stage of stellar evolution is helium burning, which is dominated by the 3-alpha process and the ensuing $^{12}C(\alpha,\gamma)^{16}O$ reaction. In this phase the stellar temperatures approach 0.2 T_9 ($T_9 = 10^9$ K), and this stage is believed to account for the abundances of ^{12}C and ^{16}O in galactic matter and for the production of neutrons which later become important in the synthesis of elements heavier than iron.

Carbon and oxygen burning constitute the third main stage of stellar evolution. Carbon burning proceeds at temperatures of 0.8 T_9, while oxygen burning requires temperatures of nearly 2 T_9. In this phase there is also a brief intermediate phase of "neon burning," in which photodisintegration of neon releases alpha particles which are subsequently captured by ^{16}O, ^{20}Ne and ^{24}Mg. The primary products of hydrostatic carbon, neon, and oxygen burning are the self-conjugate nuclei ^{20}Ne, ^{24}Mg, and ^{32}S, with lesser amounts of ^{36}Ar and ^{40}Ca. As core contraction increases the central

temperature above $T_9 \sim 3$, the onset of hydrostatic silicon burning occurs.

The stages of explosive burning are categorized in terms of the peak shock temperature to which matter is subjected. For temperatures $T \sim 2T_9$, explosive carbon burning forms many of the nuclei in the mass range $20 < A < 30$. Abundances of mass $28 < A < 44$ are reproduced in explosive oxygen burning ($T \sim 3.6\ T_9$); and explosive silicon burning ($T \sim 4.5\ T_9$) accounts for most of the isotopes in the mass range $48 < A < 62$. (Heavier elements are believed to be synthesized primarily by the r- and s-processes, which are thought to occur in a variety of stellar environments.)

In obtaining abundance predictions from the models mentioned it is necessary to have knowledge of hundreds of nuclear cross sections. While the smaller number of critical reactions are typically well-measured, the many reaction cross sections involving intermediate mass nuclei are not known. In the calculations these are usually approximated by adopting a Hauser-Feshbach (Hauser 1952) or equivalent expression for the energy-averaged cross section. These calculations require knowledge or an estimate of the nuclear level densities and reaction widths for radiative decay and particle emission. It is clearly preferable to have high-quality measurements of these reaction rates when possible.

The astrophysical reaction rate is proportional to the velocity average of the total reaction cross section, assuming a Maxwell-Boltzmann velocity distribution:

$$r(T) = N_1\, N_2 \langle \sigma v \rangle = N_1\, N_2 \int v\, \sigma(v)\, \phi(v,T)\, dv \qquad (6.2)$$

where

$$\phi(v,T) = \left(\frac{M}{2\pi kT} \right)^{3/2} \exp\left(- \frac{Mv^2}{2kT} \right) 4\pi v^2 ,$$

and N_1 and N_2 are the densities of the interacting particles (Clayton 1974). This expression may be transformed into the following form:

$$\langle \sigma v \rangle = \frac{6.1968 \times 10^{-14}}{M^{1/2} T_9^{3/2}} \int E\, \sigma(E)\, \exp\left(\frac{-11605\, E}{T_9} \right) dE \qquad cm^3\ s^{-1} \qquad (6.3)$$

where E is in MeV; this expression may then be used in numerically

integrating over the observed total reaction cross section.

The relevance of the data from this experiment to current research in nuclear astrophysics is primarily to supply measured reaction rates for calculations of explosive carbon burning. The $^{35}Cl(p,\alpha)^{32}S$ reaction rate and the reverse reaction $^{32}S(\alpha,p)^{35}Cl$ are needed. An interesting calculation which requires the forward reaction rate was first performed by Howard (1972). This calculation attempted to reproduce the observed abundances of a number of rare nuclei which are not produced in the main reaction sequences. The model assumes an initial distribution of a small amount of primordial seed nuclei which remains until the onset of explosive carbon burning. During this phase there is an abundance of free neutrons and protons which may interact with the seed nuclei to produce rare nuclei such as ^{36}S, ^{40}Ar, or ^{43}Ca. The initial calculations indicate that this model is a possible explanation of the abundances of many such nuclei. The total (p,α) cross section is shown in figure 6.26. This was calculated using the resonance parameters presented in tables 5.1 and 5.2.

Since charged particle reactions are inhibited at lower energies it is conventional to define a range of "effective energies" by

$$\Delta E_o = 0.237(Z_1^2 Z_2^2 A)^{1/6} T_9^{5/6} \text{ MeV} \qquad (6.4)$$

and a "most effective energy"

$$E_o = 0.122\,(Z_1^2 Z_2^2 A)^{1/3} T_9^{2/3} \text{ MeV} , \qquad (6.5)$$

where A is the reduced atomic weight.

The significance of these quantities may be seen in figure 6.27. The Maxwell-Boltzmann distribution is plotted along with the Gamow factor in the barrier penetration which is proportional to $\exp(-2\pi Z_1 Z_2 e^2/hv)$. The dotted line shows the product of these two functions. The peak of this product occurs at the energy E_o, and ΔE_o is the full width at 1/e times the maximum value. The (p,α) data in this experiment from E_p = 0.6 to 4.0 MeV corresponds to 0.6 T_9 to 11 T_9, with ΔE_o = 0.4 MeV at E_o = 0.6 and ΔE_o = 4.5 MeV at E_o = 4.0 MeV.

The cross section for the inverse reaction may be calculated through

Figure 6.26 Total $^{35}Cl(p,\alpha)^{32}S$ cross section.

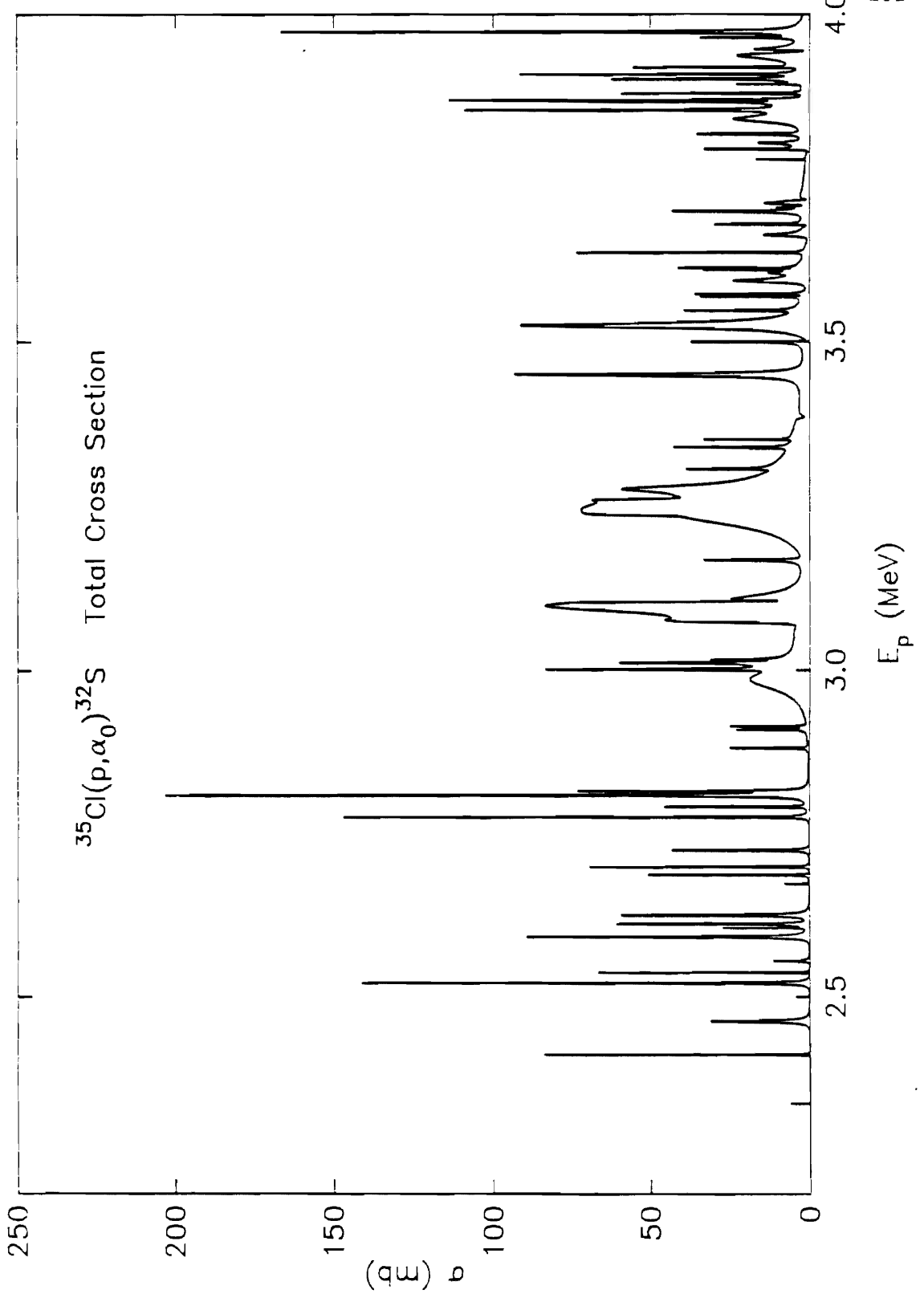
$^{35}Cl(p,\alpha_0)^{32}S$ Total Cross Section
σ (mb)
250
200
150
100
50
0
2.5
3.0
3.5
4.0
E_p (MeV)

Figure 6.27 The effective energies for nuclear astrophysical reactions. The solid curve on the left is the Maxwell-Boltzmann distribution, the solid curve on the right is a term in the barrier penetration, and the dotted curve in the middle is the product of the other two. See text for details.

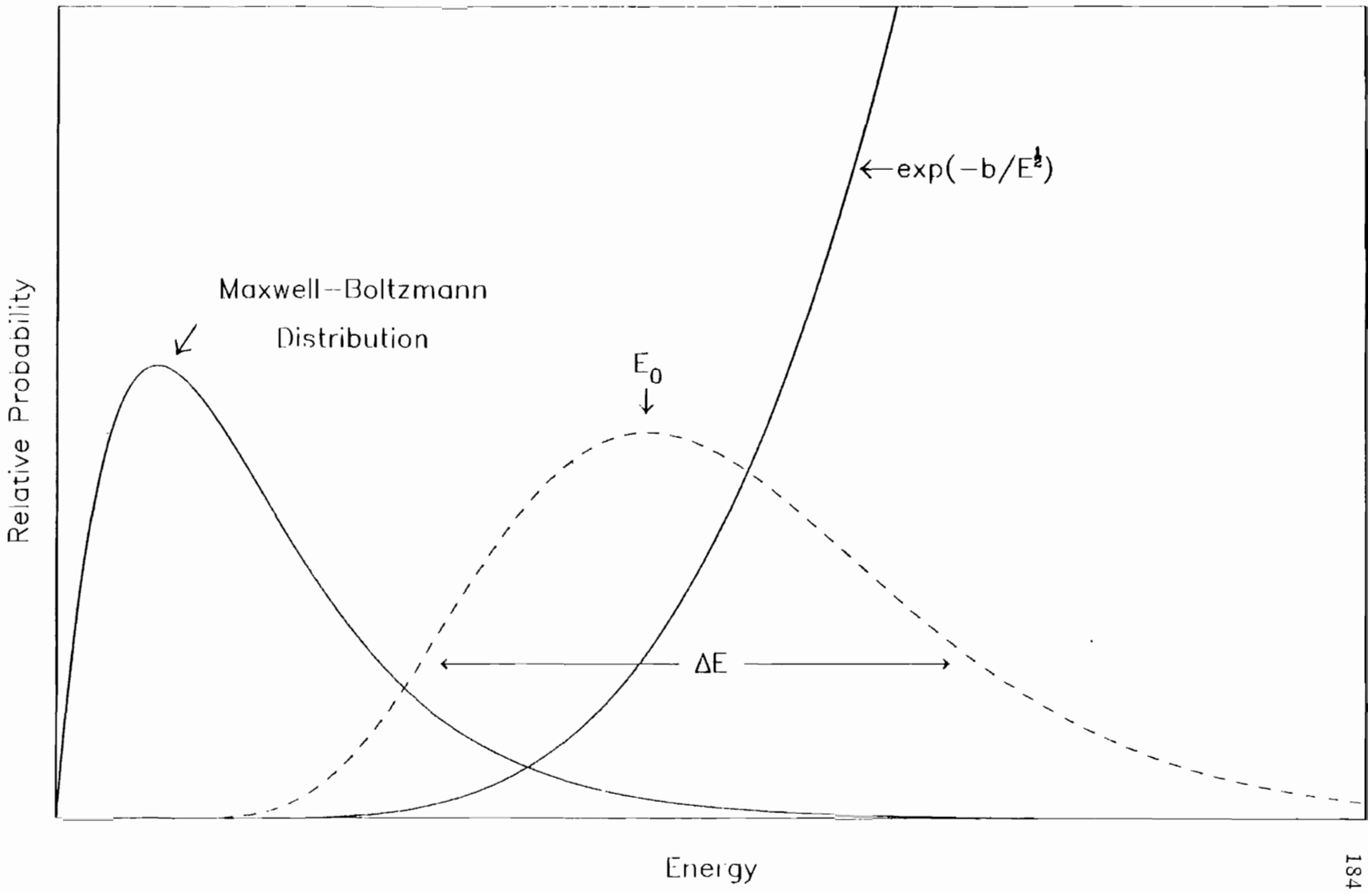
Relative Probability
Maxwell--Boltzmann
Distribution
E_0
$\leftarrow \exp(-b/E^{\frac{1}{2}})$
ΔE
Energy

the detailed balance relationship:

$$(2J_1+1)(2J_2+1)\frac{\sigma(12,34)}{\lambda_{12}^2} = (2J_3+1)(2J_4+1)\frac{\sigma(34,12)}{\lambda_{34}^2}. \qquad (6.6)$$

If only ground states of the reactants are considered, the thermal average $\langle\sigma v\rangle_{12,34}$ may be related to that of the inverse reaction:

$$\langle\sigma v\rangle_{34,12} = \langle\sigma v\rangle_{12,34}\left(\frac{M_{12}}{M_{34}}\right)^{3/2}\frac{(2J_1+1)(2J_2+1)}{(2J_3+1)(2J_4+1)}\exp\left(\frac{Q_{12,34}}{kT}\right) \qquad (6.7)$$

where M is the channel reduced mass.

If the assumption is not valid that only ground state reactants are involved, then a relation similar to equation 6.7 holds but a partition function for each nucleus replaces the spin statistical factors. In this case it is also necessary to know the cross sections for the reaction including excited states in the entrance and exit channels, since the reacting particles in stars have a thermal distribution of energies. A laboratory determination of the *total* reaction rate (including all excited states) is for this reason quite difficult for nuclei having a high density of states. For more details see Clayton (1974).

For the $^{32}S(\alpha,p)^{35}Cl$ reaction the temperatures corresponding to the energies in this experiment range from 1.5 T_9 to 5.5 T_9. A plot of $\langle\sigma v\rangle$ versus temperature is shown in fig 6.28. For the forward reaction $\langle\sigma v\rangle$ was computed numerically using equation 6.3, and $\langle\sigma v\rangle$ for the reverse reaction was computed using equation 6.7.

E. Special States

1) Isobaric Analog States

It is expected that there will be a number of isobaric analog states present in this nucleus at these energies. An introduction to the origin of these states may be found in Vanhoy (1986). An appropriate method for identifying these states is to compare the energies, spins and parities, and spectroscopic factors of states in the parent nucleus (in this case ^{36}Cl) with resonances in ^{36}Ar. The levels in this case are expected to be shifted by

Figure 6.28 <σv> plotted versus temperature. The upper plot is for the forward rate and the lower plot is for the reverse rate.

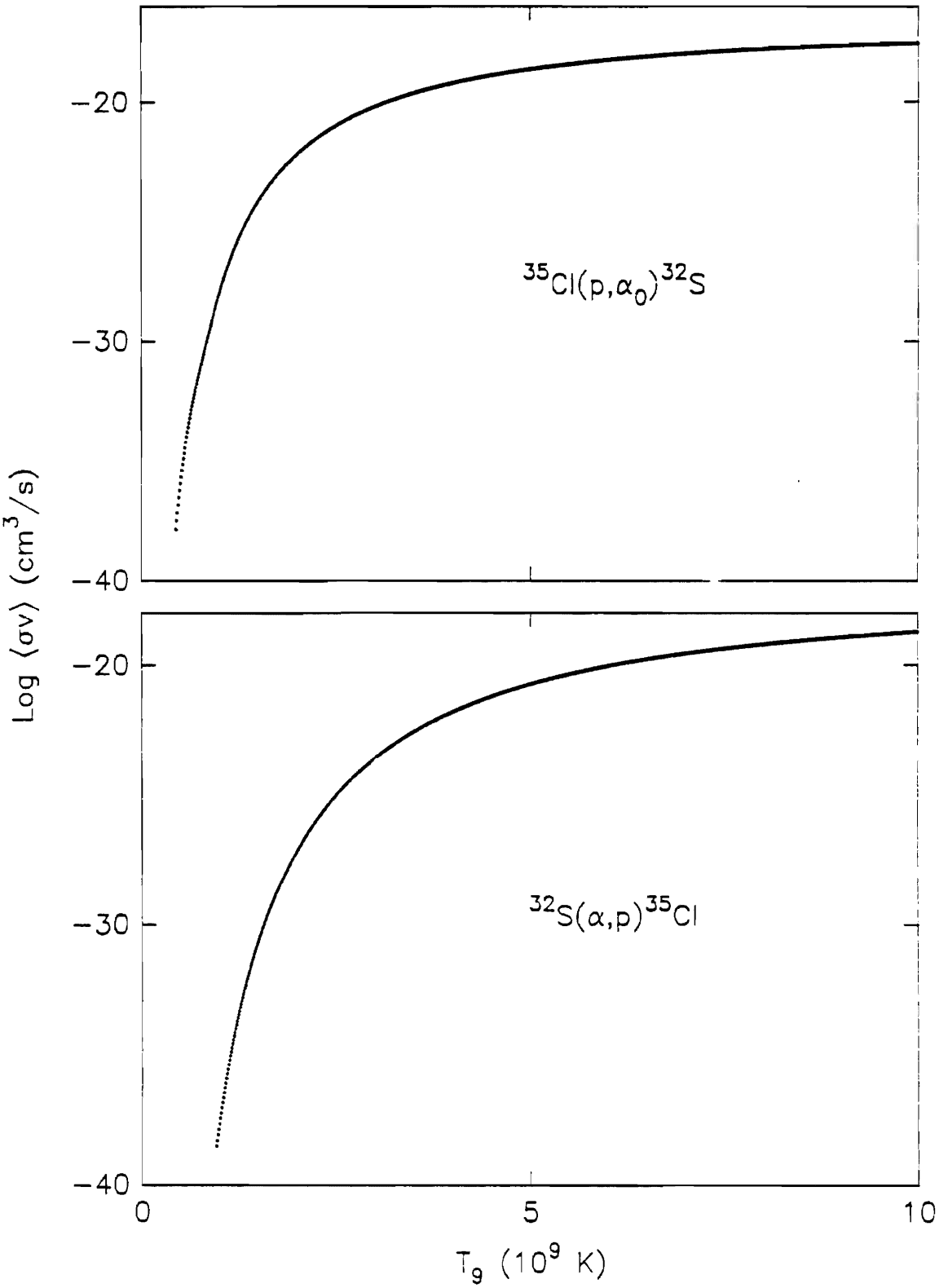
−20
−30
−40
$^{35}Cl(p,\alpha_0)^{32}S$
−20
−30
−40
$^{32}S(\alpha,p)^{35}Cl$
Log ⟨σv⟩ (cm^3/s)
0
5
10
T_9 (10^9 K)

5.389 MeV, using a Coulomb shift (Janecke 1969) of 6.6824 MeV ± 4.8 keV and the neutron-proton mass difference. Unfortunately the levels in ^{36}Cl have not been sufficiently well studied to allow comparison with the resonances in the present experiment. Studies of ^{36}Cl in the pertinent energy ranges may be performed with the ^{35}Cl(d,p)^{36}Cl neutron transfer reaction. Such measurements were done by Paris (1955) and Hoogenboom (1962) but they only assigned level energies and spectroscopic factors; spins and parities of the levels were not assigned. A more complete study was performed by Decowski (1971) in which spins and parities were assigned as well as level energies and spectroscopic factors, but the energies were too low for comparison. For this reason it is not possible to positively identify analog states in this experiment.

2) T = 2 State

The lowest T = 2 state (here T denotes nuclear isospin) occurs in this nucleus in the vicinity of E_x = 10.8 MeV with $J^\pi = 0^+$. Hardy (1969) assigned the resonance energy to be 10.8542 MeV ± 1.0 keV for this level from the (p,t) and (p,^{3}He) reactions. Martin (1976) measured the resonance energy to be 10.8542 MeV ± 1.5 keV using the ^{35}Cl(p,γ) reaction, and Huck (1976) measured the resonance energy as 10.8542 MeV ± 1.6 keV with the same reaction. The average of the two (p,γ) measurements is 10.8519 MeV, which corresponds to proton laboratory energies of approximately 2.413 MeV. Only one resonance observed in this experiment occurred near this energy, at 2.4110 MeV. Although this resonance was tentatively identified as a 2^+ state, this is only a tentative assignment. Essentially no effect was seen in the elastic scattering cross sections; a resonance was seen in the (p,α_o) yield. Further study is required to permit identification of this state as the T = 2 state.

F. Strength Functions

The strength function is defined as the average reduced width divided by the average level spacing ($s = \langle\gamma^2\rangle/D$), and is a measure of the strength

of a reaction over a given energy range. The strength function may be related to specific terms in the optical model potential if there is sufficeint data. Strength function effects related to the isospin term in the optical model potential have been studied by Fang (1987). Similar effects related to the spin-spin and spin-orbit terms are discussed in Fang (1987) and Vanhoy (1986). In the present experiment strength functions have been obtained for a number of reaction channels and will be presented. However, the precision of these values is limited by the small sample size and because analog state resonances cannot be excluded.

The existence of the Bartlett spin-exchange force in the nucleon-nucleon interaction implies a potential term depending on the coupling of the spins of the incident nucleon and target nucleus. Spin-spin forces in the nucleon-nucleus interaction would result in differences for the s-wave strength functions for formulation of resonances with different spins and parities. Previous experiments with charged particles have resulted in the following values for s-wave resonances in 4N type nuclei:

^{24}Mg	(Vanhoy 1986)	$s_{J=1}/s_{J=2} = 0.61$
^{28}Si	(Nelson 1984)	$s_{J=2}/s_{J=3} = 3.5$
^{32}S	(Fang 1987)	$s_{J=0}/s_{J=1} = 0.38$
^{36}Ar	(Present experiment)	$s_{J=1}/s_{J=2} = 0.39$
^{40}Ca	(Warthen 1987)	$s_{J=1}/s_{J=2} = 0.54$

In this experiment the 1^+ (s=1, ℓ =0) strength function was 0.0047 for 12 levels, while that for 2^+ (s=2, ℓ =0) levels was 0.012 for 19 levels.

CHAPTER VII

SUMMARY

Data were obtained for the $^{35}Cl(p,p_0)^{35}Cl$ and the $^{35}Cl(p,\alpha_0)^{32}S$ reactions for the energy range E_p = 0.6 to 4.0 MeV at the laboratory angles θ = 90°, 108°, 135°, 150°, and 165°. The data were fit using a multi-level, multi-channel R-matrix computer code and resonance parameters were extracted for a total of 200 resonances, 140 of which have measurable alpha width. The parameters determined for each resonance are: the resonance energy, the spin and parity, the partial widths, orbital angular momentum mixing angle, and the channel spin mixing ratio. When the resonances strongly overlap, and where there is little alpha strength, the parameters are more ambiguous; for isolated resonances and for resonances with measureable alpha strength the parameters are fairly well determined.

The data were compared with the predictions of standard nuclear statistical models. The distributions of the proton reduced widths in the p-wave channels with s = 2 and J = 1, 2, and 3 agreed well with the Porter-Thomas distribution. For these resonances only about 5% of the levels were missed. In general the qualitative agreement with the Porter-Thomas distribution was good for nearly all channels. Very little s- and d-wave strength was observed, while a large amount of p- and f-wave strength was observed. The largest amount of strength observed was in the p-wave channels.

The strength in the alpha channels was measured to be much larger than that in most of the proton channels. In the 3^- channel the alpha width was approximately one-third of the single particle limit. The strength in the 1^- and 2^+ alpha channels was of the order of a single particle width. These results, which should be quite reliable, indicate a large amount of alpha cluster character in this nucleus at these energies.

No analog states were identified since complementary (d,p) data was not available for comparison. A state was observed in the energy region where

the lowest T = 2 state is expected. Astrophysical reaction rates for the (p,α) and (α,p) reactions were calculated. The strength functions were calculated for s = 1 and s = 2 s-wave resonances and the ratio of the two values was found to be consistent with the ratio in several other 4N type nuclei.

The results presented here suggest more detailed measurements of the alpha angular distributions in order to obtain more precise determinations of the mixing parameters. These values would assist in systematic comparisons with other 4N type nuclei. It would also be of interest to investigate further the large amount of alpha strength in this nucleus at these energies and to compare with the results for other 4N nuclei in this mass region.

Appendix

Targets for High Resolution Charged Particle Spectroscopy

Nuclear targets used for high resolution charged particle spectroscopy must possess three demanding attributes. They must be sufficiently thin, of uniform thickness, and physically and chemically stable under the temperature and vacuum conditions of the measurements. In this section these three requirements will be discussed in detail. Much of what is understood about thin films and the techniques for producing them is empirical. In the following are described some of the methods and results which have been found to be useful in preparing targets for high resolution measurements.

The requirement that the target be thin arises from the need for high resolution in measuring the energy dependence of differential cross sections. Because of the atomic process of slowing of charged particles as they pass through matter, the reaction energies of particles scattered by nuclei are a function of where in the target the scattering occurs. The thickness of the target layer is chosen so that the average energy loss of the charged projectile is much less than the overall system resolution. For example, a 100 eV energy loss for 2 MeV protons passing through aluminum corresponds to a thickness of aluminum of 0.91 $\mu g/cm^2$ (Ziegler 1980). Assuming normal density for aluminum this gives an average depth of 34 angstroms, meaning the target thicknesses are typically of the order of magnitude of 10 to 100 atoms.

Such a thin layer of material will not in general be self-supporting. Over the years it has been found that thin self-supporting foils can be made from aluminum and from carbon, as well as a few other materials. The thinnest foils are made from carbon. It is possible to prepare 10 $\mu g/cm^2$ (~375 angstroms) thick aluminum foils which are self-supporting, while it is possible to make carbon foils of 0.5 $\mu g/cm^2$ (~25 angstroms). (For the latter special precautions must be taken; before lifting the foils they are first coated

with a solution of one part flexible collodian solution dissolved in 9 parts amyl acetate. After drying, the collodian stays on the foil until a charged particle beam strikes it and burns the collodian away. It has been reported that the crystal structure of the carbon lattice (as observed with x-ray crystallography) is modified in these backings; this is not fully understood. Thus this treatment provides more than just physical support for the delicate backings.) Failure of these foils is common, of course; they are very fragile to handle and often have pinholes and cracks.

Since generally targets of 1 $\mu g/cm^2$ cannot be made self-supporting, a compromise is usually struck by using carbon or aluminum backings to support the target material of interest. This has the unfortunate effect of adding a very large peak to the charged particle spectrum, as well as introducing the possibility of other contributions. Many properties of a target backing material must be considered in selecting a backing for a given experiment. Carbon has been used most often in the High Resolution Laboratory at TUNL for many reasons. Backings of 5 - 10 $\mu g/cm^2$ are strong enough to reliably withstand careful handling. The mass and charge of carbon are lower than that of almost all targets of interest; thus the elastic scattering peak due to carbon is well separated from any elastic peaks of interest, and the amount of Rutherford scattering for a given backing thickness is much smaller. Carbon is a conductor, so the backing does not charge and discharge due to the charge deposited by the beam. Since the first excited state in C is at 4.4 MeV, no inelastic proton peaks obscure the spectrum for experiments below that energy; other reaction channel thresholds are even higher. ^{13}C has several reaction channels open at 4 MeV, but all are inhibited by the Coulomb penetrability except the (p,n) channel which has a threshold at 3.23 MeV. Since ^{13}C has only a 1.1 % natural abundance, charged reaction products from ^{13}C usually will not be measurable in the spectrum.

However, there can be disadvantages to using a carbon backing. If the target material happens to react with carbon this may cause problems in performing measurements; an example of this will be described below. There is also an extremely large $^{12}C(p,p_0)$ resonance at about 1.7 MeV which can cause a large increase in the system dead time. This large yield

can also cause pileup peaks in the spectrum in the region of higher energy (p,α_0) peaks, causing a large artificial background problem. The approach taken to circumvent this problem in the past has been to limit the incident beam energy and to use thinner backings in that energy region.

Next consider the uniformity requirement. First assume the ideal conditions of a homogeneous projectile beam and a uniform-thickness target. Then the beam is slowed a known average amount as it passes through the target, and the resolution is degraded by this known quantity. The temperature distribution is smoothly varying and cylindrically symmetric for a circular beam spot.

If the homogeneous beam spot condition is relaxed, the possibility exists for "hot spots" on the target surface. This may lead to problems for targets which have relatively low melting points or high vapor pressures at relatively low temperatures, or where a potential chemical or physical change is strongly temperature dependent. There is no simple solution to this inhomogeneity problem, although "beam wigglers" exist which average out the effect. Since beam optics change as the beam energy increases, any effect of this type will slowly come and go as the energy increases. For long, straight beam paths and tight collimation one could hope it would be a small effect. This problem only threatens the structural integrity of the target but does not degrade the resolution.

If on the other hand one has a homogeneous beam but a non-uniform target, the resolution is worsened and target stability may also be affected. The picture here is that the target material has condensed onto the backing surface in "blobs" instead of a smooth surface. The smaller the agglomerates are, the more uniform the surface. In a rough model where half the surface is empty and half is filled with globules of target material, the average projectile energy loss will be twice as much and the resolution will be adversely affected. When the agglomeration is even greater the resolution will be correspondingly poorer. This problem may be a serious consideration; for instance, aluminum is known to form a completely solid layer on glass only at about 300 angstroms thickness, much thicker than the targets being considered here.

It is possible to predict whether a smooth layer is inherently stable or not based on the latent heats of evaporation (Holland 1966, p.205). Although these numbers may not be available for many materials, the general indication for metals on metals is that agglomeration is favored. The same source (Holland 1966) indicates that the atoms are mobile; at temperatures well below the melting point of the deposited material the deposited atoms will move freely to local minima of the surface force potential.

Information about the degree of granularity of various kinds of materials is available in the literature. As a general rule, at least for metals, the faster the evaporation the less granular the layer formed will be. In the laboratory it is possible to perform simple tests using a charged particle beam. First one counts the number of particles scattered into an angle for a given amount of charge passed through the target, for a given set of beam tuning parameters. Then one can move the target upward physically by putting shim stock under the target rod support, and check the yield again. While a single test like this may not yield useful information a series of tests with varying thicknesses of shim stock may give an indication of granular structure of dimensions of several thousandths of an inch or more, which would indicate a serious problem. This same test can be performed by changing the beam steering slightly and checking the yield. This utilizes the non-homogeneity of the beam to probe the film surface to smaller dimensions than the previous method, although it is not normally a very sensitive test. An intense portion of the beam moved from an empty spot on a target to an especially thick part will produce a rise in the observed yield. This effect has been observed in a number of targets. Another test which can be performed is the measurement of the resolution with a known narrow state in the compound nucleus when the system resolution is known to be good. Both point scatter and the deduced resolution should help to indicate whether a granular target surface problem has occurred.

More exotic tests can be performed for granularity; for example, the conductivity of a thin film of a conductor is an indication of how granular the surface is. Optical tests might be applicable in cases where it is possible to eliminate other factors contributing to optical transparency. Ultimately of

course an electron microscope could be used to look at the surface structure. For most experiments, however, the simple accelerator tests described before are sufficient.

One other possible source of non-uniformity in the targets is the degree of flatness of the carbon backing. Evaporated materials are known to replicate fairly well the surface on which they impinge. In this case one is concerned with the carbon films. Commercially available carbon films are made by depositing carbon onto microscope slides coated with a release agent. The release agent is wiped onto the slides before the deposition is done, and it is often possible to actually see the wipe marks which are made visible by the carbon. Therefore how flat the carbon film is on a microscopic scale may be a legitimate source of concern. Certainly the microscope slide is not ground to optical flatness, and the release agent may or may not constitute a very flat surface on the microscopic level. One might argue that a rough surface will not matter since the target material is evaporated at a 90^{o} angle to the surface and will deposit material to a uniform thickness although at different heights on the target. But the utility of this is lost when the target is turned 25^{o} with respect to the beam line, as is normally done. If the carbon surface is dramatically uneven this may force some of the projectile beam to pass through some thickness of carbon before it hits the target of interest.

The third requirement for a nuclear target is that it be physically and chemically stable. Physical stability means the target material does not melt, sputter off, fall off or diffuse into the target backing as the backing heats up in the beam. These kinds of processes are manifested as either a gradual change or as a sudden change in the elastic scattering yield over time at a single energy (from now on referred to as the "time yield"). The primary physical stress to a backing is thermal, with vibration being another much smaller effect. Although it is unknown what temperatures are reached in the center of the target it is certainly probable that it is in the range of a few hundred degrees C. Because the backing is so thin very little heat is conducted away, and so most of the heat dissipation is radiative. Thus when beam is applied and removed many times to the same target one` may

imagine the stresses to the backing in the center region are large, and contribute to the final failure of the target.

Chemical stability refers to the possibility of a chemical change taking place which lowers the quality of the target. At higher temperatures chemical reaction rates are much enhanced; however even if reactions occur it may not be a serious problem. For instance, if the carbon reacted with the target material just at the interface of the two layers to form a stable material it would have very little effect on the quality of the data. If however some volatile material or gas were formed at the interface it would change the amount of the target present by outgassing and also in the process tend to make the target less stable physically.

One interesting possibility suggested by the problem of chemical instabilities is that with a systematic study one might be able to determine the maximum temperature of the target beam spot as a function of incident beam current. Since melting points and vapor pressures are known for many materials, one could with a judicious choice of lower-melting point materials map out the beam currents required to produce target decay and attempt to correlate the melting points for each material. If a fairly smooth dependence emerged for a number of points using well-chosen materials, one could be reasonably confident in making an estimate of the maximum temperature for a given thickness of carbon, target material, and for a given beam current.

General Procedure for Targetmaking

Typical preparation of nuclear targets for high resolution scattering measurements is as follows. The target material is selected on the basis of a number of factors. Normally isotopically enriched target material is desired, and so the chemical forms of that nuclide which are commercially available must be determined. From the set of possibilities one normally chooses a high melting point compound; for example, in the case of some metals the metal itself is a suitable target material, whereas for others an ionic compound including that metal is required. Any data on target materials from previous experiments is helpful. If the nuclide to be studied is bound in

a compound, one should choose between available compounds so that neither the elastic scattering peaks nor reaction products from other elements in the compound contribute to the spectrum in a way which obscures the peaks of interest.

For example, to study an isotope of chlorine one might choose barium perchlorate ($Ba(ClO_4)_2$) over sodium chloride (NaCl). In the former the barium and oxygen elastic peaks are well separated from the chlorine peaks and do not add any other reaction products to the spectrum, whereas in the latter the sodium elastic peak is fairly close to that of chlorine and natural sodium has a number of open reaction channels which will add more peaks in the spectrum. Kinematic caluclations can determine whether any peaks will overlap in the energy range of interest, but the experiment is generally simpler if no unnecessary peaks occur in the spectrum. One final consideration for compound target materials is minimizing the amount of beam energy loss per given thickness of the nuclide of interest. Because of additional elements present in a compound one target material may be significantly better than another in this respect. For instance, for a given thickness of chlorine one can calculate that the average energy loss in barium chloride ($BaCl_2$) is less than that in silver chloride (AgCl). This allows the use of thicker targets for a given energy loss, which makes it possible in many cases to increase the data acquisition rate.

After the target material has been selected the carbon backings can be prepared. This is done by floating carbon foils onto stainless steel target support rings and allowing them to dry. Whenever possible these foils should be flat, free of wrinkles, cracks and pinholes. The backings are then placed in a holder in a vacuum bell jar and the material of interest is evaporated onto them. This is typically done by placing the target material in a specially made "boat" made of tantalum, tungsten, or other materials. Only boats of a certain fabrication are appropriate for a given material, and problems may easily arise. For instance, it is difficult to evaporate nickel from a metal boat because nickel forms a low melting point eutectic with the boat, which immediately melts in half. Thus one uses a metal boat coated

with aluminum oxide instead. Information on appropriate boats and filaments for many materials is available.

The distance between the boat and the backings chosen is dependent on several factors. The greater the distance, the more uniformly thick the layer deposited is; thus one often makes this distance as large as possible. In special cases there may only be a small amount of isotope available and so the distance may need to be smaller. This is also true sometimes when the target material is difficult to evaporate or doesn't adhere well to the carbon backings; this has been observed for zinc and magnesium, for example. Sometimes the backings need to be protected from the heat of the boat by a shield with a hole in the center. This has been true of materials with extremely high melting points where the radiant heat from the brightly glowing boat can damage the carbon foils. The backs of the foils should be covered with microscope slides to prevent material from being deposited on the back side of the foils. This surprising effect has been observed a number of times.

For greater control of evaporation a movable shield is often placed between the boat and the backings. When the desired deposition rate is indicated by the thickness monitor the shield can be moved away; then when the desired thickness is reached it can be replaced. This is the optimum procedure when possible; it is preferred because some properties of the films depend on deposition rate, so it is helpful to be able to control the rate. Also, being able to cut off the deposition suddenly is necessary for producing more precise film thicknesses; when the evaporation process is terminated by simply turning down the heating current, the evaporation often continues for several seconds, while decreasing gradually.

Most target materials can be melted and evaporated by passing current through one kind of boat or another; for materials which have the highest melting points or which react with the hot boat, however, an alternative method is to use an electron gun. This is a simple device which produces a focused beam of electrons which in striking the target material heats the surface until it melts. Because modern electron guns are controllable and a clean means of heating a surface, this method is used very commonly by professional targetmakers for most physical vapor deposition. The use of a

liquid nitrogen trap during the evaporation helps to reduce the amount of contaminants in any evaporation; outgassing the boat by heating it also helps to reduce contamination; a thoroughly clean bell jar and vacuum system are also significant in reducing unwanted elements from being deposited in small quantities on the backing.

Once the material has been deposited and allowed to cool the backings can be removed from the bell jar and tested. Normally they are let up to dry nitrogen gas, since many materials of interest will either oxidize or absorb water. The targets can be protected somewhat from this by transporting them in a plastic bag of dry nitrogen, but a facility for doing this which is both simple and thorough does not presently exist at this laboratory.

Appropriate procedures for testing targets depend to some extent on the target. A basic test is to take a time yield over 15 to 30 minutes time, to look for target decay and check for excessive point scatter. This must of course be done when the system energy is known to be stable. Point scatter can indicate problems with the target, but can also indicate problems in the energy correction system, and when stepping in energy often indicates background subtraction variations. Therefore care must be used in interpreting this effect; but in favorable cases the point scatter has been seen to be within 10% of counting statistics.

Other tests include measuring a long term spectrum to look for small contaminant peaks; from this one could estimate upper limits to levels of contamination of elements near the nuclide of interest in the spectrum. One also can obtain a long term spectrum of a carbon foil without the target material on it but which has gone through all the other phases of preparation which the targets have. This would detect contaminants which would occur under the peak of interest. If one particular contaminant is suspected these tests would be enhanced at an energy where there is a known resonance in the contaminant. Further diagnostics include measuring time yields for other peaks in the spectrum. This helps to provide clues to what is happening to the target surface during bombardment. For instance, if one calculates the ratio of silicon to oxygen on a target prepared by quickly evaporating silicon dioxide (SiO_2) onto a backing it will typically be found that (after Coulomb

effects, resonance effects, and oxygen contamination are taken into account) the ratio of silicon to oxygen is non-stoichiometric and depends on the evaporation rate. What ends up on the backing is a mixture of silicon metal and silicon oxides, which is a well known effect. If there is a problem with target decay one can measure the yields of all the other materials on the target to attempt to correlate the amount that disappears with changing yields of the other material; for example if it were suspected that the carbon was combining with the target material to produce a gas one would expect a stoichiometrically consistent decrease in the carbon yield as the target decays. Another example is monitoring the oxygen time yield. A decrease might indicate that water of hydration is being removed if the target material is a hydrated ionic crystal. For some hydrated crystals this disrupts the physical structure; for example, it is known that removal of water from the crystal lattice of $BaCl_2 \cdot 2H_2O$ destroys the lattice. Clues like this can be helpful in diagnosing target problems.

An approach taken by a number of people is to evaporate a thin layer of another material on the carbon backing before depositing the target material. This has been done for several reasons. Some materials do not adhere well to carbon; zinc phosphide and magnesium have already been mentioned. Sometimes the target material will adhere better to a thin layer of another material, such as gold or nickel. In other cases experimenters have used gold in this way to give excellent normalizations for their data, since for such a heavy nucleus at low energies the scattering is purely Rutherford. This technique is simple and useful when the evaporation of the material used produces a uniform layer and the material does not contribute reaction products to the spectrum.

One interesting test which could be performed for a particular target material is to actually measure the average energy loss of a charged particle beam passing through that material. It has occasionally been seen that a target which was thought to be too thick has produced good resolution. This would indicate that the energy loss estimates might be low; the tables given by Ziegler (1980) are for much thicker layers than are considered here, and it may be that those calculations are not as accurate for the limiting case of a few tens of atoms as has been assumed. A rough measurement of the

energy loss in a given material could be obtained by measuring the change in location of a resonance peak after a particle beam has passed through a layer of the material of interest. For example, in measuring the energy loss of protons passing through zinc phosphide, one could apply a layer of zinc phosphide over a layer of aluminum on a carbon backing for one target, and apply a layer of aluminum over a layer of zinc phosphide on a carbon backing for another target. The energy shift of a narrow resonance in aluminum between the two targets would give the average energy loss due to the zinc phosphide; the temperature of the target should be the same since the thickness and makeup of both targets are the same, so the Doppler broadening effect should be identical for each. It might be informative to study such an effect in detail using materials whose evaporation properties are known.

Approaches Taken for Chlorine Targets

The procedure just given did not work satisfactorily for the targets used in the ^{36}Ar measurement. The target material $BaCl_2$ was chosen for several reasons. Commercially available ^{35}Cl comes in the forms NaCl, KCl, AgCl, $PbCl_2$, $BaCl_2$, Cl_2(gas). The first two were eliminated because of reaction products due to Na and K and because the elastic peaks were close to that for ^{35}Cl. AgCl and $PbCl_2$ had melting points of 455^{o} C and 500^{o} C respectively, which were low compared to that of $BaCl_2$ which is 963^{o} C. For a given thickness of chlorine the energy loss of a proton was less through $BaCl_2$ than for AgCl and $PbCl_2$; $BaCl_2$ had also been used in previous experiments. So $BaCl_2$ was chosen to be the target material.

It was found, however, that this target material underwent chemical decay in the intense proton beam. As a consequence, other target compounds were tried. Chlorine occurs in many organic compounds, but these are invariably ruled out by low melting points and volatility. This leaves only ionic compounds to try, due to the halide nature of chlorine. Targets were made using yttrium chloride and silver chloride, these being chosen because it was possible to simply convert $BaCl_2$ to these forms chemically. These targets decayed also, and the time yields of chlorine

which exhibited the decay in both cases were identical in shape to that of $BaCl_2$. This indicated that the decay was due to the ionic nature of chlorine in these compounds, suggesting that no ionic compound would be any better than $BaCl_2$, and that another approach was needed. The decay process clearly involved the carbon as well, since all of those compounds are chemically stable at several hundred degrees C. For the chlorine to disappear from the target, the chlorine had to be in the form of a gas (Cl_2) or volatile liquid (e. g. carbon tetrachloride - CCl_4), since the barium yield showed little change while the chlorine decreased rapidly.

With this in mind it was attempted to find a material which could be evaporated onto the carbon first to chemically "insulate" it from the final layer of $BaCl_2$. The materials chosen for these tests were ones which formed high melting point chlorides, so that even if the material reacted with the barium chloride it would still stay on the target. This procedure was tried with nickel, lanthanum, barium nitrate, gold, tungsten, tantalum, and silver. The decay was slower in all cases than before, but was still there. Nickel gave the best results of all those tried, and was used to take data with in the early experimental runs with $BaCl_2$ on nickel-coated carbon backings.

Further Attempts

In the course of attempting to measure data with the above-described targets a number of further approaches were tried to limit target decay. These approaches included using lower beam currents on the targets, experimenting with different proton beam tunings, and placing shims under the target rod positioning stop to move the beam spot to a different part of the target surface. While the first two approaches were not effective, it was noticed that better results were obtained by slightly repositioning the beam spot on a target which had already been in the beam for some time. Such a procedure produced targets exhibiting a nearly stable time yield. This was a clue that perhaps heating these targets might make them more stable. In response it was attempted to "pre-condition" the targets using a low-energy electron beam. This produced stable targets which were however very thin in chlorine and in which the ratio of barium to chlorine was quite non-

stoichiometric. The next technique tried involved heating the nickel-coated carbon backings first, before applying the layer of $BaCl_2$. This produced targets which were stable and which had a ratio of barium to chlorine which was very closely 1:2 (Coulomb effects have been divided out). These constituted the final targets for the experiment.

Description of the Method

Several carbon foils (produced by carbon arc) of 5 $\mu g/cm^2$ thickness were floated onto stainless steel target support rings of inner diameter 7 mm and outer diameter 19 mm. These were then placed under vacuum and nickel metal was evaporated onto them. The vacuum level was in the range 0.5 to 2 μtorr, and the thickness of the nickel layers was 1.0 to 1.5 $\mu g/cm^2$ as measured by a Maxtek TM-100 deposition thickness monitor. For this evaporation nickel powder was placed in an aluminum oxide coated tantalum open boat 0.25 mm thick which was mounted about 25 cm beneath the target rings. The boat was heated by passing 180 A of alternating current through it for about 1 minute in order to melt the nickel (m. p. 1455^{o} C) and deposit the required thickness onto the carbon backings at a measured rate of about 0.03 $\mu g/(cm^2\ s)$. After cooling, the foils were removed from the vacuum and heated individually.

The heating of the foils was accomplished by passing a high-current, low-energy electron beam through the backing under vacuum. The apparatus is depicted schematically in fig. A.1. A circular filament of 0.05 mm thick tantalum wire with a diameter of 1.8 cm was mounted 3 mm above the target ring. The ring itself was positioned with the nickel-coated side facing the filament above and was supported from beneath by a small hollow cylinder of carbon resting on a rubber ring to electrically isolate the stainless steel ring and carbon cylinder. Beneath the center of the foil was a rounded copper electrode. The electrode was approximately 5 mm thick and located 3 mm beneath the surface of the carbon film and was mounted in a water-cooled copper heat sink. The entire assembly was put under 10^{-4} torr of vacuum.

Figure A.1 Experimental apparatus for heating foils.

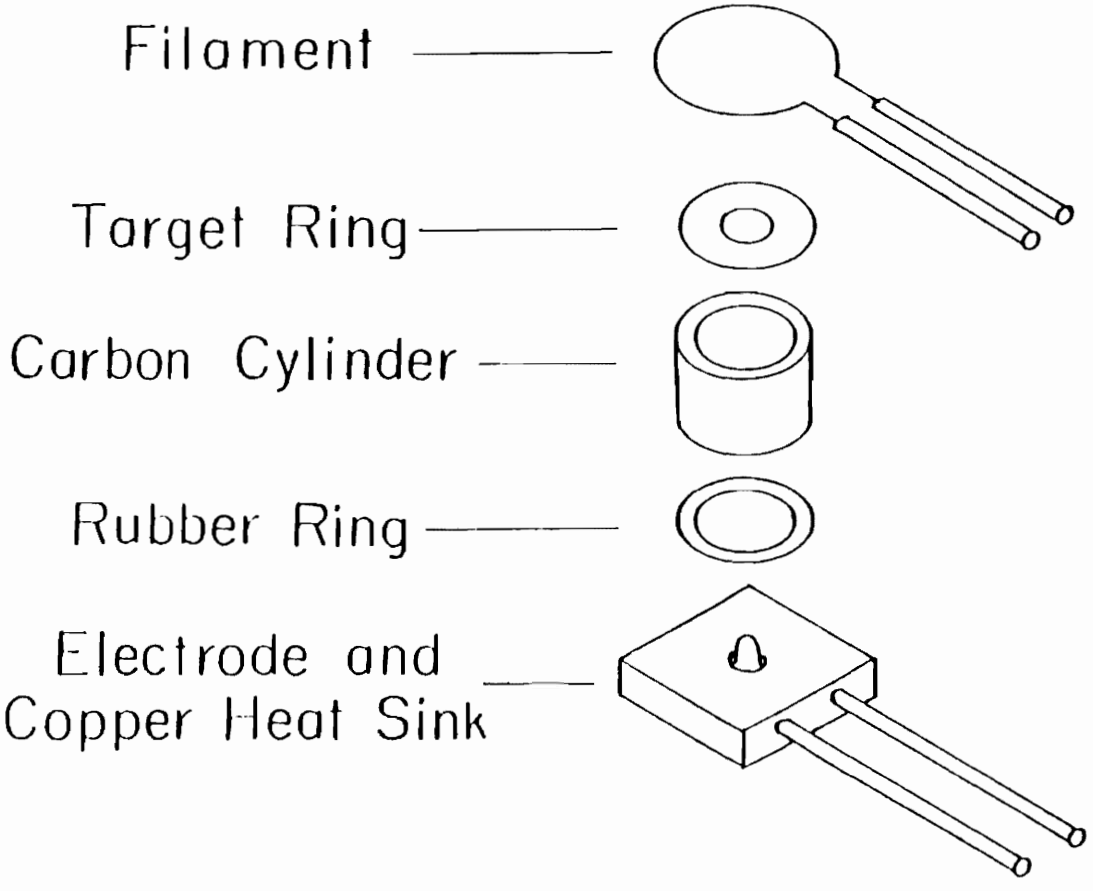
Filament
Target Ring
Carbon Cylinder
Rubber Ring
Electrode and
Copper Heat Sink

The electron beam was produced by first passing 12 - 15 A of alternating current through the filament to heat it and then biasing the filament at - 1000 V dc with respect to the grounded copper electrode beneath the target. The electron beam produced in this manner was typically 40 mA. Each foil was heated by passing the beam of electrons through the center region for about one minute. A circular spot 2 mm in diameter in the center of the foil was observed to emit a dull orange glow, probably indicating temperatures in excess of 700° C. Because of the brightly glowing filament directly above the backing, it was difficult to measure the temperature with an optical pyrometer or similar device. As a result of several tests it appeared that neither the time of heating, current and energy of the electron nor exact apparatus dimensions were critical.

After each foil was heated separately in this way, they were all placed under vacuum again and a layer of barium chloride 1 - 2 $\mu g/cm^2$ in thickness was evaporated onto them at 1 μtorr. For this evaporation, about 25 mg of barium chloride (isotopically enriched to 99.35% ^{35}Cl) was placed in a 0.013 mm thick tungsten open boat mounted about 25 cm beneath the targets. About 50 A of alternating current were sufficient to melt the compound (m. p. 963° C) after it was first gently heated to drive away the water of hydration. The evaporation took place over a period of about 3 min at a measured rate of about 0.004 - 0.008 $\mu g/(cm^2\ s)$. After cooling, the final targets were removed and tested in a proton beam.

The decay exhibited by the original targets of barium chloride on carbon backings was of a fairly reproducible shape, although the extent of the decay varied; typically the yield would drop to 25 - 35 % of its initial value in one hour. At a given incident current and energy, the elastic scattering yield over time resembled the general shape of a decaying exponential (see fig A.2). The point scatter in most targets was seen to be significantly greater than that due to counting statistics, and irregular jumps in the chlorine time yield occurred occasionally. These observations were made with bombarding proton beam currents of 1.5 - 6.0 μA at energies of 1 - 4 MeV. The largest amount of decay would occur in the first few minutes of bombardment, and in these targets the rate of decay would continue to

diminish but never reach zero as time went on. The barium decay was measured to be less than 10% of the chlorine decay over a given period of time. Targets made by evaporating a layer of nickel on the carbon before depositing the barium chloride were observed to decay to a lesser extent and often come to an equilibrium thickness of chlorine after a period of time varying from 1 to 6 hours. These targets were also observed to be somewhat fragile after being conditioned in this way.

The targets produced using the previously described process of "baking" the nickel-carbon backings in several tests showed no measurable amount of decay over a period of more than an hour. The amount of point scatter in these targets was generally observed to be relatively small; in the test shown in fig. A.2, the observed standard deviation was only about 8% greater than that expected from counting statistics, as compared to a factor of two or three for the earlier targets. They also appeared to be much stronger than the previously tested ones, lasting in one instance over 90 hours while being bombarded with 2 - 4 μA of proton beam at 3.5 - 4.0 MeV. (It is not generally recommended that targets even be used that long in the beam since a layer of carbon usually will get sputtered onto the target surface due to residual pump oils in the system, degrading the resolution.) The surface of the foils acquired a gold-colored tint after being heated, and changed from being flat to being slightly dome-shaped, with the apex of the dome being about 1 mm above the plane of the target ring. They also seemed more rigid after being heated. Targets for some of the experimental data were fabricated using a slightly different geometry than that which has been described. These targets were seen to decay a small amount over several hundred kilovolts range. The range of data for E_p = 1.8 to 2.2 MeV showed this effect. The problem involved was probably due to insufficient heating of the Ni-C backing, since no heated spot was observed on the backing surface as had been true using the geometry described.

Conclusions

Without extensive testing using special technologies it is impossible to unambiguously determine the processes occurring which account for the

Figure A.2 Time yields for decaying target and for stable target.

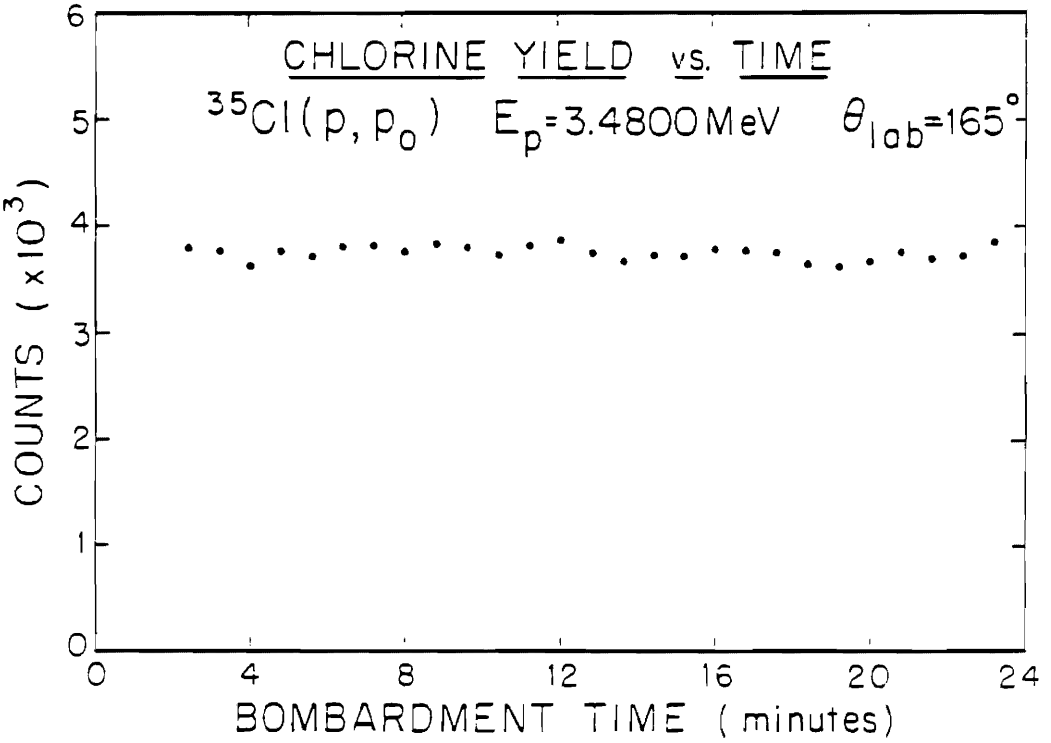
CHLORINE YIELD vs. TIME
$^{35}Cl(p,p_0)$ E_p=3.4800MeV θ_{lab}=165°
COUNTS (x10^3)
0
1
2
3
4
5
6
0
4
8
12
16
20
24
BOMBARDMENT TIME (minutes)

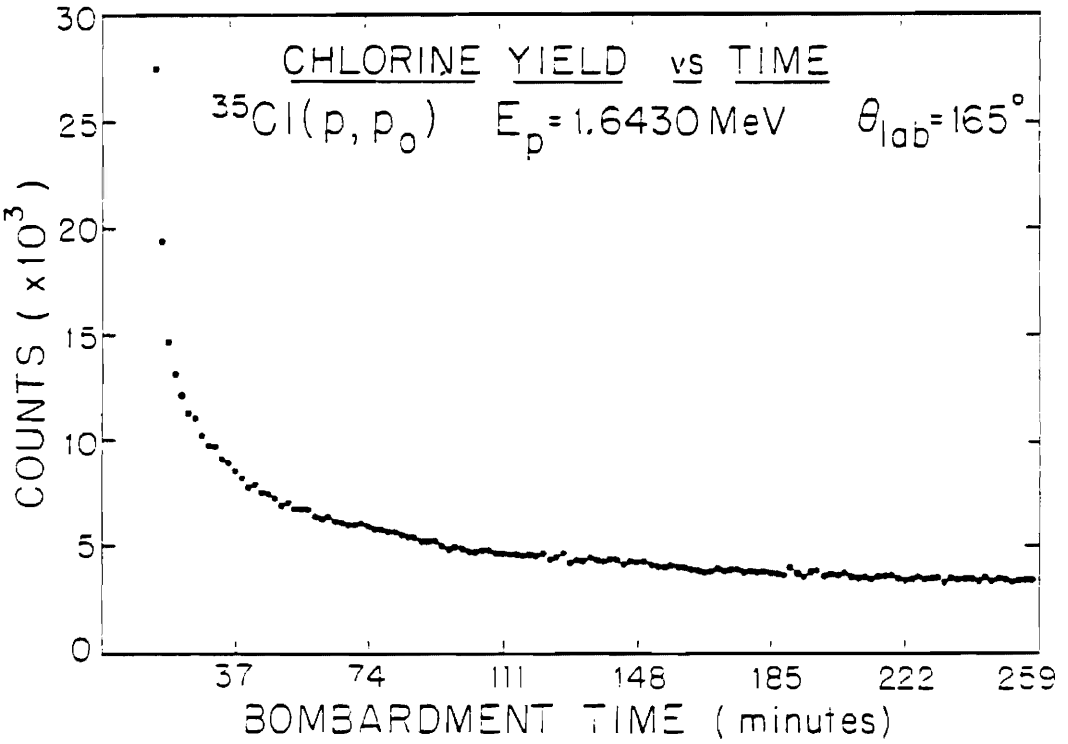
CHLORINE YIELD vs TIME
$^{35}Cl(p,p_0)$ E_p=1.6430MeV θ_{lab}=165°
COUNTS (x10^3)
0
5
10
15
20
25
30
37
74
111
148
185
222
259
BOMBARDMENT TIME (minutes)

decay in the original targets and its prevention in the final targets. However, it is certainly possible to model the processes based on what is already known about thin film behavior. After much consideration such a model has been formulated and is presented here; it must however be considered speculative in its details.

The original targets decayed primarily by a chemical process which liberated chlorine as a gas or other volatile compound. The physical instability caused by this also induced a much smaller fraction of the decay, seen as occasional sudden drops in the chlorine time yield and a slight decrease in the barium time yield.

When nickel is evaporated onto the carbon foil before the layer of barium chloride is deposited, the decay still occurs, but to a somewhat lesser extent, and it eventually stops after much of the chlorine originally present is gone. This is understood to be where the nickel evaporation has produced a spotty layer of nickel with many open holes and an average thickness of 7 - 8 angstroms. This is the expected behavior for metals evaporated onto most substrates in that average thickness. The next evaporation deposited barium chloride both on the nickel spots and carbon holes, probably also in the form of amorphous clumps randomly distributed, or possibly clumps growing on the nickel seed clumps. This phenomenon is known to happen in evaporations of certain metals onto other metals. In the beam the barium chloride which was in contact with the carbon decayed, but that which was only in contact with the nickel did not.

In the "baking" process at elevated temperatures of perhaps 600 - 700^{o}C the nickel clumps spread out to cover the carbon surface, with diffusion of the carbon into the nickel. Such diffusion properties of carbon into metals are well known; in fact the carbon foil was observed to have diffused into the stainless steel target ring when heating the targets under vacuum. It would be a little surprising that the nickel completely covers the surface, since it began initially in the form of clumps. However, from experience if at any time the barium chloride comes into contact with the carbon it will decay in the beam; thus one may consider that to be a measure of the exposed area of carbon. By this measure the surface is completely covered. It is also thoroughly outgassed; however this effect is probably

undone by removing the backings from the vacuum before the final evaporation.

BIBLIOGRAPHY

Amaldi, E., D'Agostino, O., Fermi, E., Pontecorvo, B. Rasette, F. and Segre, E., Proc. Roy. Soc. 149, 522 (1935).

Biedenharn, L.C., Blatt, J.M., and Rose, M.E., Rev. Mod. Phys. 24, 258 (1952).

Bilpuch, E.G., Lane, A.M., Mitchell, G.E., and Moses, J.D., Phys. Reports 28C, 147 (1946).

Bohr, N., Nature (London) 137, 344 (1936).

Bosnjakovic, B., Bouwmeester, J., Van Best, J.A. and Pruys, H.S., Nucl. Phys. A110, 17 (1968).

Boyd, M.A., Gould, C.R., and Roberson, N.R. , XSYS Reference Manual. 4th. ed. Durham, N.C. Triangle Universities Nuclear Laboratory, 1984.

Bull, J.S., Ph. D. dissertation, Duke University, 1988(projected).

Clarke, R.L., Almqvist, E. and Paul, E.B., Nucl. Phys. 14, 472 (1960).

Clayton, D.D., Woosley, S.E., Rev. Mod. Phys. 46, 755 (1974).

Erne, F.C. and Endt, P.M., Nucl. Phys. 71, 593 (1965).

Fang, D. F., "Proton Resonance Spectroscopy in ^{32}S", Ph. D. dissertation, Fudan University(China), 1988.

Gilbert, A. and Cameron, A.G.W., Can. J. Phys. 43, 1446 (1965).

Holzweig, L.G. and Poore, R.V., IEEE Trans. Nucl. Sci. NS-28, 3815 (1981).

Huby, R., Proc. Phys. Soc. A67, 1103 (1954)

Kapur, P.L. and Peierls, R.E., Proc. Roy. Soc. A166, 277 (1938).

Karadzhev, K., V., Man'ko, V.I., Chukreev, F.E., J. Nucl. Phys. (U.S.S.R.)4, 909 (1966).

Kernbach, K.G., Lettere al Nuovo Cimento III, 461 (1970).

Krieger, T.J. and Porter, C.E., J. Math. Phys. 4, 1272 (1963).

Heisenberg, W., Z. Physik 120, 513 and 673 (1943).

Holland, L., Vacuum Deposition of Thin Films (Chapman and Hall Ltd.,1966).

Johnson, P.M., Meyer, M.A., and Reitmann, D., Nuclear Physics A218, 333 (1974).

Lane, A.M. and Thomas, R.G., Rev. Mod. Phys. 30, 257 (1958).

Liou, H.I., Camarda, H.S., Wynchank, S., Slagowitz, M., Hacken, M.,Rahn, F., and Rainwater, J., Phys. Rev.C5, 974 (1972).

Marmier, P. and Sheldon, E., Physics of Nuclei and Particles, Vol. I (Academic Press, New York, 1969)

Marmier, P. and Sheldon, E., Physics of Nuclei and Particles, Vol. II (Academic Press, New York, 1970)

McCarthy, I.E. Introduction to Nuclear Theory (J. Wiley and Sons, New York, 1968).

Moon, P.B. and Tillman, R., Proc. Roy. Soc. 153, 421 (1936).

Nelson, R.O., Bilpuch, E.G., and Mitchell, G.E., Nucl. Instrum. and Methods A236, 128 (1985) .

Porter, C.E. and Thomas, R.G., Phys. Rev. 104, 483 (1956).

Roberson, N.R. and Edwards, S.E., IEEE Trans. Nucl. Sci. NS-28, 3834 (1981).

Schiff, L. I., Quantum Mechanics (McGraw-Hill Book Company, Inc., New York, 1968)

Sellin, D.L., "Excited States in ^{19}F", Ph. D. dissertation, Duke University, 1969.

Szilard, L., Nature, 163, 849 (1935).

Vogt, E., Rev. Mod. Phys. 34, 723 (1962).

Warthen, B.J., "Proton Resonance Spectroscopy in ^{40}Ca", Ph. D. dissertation, Duke University, 1988.

Westerfeldt, C.R., Nelson, R.O., Bilpuch, E.G., and Mitchell, G.E., The TUNL High Resolution Laboratory System and Operating Procedures (TUNL Technical Report, 1986).

Westerfeldt, C.R., Nelson, R.O., Bilpuch, E.G., and Mitchell, G.E., Nucl.

Instrum. and Methods A270, 467 (1988).

Wigner, E.P., Phys. Rev. 70, 15 (1946).

Wigner, E.P., Phys. Rev. 70, 606 (1946).

Wigner, E.P., and Eisenbud, L., Phys. Rev. 72, 29 (1947).

Ziegler, J. F., Handbook of Stopping Cross Sections for Energetic Ions in All Elements, Vol. V (Pergamon Press Inc., 1980).

BIOGRAPHY

William King Brooks Jr.

Personal:	Born March 7, 1959 Savannah, Georgia
Education:	B.S. Physics, University of Florida 1981 B.A. Mathematics, University of Florida 1981 M.A. Physics, Duke University 1984
Positions:	Teaching Assistant, Duke University 1982 – 1983 Research Assistant, Duke University 1983 – 1988
Abstracts:	"A High Resolution Proton Study of ^{36}Ar," W. K. Brooks, C. R. Westerfeldt, E. G. Bilpuch, and G. E. Mitchell, Bull. Am. Phys. Soc. 32, 2145(1987) "Levels of ^{36}Ar from High Resolution Proton Scattering," W. K. Brooks, C. R. Westerfeldt, E. G. Bilpuch, and G. E. Mitchell, Bull. Am. Phys. Soc. 30, 1769 (1986).
Publications:	"Preparation of Thin-Film Targets of Chlorine," William K. Brooks, Nucl. Instr. and Methods A257(1987)4-6 "Status Report on Metal-Coated Carbon Backings," William K. Brooks, Newsletter of the International Nuclear Target Development Society, December 1987, p. 9
Memberships:	American Physical Society